Development of Peptide Inhibitors of Cancer Cell Signaling Targets, STAT3 and LC3B

A thesis submitted by

Robert A. Cerulli

in partial fulfillment of the requirements for the degree of

PhD

in

Cell, Molecular, and Developmental Biology

Tufts University

Graduate School of Biomedical Sciences

May 2020

Adviser: Joshua Kritzer, PhD

Abstract

Despite decades of research and considerable advancements in the field of novel cancer therapeutics, there remains a high demand for new strategies and new molecules to combat aggressive, chemoresistant malignancies. Two cell signaling pathways that have been studied for several decades and have been the subject of inhibitor development, are STAT3 signaling and the autophagy pathway. There is considerable evidence to suggest that both pathways contribute to cancer progression and chemoresistance, yet to date, neither pathway has been granted an FDA-approved inhibitor for use in the treatment of cancer. As such, the manuscripts of this work describe our efforts to develop peptide-based inhibitors of these pathways.

For STAT3, these efforts consist of peptides targeting the Src Homology 2 (SH2) domain, conjugated to highly cytosolically efficient cell-penetrating peptides (CPPs). We studied the binding affinity of STAT3-targeted peptides incorporating hydrolytically stable phosphotyrosine (pTyr) analogs. Further, we studied the cell penetration of these CPP-conjugated peptides, observing impressive cell penetration for CPP-conjugated anionic peptides. We also studied serum and lysate stability of CPP-conjugated peptides, noting not only resistance to dephosphorylation but additional resistance to proteolytic degradation with use of pTyr isosteres. This work provides several insights into the balance of affinity, stability, and cell penetration of SH2-targeted inhibitor development.

The autophagy-aimed efforts of this work focused on peptide inhibitors of the central autophagy protein, LC3B. In this work, we focused largely on structure-activity relationship efforts, studying the binding of the LC3-Interacting Region (LIR) motif of the adapter protein FYCO1. We studied the FYCO1 LIR motif binding to LC3B, determining the contributions to affinity of residues in the N- and C-termini, as well as the seven negatively charged residues, and the hydrophobic pocket-targeted residues. Further we

incorporated numerous artificial amino acids and ultimately perform diversity-oriented peptide stapling to generate optimized LC3B inhibitors with up to 2.4-fold improvement in binding affinity while maintaining LC3B paralog selectivity and improving lysate stability by about 2-fold. Both our STAT3- and LC3B-aimed efforts provide useful insights into the development of selective inhibitors of these cancer-relevant protein targets.

Dedication

This work is dedicated to the mentors who have invested their time and effort in my training and who have truly helped shape my career path. In particular, I'd like to thank those whose guidance has instilled in me a passion for medicine and science and a genuine longing to combine the two to make a difference in the lives of others; thank you David, Andy, Carol, and Joshua.

Further, this work is dedicated to my family, especially my parents, Bob and Annette, who worked tirelessly to provide me with the opportunities that have led me to this degree program and career path. You've made your dream the ability for me to follow my heart and I will never take that for granted. These accomplishments are in no small part a result of what you have worked for. This is also dedicated to my sister and oldest friend in the world, Michelle, and her husband and my brother-in-law, Matt. I am so grateful for the love and support you two bring to my life and can't wait for the chapters ahead for our family.

Lastly, this work is dedicated to my wife and best friend, Shaylagh. This degree is as much yours as it is mine. I could not have gotten through this PhD training without you. For the last five years, you have been my rock. You have lifted me up when times were difficult and reeled me in whenever I would get too far ahead of myself. You have always had confidence in me, even when I wasn't so sure. Thank you for making this whole thing possible, and even more so for the joy you bring my life every single day. I can't wait to see what adventures are in store for you, me, and our new little one.

Acknowledgements

I'd like to acknowledge my thesis committee, including my PI and thesis advisor, for all of their advice and support throughout this PhD training and for constantly pushing me to a deeper level of understanding and questioning. Thank you Joshua, Phil, Jim, and Rebecca. I would also like to acknowledge and thank my external committee member, Dr. Loren Walensky.

I would also like to acknowledge the additional mentorship and collaborations with Dr. David Frank and his lab at the Dana Farber Cancer Institute. Thank you for your mentorship and all of the help from Isidora, Kevin, and others on our shared work. Thank you even more so for your continued support on my career path over these past ten years.

I'd like to acknowledge all of the help from my labmates (and honorary labmates) past and present. Whether troubleshooting experiments, fixing instruments, or talking through the daily challenges of PhD training, thank you for helping me on this journey. I'm glad to have gone through it with all of you and hope I've helped your journey as well.

I would also like to acknowledge the support from the Tufts Graduate School of Biomedical Sciences, the Medical Scientist Training Program, and the Tufts University Chemistry Department. Thank you to the professors, directors, deans, and administrators who keep these programs running and these buildings standing.

Lastly, I would like to acknowledge the funding sources of my PhD training, in particular the NIH Ruth L. Kirschstein Individual Predoctoral Fellowship Training Grant F30CA220678 (NIH, NCI). Thank you for supporting this work and even more so for believing in and supporting my training as a physician scientist.

Table of Contents

List of Tables

List of Figures

List of Copyrighted Materials

Cerulli, R.A.; Kritzer, J.A. Phosphotyrosine Isosteres: Past Present and Future. *Org. Biomol. Chem.;* 18(4): 583-605. **2019**.

List of Abbreviations

ALS – Amyotrophic lateral sclerosis
BCA – bicinchoninic acid (assay)
Bcl-2 – B-cell lymphoma 2 protein
Bcl-xL – B-cell lymphoma-extra large protein
BLI – biolayer interferometry
B-Raf – B-Raf proto-oncogene, serine/threonine kinase
CAPA – chloroalkane penetration assay
cF – carboxy phenylalanine
CPP – cell-penetrating peptide
ct – chloroalkane tag
DCM – dichloromethane
DIPEA – diisopropylethylamaine
DMEM – Dulbecco's modified eagle medium
DMF – dimethylformamide
DMSO – dimethyl sulfoxide
DTT – dithiothreitol
EDT – ethanedithiol
EDTA – ethylenediaminetetraacetic acid
F_2Pmp – difluorophosphonomethyl phenylalanine
FAK – focal adhesion kinase
FBS – fetal bovine serum
FLT3 – Fms-like tyrosine kinase 3 protein
FMOC – fluorenylmethyloxycarbonyl (protecting group)
FP – fluorescence polarization
FPLC – fast protein liquid chromatography
FRET – Förster resonance energy transfer
FYCO1 – FYVE and coiled coil domain-containing protein 1
GABARAP(L1/L2) – gamma-aminobutyric acid receptor-associated protein(-like 1/2)
gp130 – glycoprotein 130
Grb2 – growth factor receptor-bound protein 2
Grb7 – growth factor receptor-bound protein 7
GST – glutathione S-transferase
HATU – hexafluorophosphate azabenzotriazole tetramethyl uronium
HBTU – hexafluorophosphate benzotriazole tetramethyl uronium
HER2 – human epidermal growth factor receptor 2
HOBt – hydroxybenzotriazole
HP1/2 – hydrophobic pocket 1/2
HPLC – high performance liquid chromatography
IL-6 – interleukin 6
IPTG – Isopropyl β-D-1 thiogalactopyranoside
JAK – Janus kinase
LC3A/B/C – microtubule-associated protein 1A/1B light chain 3A/B/C
LIR – LC3-interacting region
MALDI-TOF – matrix-assisted laser desorption/ionization – time of flight mass spec
MMPs – matrix metalloproteases
mTOR – mammalian target of rapamycin
OSM – oncostatin-M
p62 – sequestrome 1 protein
PD-1 – programmed cell death protein 1

PD-L1 – programmed death-ligand 1
PE – phosphatidylethanolamine
PI-3K – phosphoinositol-3 kinase
Pmp – phosphonomethyl phenylalanine
PROTAC – proteolysis targeting chimera
Pten – phosphatidylinositol 3,4,5-triphosphate 3-phosphatase and dual-specificity protein phosphatase
PTP1B – protein tyrosine phosphatase 1B
Ptps – protein tyrosine phosphatases
pTyr – phosphotyrosine
Pybop – benzotriazol-1-yl-oxytripyrrolidinophosphonium hexafluorophosphate
RAC1 – Ras-related C3 botulinim toxin substrate 1
SH2 – Src homology 2
SHC – Src homology 2 domain-containing protein
STAT1 – signal transducer and activator of transcription 1
STAT3 – signal transducer and activator of transcription 3
Tat – trans-activator of transcription protein
TFA – trifluoroacetic acid
TIAM1 – T-lymphoma invasion and metastasis-inducing protein 1
TIPS – triisopropylsilane
ULK1 – Unc-51 like autophagy activating kinase
VEGF – vascular endothelial growth factor
VHL – Von Hippel-Lindau
VPS34 – vacuolar protein sorting 34

Chapter 1: Introduction to STAT3 and Autophagy Signaling Pathways in Cancer

1.1. Targeting the STAT3 SH2 Domain for Novel Anticancer Therapeutics

1.1.1. STAT3 Signaling and Cancer

The Signal Transducer and Activator of Transcription 3 (STAT3) has long been a desirable target for drug discovery efforts due to its pro-tumorigenic transcriptional activity. STAT3 is a transcription factor in the JAK/STAT cytokine signaling pathway. When extracellular cytokines such as IL-6 or Oncostatin-M bind their corresponding receptors, the receptors activate JAK family kinases.[1,2] STAT3 monomers are then localized to the cell membrane and are subsequently phosphorylated by JAK kinases. Following phosphorylation, STAT3 monomers undergo dimerization, becoming transcriptionally active. The STAT3 homodimer then translocates to the nucleus, where it can upregulate numerous STAT3 target genes, many of which are central to the hallmarks of cancer.[1,2] STAT3 has been shown to induce angiogenesis through expression of proteins such as vascular endothelial growth factor (VEGF), enhance cancer cell motility through expression of matrix metalloproteinase-2, and to escape cell death through upregulation of antiapoptotic proteins including survivin, Bcl-2, and Bcl-xL.[3–6] It was shown by Schlessinger and Levy that STAT3 was required for the malignant transformation of mouse fibroblasts, but, importantly, that normal fibroblast growth did not depend on this activity.[7] This suggests that there exists a reasonable therapeutic window for STAT3 inhibition in some cancers. Additionally, STAT3 has been shown to enhance the expression of the checkpoint inhibitors PD-1 and PD-L1.[8] It is possible that these largely efficacious checkpoint inhibitors could be further assisted through the addition of a targeted STAT3 inhibitor.[9] For decades, STAT3 has been the focus of drug development efforts because of the tremendous body of research highlighting its central role in cancer cell signaling.[1,2,10]

1.1.2. SH2 Domains: Structure and Function

STAT3's Src Homology 2 (SH2) domain is critical for its function. SH2 domains were first described by Pawson and colleagues in 1986, and soon after it was shown that SH2 domains recognize phosphorylated tyrosine residues (pTyr) and mediate pTyr signaling across diverse cell signaling networks.[11,12] There are over 110 human proteins with SH2 domains, all with very different purposes and functions in the cell, from adapters and scaffolding proteins to transcription factors.[13,14] The activity or expression of SH2 domain-containing proteins are dysregulated in countless human diseases, including many cancers.[13,14] As such, considerable work has been done over the past several decades to better understand the structure and function of SH2 domains, in the pursuit of developing selective SH2 inhibitors.

In 1992, the first crystal structure of an SH2 domain binding its respective phosphopeptide ligand revealed that the domain is comprised of a central, multi-stranded β-sheet connected by several loop regions and flanked by two α-helices.[15,16] This tertiary structure forms two separate binding pockets: one that recognizes pTyr and a secondary pocket that recognizes amino acids in close proximity to the pTyr residue (typically, C-terminal to the pTyr). Work in 1990 by Cantley and colleagues used a phosphopeptide library to characterize the selectivity motifs of over a dozen SH2 domains.[17] This work introduced the concept, which was later verified through more comprehensive binding studies and structural characterization, that SH2 ligand specificity is most commonly dictated by the residues immediately C-terminal to the phosphotyrosine. Further, SH2 domains could be classified based on binding preferences, as there was considerable overlap in consensus sequences for different groups of SH2 domains. Armed with this improved understanding of how to selectively target subsets of SH2 domains, or even individual SH2 domains, researchers began

drug discovery efforts that would collectively span several decades. These efforts focused on developing selective inhibitors of SH2 domains implicated in cancers and other diseases, including STAT3.

STAT3's SH2 domain is indispensable for its activity. The SH2 domain is required for initial docking at the membrane to the IL-6 signaling chain, gp130. Upon extracellular cytokine stimulation and subsequent gp130 phosphorylation, the STAT3 SH2 domain recognizes and docks to phospho-gp130 so that STAT3 can subsequently be phosphorylated on its own tyrosine (Y708).[10] This phosphorylation allows the pTyr of one STAT3 monomer to be recognized by an additional monomer's SH2 domain, and vice versa, producing a STAT3 homodimer. It is this dimer that is capable of nuclear translocation and transcriptional activity. Therefore, the SH2 domain is critical for the pro-tumorigenic transcriptional activity of STAT3, and thus represents an enticing target for inhibitor development.

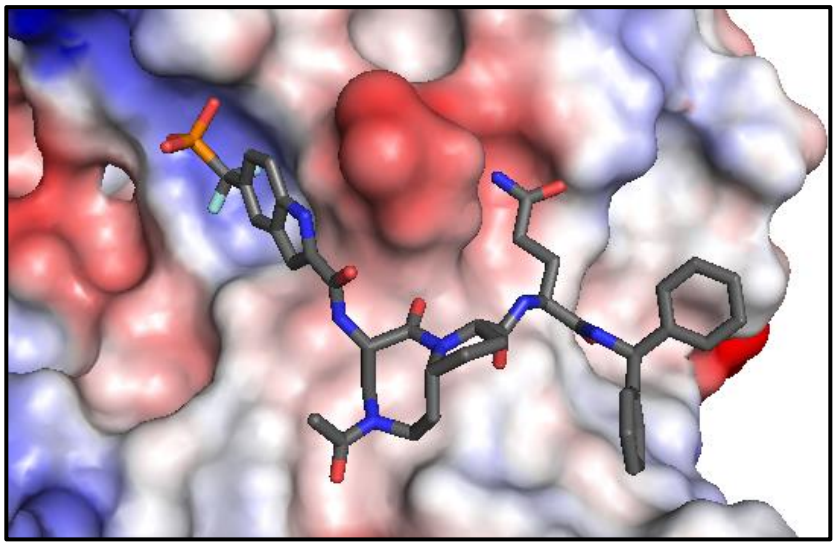

Figure 1.1. STAT3 SH2 domain structure. Here binding difluorophosphonate-containing peptidomimetic (discussed below). The negatively charged pTyr mimic binds the positively charged pTyr binding pocket (blue), and the glutamine side chain (+3 position) engages the specificity pocket (red). (PDB: 6NJS)[18]

1.1.3. pTyr and pTyr Isosteres to Inhibit SH2 Domains

It became clear very early on that inhibiting SH2 domains with pTyr would be challenging. While pTyr-containing peptides could achieve high affinity to SH2 domains *in vitro*, pTyr itself exhibited poor pharmacological properties.[19] It is extremely unstable in the intracellular environment due to intracellular phosphatases, and additionally with two negative charges is poorly cell penetrant. As such, successful SH2 domain inhibitors would need to incorporate pTyr mimics, or isosteres, that could combat these barriers. The simplest class of pTyr isosteres, benzyl phosphonates, replaced the phosphate bridging oxygen with a methylene unit, ensuring stability to hydrolysis. Shoelson, Burke and co-workers reported the first peptide inhibitor containing a phosphonomethyl phenylalanine (Pmp) residue.[20] Their phosphonopeptide targeting the N-terminal SH2 domain of phosphatidyl inositol-3 kinase (PI-3K) bound with a K_d of 20 nM, which represented excellent affinity since the native phosphopeptide bound with a K_d of 10 nM. In mouse 3T3 fibroblast cell lysates in the presence of vanadate, a potent phosphatase inhibitor, both peptides outcompeted PI-3K interaction with its binding partner, middle T-antigen (100 nM and 800 nM for the phospho and phosphono-peptide respectively). But in the absence of vanadate, only the phosphonopeptide maintained inhibition. This early work demonstrated that pTyr isosteres would need to be phosphatase-stable to achieve sufficient intracellular efficacy.

While the Pmp residue demonstrated considerable stability, there was still an apparent loss in peptide affinity compared to the native pTyr. To improve upon this, Burke and colleagues made more sophisticated isosteres, including fluoro-, difluoro-, and hydroxy-Pmp.[21,22] The difluorophosphonomethyl phenylalanine (F_2Pmp) was incorporated into a hexapeptide substrate of the phosphatase PTP1B, and demonstrated a 1000-fold greater inhibitory potency than the Pmp peptide (IC_{50} values of 100 nM and

approximately 100 μM, respectively).[21] This difference made apparent the importance of not only stability, but of H-bonding interactions of the phosphate's bridging oxygen, as well as the importance of fluorine atoms as electron-withdrawing groups to mimic pTyr.[22] However in subsequent work, it was demonstrated that not all SH2 domains tolerate F_2Pmp substitution well. F_2Pmp was incorporated into peptides targeting the C-terminal SH2 domain of PI-3K, Src, and Grb2, but these peptides differed in their relative binding affinities.[23] The PI-3K F_2Pmp peptide displayed similar binding affinity as the native pTyr (170 nM vs. 150 nM). The Grb2 peptide, however, lost 5-fold affinity compared to pTyr, and the Src peptide gained 5.7-fold affinity compared to pTyr. Since those early works, the F_2Pmp isostere has been incorporated into many peptide and small molecule inhibitors.[24–27] Later results continued to show that different SH2 domains and PTPs have very different responses to substitution of these and other pTyr isosteres.

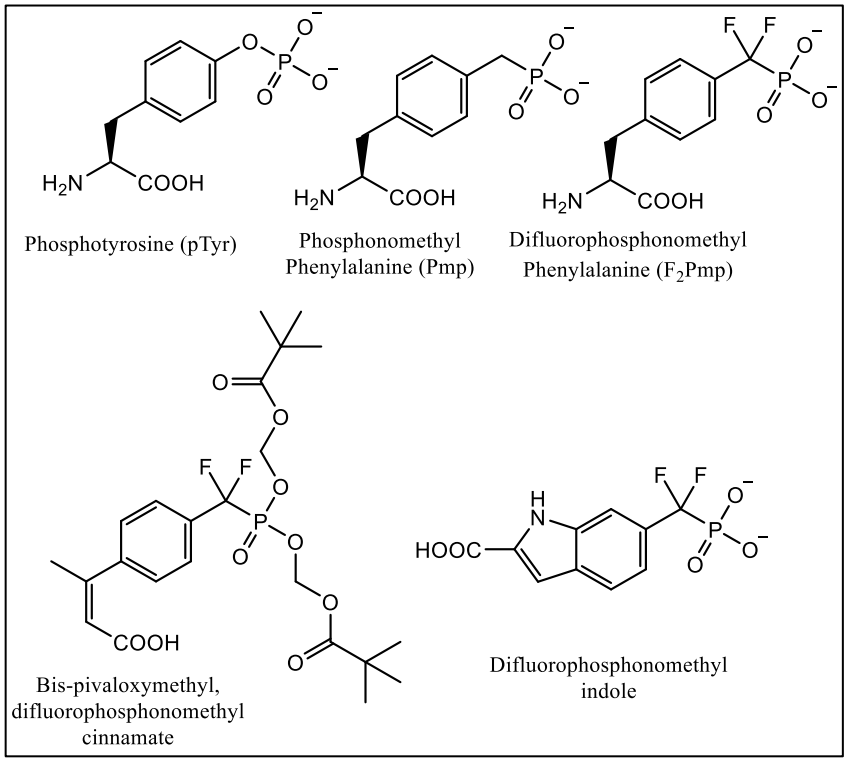

Figure 1.2. Phosphonates and STAT3-targeted phosphonate derivatives. (Adapted from [Cerulli, R.A.; Kritzer, J.A. Phosphotyrosine Isosteres: Past Present and Future. *Org. Biomol. Chem;* 18(4): 583-605. **2019**.] with permission from the Royal Society of Chemistry. Alterations include the removal of several non-phosphonate structures and the addition of the difluorophosphonomethyl indole structure.)

Though initial phosphonate inhibitors were developed several decades ago, phosphonate-derivatives continue to be incorporated into SH2-targeted inhibitors, including against STAT3. For example, recently McMurray and colleagues developed peptidomimetics containing a 4-phosphonodifluoromethylcinnamate. Using reversible pivaloyloxymethyl protecting groups, they were able to mask the phosphonate negative charges to improve upon cell penetration.[28–32] Their most potent molecule inhibited intracellular STAT3 phosphorylation at 100 nM in MDA-MB-468 cells and displayed impressive STAT3 selectivity compared to STAT5 and the highly homologous STAT1.[29]

Even more recently, Bai and colleagues generated a difluorophosphonomethyl indole, which they incorporated into small peptidomimetic STAT3 SH2 domain inhibitors.[18] Their inhibitors bound with impressive affinity (K_i 10 nM by competition FP assay), and potently inhibited STAT3 transcriptional activity in cells with an IC_{50} of 3 μM. Uniquely, Bai and colleagues used this ligand to design a proteolysis targeting chimera (PROTAC)[33] capable of efficiently degrading STAT3 protein. The STAT3 PROTAC molecule potently suppressed xenograft tumor growth in mice of multiple hematological malignancies. So, not only are pTyr isosteres very much still being evaluated in SH2 domain inhibitors today, but new uses for them continue to be discovered.

1.1.4. Small Molecule pTyr Isosteres Targeting STAT3

While peptide and peptidomimetic approaches generated potent binders in biochemical assays, many of these inhibitors failed to demonstrate sufficient activity in cell culture. The most common explanation for this discrepancy was that the negative charges of pTyr isosteres fostered poor cell permeability. This led to increasing efforts focused on small molecule inhibitors, as this would provide more cell-penetrant starting points. Unfortunately, while small molecules generally had improved cell penetration, they were often less selective among related SH2 domains and PTPs. Thus, testing selectivity

along with affinity and cell-based activity became a necessary balancing act for developing these small molecule inhibitors.

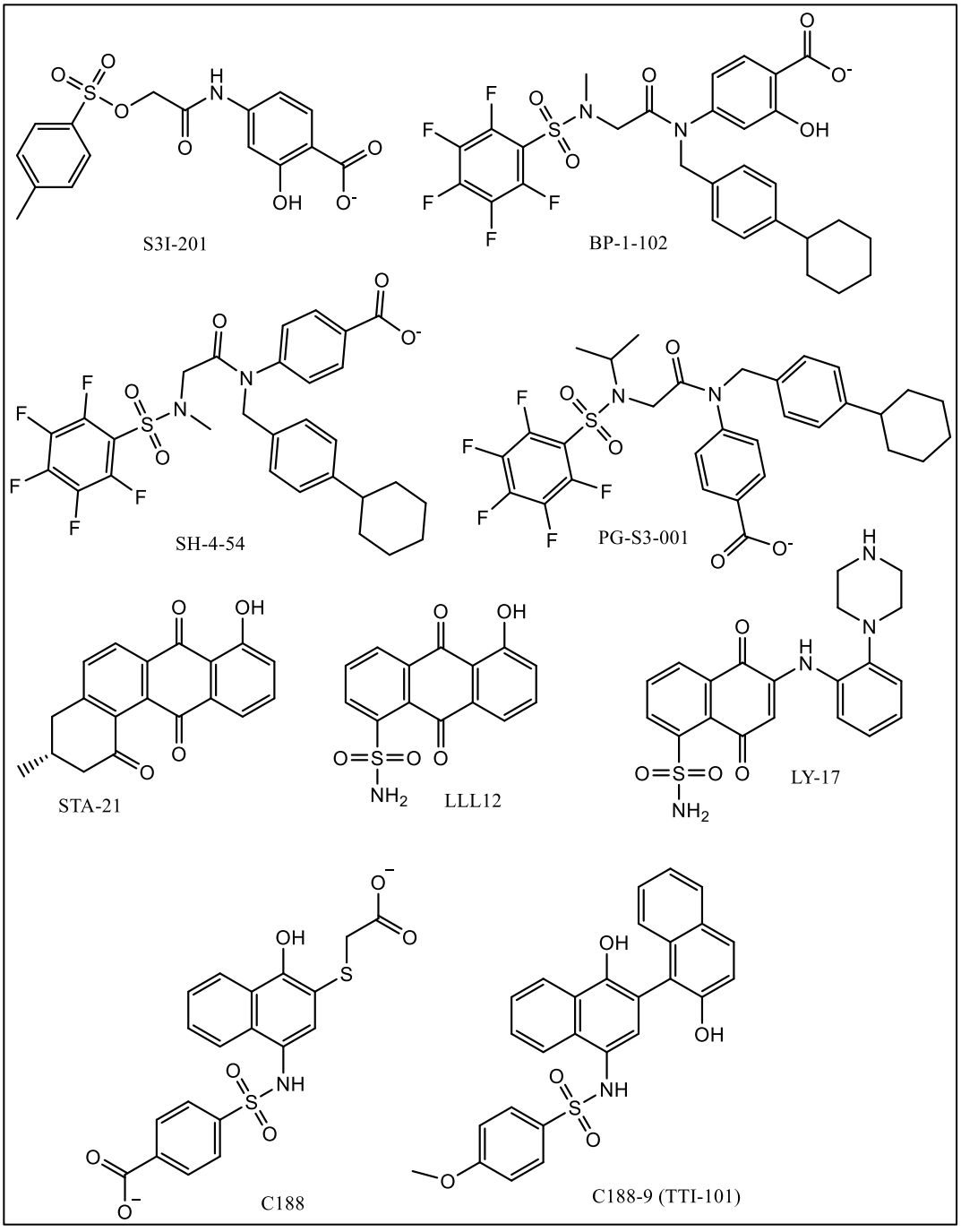

Fig 1.3. Structures of select STAT3-targeted pTyr isostere-containing small molecules. (Adapted from [Cerulli, R.A.; Kritzer, J.A. Phosphotyrosine Isosteres: Past Present and Future. *Org. Biomol. Chem.;* 18(4): 583-605. **2019**.] with permission from the Royal Society of Chemistry. Alterations include the removal of several non-STAT3 targeted small molecule structures.)

In 2007, Turkson and colleagues reported one of the earliest small molecule inhibitors of the STAT3 SH2. S3I-201 was identified from a virtual screen, and contained a salicylate as a pTyr isostere.[34] Though this molecule displayed poor *in vitro* inhibition, S3I-201 inhibited MDA-MB-231 human breast tumor growth in a xenograft model when delivered intravenously. Working with Gunning and colleagues, multiple improved derivatives were generated both by rational and computer-aided design.[35–39] Their most optimized analog, BP-1-102 had a K_d of 504 nM, and an IC_{50} of 4.1 μM for outcompeting a STAT3-phosphopeptide interaction. Impressively, it displayed 7-fold selectivity for STAT3 over STAT1 and STAT5 and inhibited tumor growth in mouse xenograft models of human breast and non-small cell lung cancers.[37] Gunning and colleagues would go on to generate several other derivatives (SH-4-45 and PG-S3-001). With the removal of the salicylate hydroxyl group, they produced benzoates with improved affinities, displaying efficacy in models of glioblastoma multiforme and pancreatic adenocarcinoma.[38,39] These works demonstrated that salicylates and benzoates can be effective pTyr mimics for STAT3-targeted inhibitors.

In a separate series of papers targeting STAT3-SH2, a virtual screen of a 429,000-member small molecule library identified the STAT3 inhibitor STA-21.[40] Lin and colleagues showed that STA-21 blocked STAT3 homodimerization at 20 μM in MDA-MB-435 breast cancer cells and induced apoptosis in several STAT3-dependent breast cancer cell lines, as well as in rhabdomyosarcoma and bladder cancer cell lines.[41,42] A significantly more potent derivative, LLL12, used an uncharged sulfonamide as its pTyr isostere.[43] LLL12 displayed IC_{50} values between 0.16 to 3 μM when tested in multiple pancreatic cancer, breast cancer, and glioblastoma cell lines. *In vitro* and *in vivo* work in STAT3-dependent hepatocellular carcinoma, medulloblastoma, pancreatic cancer, and

multiple myeloma demonstrated further compound efficacy.[44–47] Using a fragment-based approach, Kong and colleagues identified LY-17, a sulfonamide quite similar to LLL12.[48] LY-17 potently inhibited STAT3 phosphorylation in MDA-MB-231 breast cancer cells at 5 μM. Further, it demonstrated a significant reduction in tumor growth in a xenograft breast cancer model with oral delivery.

Another prominent sulfonamide, one currently in clinical trials, was discovered by Tweardy and colleagues via a 920,000-member virtual library screen.[49] The most potent hit from this screen was compound C188, however this molecule also exhibited toxicity in non-STAT3-dependent cell lines.[50] Additional computational screening improved C188, producing C188-9 with an impressive K_d of 4.7 nM for STAT3.[51] C188-9 lacked both carboxylates of C188. C188-9 inhibited STAT3 phosphorylation in cells and, importantly, displayed no effect on healthy bone marrow colony formation, suggesting an improved toxicity profile compared to its predecessor. In mouse models with UM-SCC-17B head and neck squamous cell carcinoma, C1889 significantly reduced tumor size when delivered at 100 mg/kg daily. Tvardi Therapeutics was founded in 2017 to move C188-9, now named TTI-101, into clinical trials.

1.1.5. Clinical Trials of STAT3 Inhibitors

Very few inhibitors of SH2 domains have entered clinical trials, and as of yet none have been granted FDA approval. Among SH2 domain inhibitors, only a select few compounds that target the STAT3 SH2 domain have been tested clinically. The sulfonamide TTI-101, developed by Tvardi Therapeutics, is currently in phase I trials for patients with advanced solid tumors (NCT03195699). The STAT3 inhibitor STA-21 was tested in a phase I/II trial as a topical therapy for psoriasis, improving skin lesions for six of the eight patients tested.[52] However, since this trial concluded in 2010, STA-21 has not been advanced to further clinical testing. Several small molecule STAT3 SH2

inhibitors developed by Otsuka Pharmaceuticals were also tested clinically. OPB-51602 and OPB-31121 were both tested in a variety of phase I and II clinical trials for patients with solid tumors and hematological malignancies. However, neither molecule progressed to phase III trials due to dose-limiting toxicities including lactic acidosis and peripheral neuropathies.[53–57] OPB-111077 is another STAT3 SH2 inhibitor by Otsuka, and OPB-111077 currently remains in clinical trials. In initial phase I testing, this drug was well-tolerated in patients with hepatocellular carcinoma and advanced solid tumors.[58,59] OPB-111077 is currently in phase I trials as a single agent and in combination with bendamustine and rituximab.

Beyond direct SH2 domain inhibition, other approaches for inhibiting STAT3 activity have been tested clinically.[60–63] AstraZeneca's AZD9150 is an antisense oligonucleotide therapy targeting STAT3. Several phase I and I/b trials in patients with treatment-refractory lymphomas and lung cancer demonstrated good overall tolerability and even initial signs of efficacy.[62,63] Multiple phase I/II and phase II trials are currently recruiting patients with triple negative breast cancer, non-small cell lung cancer, and several other advanced cancers.

Pyrimethamine, an FDA-approved anti-malarial, has also been shown to modulate STAT3 activity through an unknown, likely indirect, mechanism.[64] It is currently in phase I clinical trials for patients with myelodysplastic syndromes and chronic lymphocytic leukemia (NCT03057990, NCT01066663).

Additionally, modulating tyrosine kinase activity upstream of STAT3, including various JAK inhibitors, is another proven strategy to treat advanced cancers. Multiple clinical trials have been conducted with several JAK inhibitors for patients with numerous solid and hematological malignancies.[1,65] Currently ruxolitinib (Jakafi) and fedratinib (Inrebic) are the only two JAK inhibitors approved for use in cancers. Ruxolitinib is a JAK1/2

inhibitor approved for patients with myelofibrosis and polycythemia vera[1], and fedratinib is a JAK2-selective/FLT3 receptor tyrosine kinase dual inhibitor recently approved in myelofibrosis patients.[65]

1.1.6. Cell Penetrating Peptide-Conjugated Inhibitors of SH2 Domains and PTPs

The development of STAT3 inhibitors illustrates the challenge of balancing affinity, selectivity, and cell penetration. Perhaps one of the small handful of STAT3 inhibitors that have advanced to clinical trials will achieve this balance and be the first FDA-approved STAT3 inhibitor. However, until this goal is realized, new strategies to inhibit STAT3 activity are still highly sought after.

While some of the previously discussed pTyr isosteres, such as F_2Pmp, have demonstrated affinity for some SH2 domains that is equal to or better than pTyr itself, their multiple negative charges exhibit poorer cell penetration. This has been and continues to be a major barrier for their use in more selective peptide SH2 domain inhibitors. One possible approach for overcoming this barrier is to combine pTyr isosteres with cell-penetrating peptides (CPPs) to promote improved cytosolic delivery.

For several decades, cell-penetrating peptides have been used to promote cellular uptake of otherwise impermeable biomolecules.[66–68] These sequences commonly have many cationic residues or have an alternating pattern of cationic and hydrophobic residues.[66] There are several reports of CPPs, including Tat, polyarginine, and penetratin, being used to deliver phosphopeptide inhibitors of SH2 domains.[69–71] However, given the lack of intracellular stability of phosphopeptides, the more successful efforts using CPPs have incorporated pTyr isosteres.[72,73] Watson and colleagues developed a bicyclic peptide inhibitor of the Grb7 SH2 domain (K_d of 130 nM) incorporating a carboxyphenylalanine residue as a pTyr isostere, and conjugated it to penetratin for improved cell penetration. This peptide inhibited Grb7 binding to FAK,

HER2, and SHC in SKBR3 breast cancer cells.[72] Additionally, Lian and colleagues incorporated F_2Pmp into a bicyclic peptide targeting the phosphatase PTP1B (K_i of 37 nM), in which one macrocycle incorporated the PTP1B binding motif and the other incorporated a cyclic CPP, cyclo(FφR$_4$) where φ is 2-naphthylalanine. This peptide produced a two-fold increase in insulin receptor phosphorylation in HepG2 liver cells when applied at 200 nM.[73] These studies demonstrated that one can develop potent and cell-penetrant inhibitors of SH2 domains and protein tyrosine phosphatases by combining non-hydrolyzable pTyr isosteres, macrocyclization, and CPPs.

In recent years, considerable research efforts have gone into generating CPPs with improved uptake and endosomal escape efficiency. These newer CPPs represent new opportunities to combat the challenge of cell penetration for pTyr-isostere-containing peptides.[74–76] For example, an improved version of cyclo(FφR$_4$), CPP12, was demonstrated by Qian and colleagues to improve cytosolic delivery efficiency by 6-fold compared to cyclo(FφR$_4$), and 30 to 60-fold compared to polyarginine and Tat, respectively.[74]

Chapter 2 consists of a manuscript in which we generate peptides combining the cytosolically efficient CPP12 with pTyr isosteres such as Pmp and F_2Pmp to generate more cell-penetrant inhibitors of the STAT3 SH2 domain. In this work, we studied these CPP12-conjugated peptides for their ability to bind STAT3 and inhibit STAT3 transcriptional activity. Despite STAT3 binding *in vitro*, we observed no cell-based phenotypes with our initial CPP12-conjugates, prompting a more in-depth analysis of the cell penetration and stability of our pTyr isostere-containing peptides.

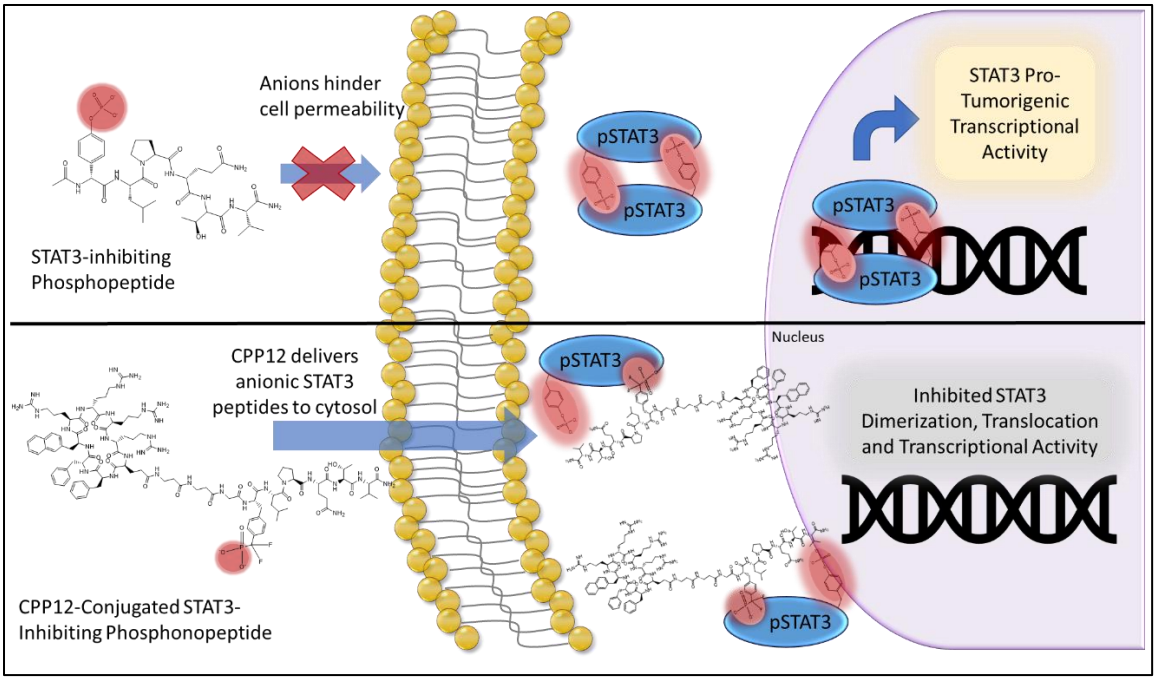

Fig 1.4. Hypothesis of our CPP12-gp130 conjugate peptide work. By conjugating CPP12 to STAT3-targeted peptides containing Pmp or F_2Pmp, we can generate more cell-penetrant, hydrolytically stable STAT3 SH2 domain inhibitors.

1.2 Targeting the Autophagy Pathway for Novel Anticancer Therapeutics

1.2.1. Autophagy and its Involvement in Disease

Autophagy is a conserved eukaryotic by which cells respond to stress and starvation via recycling organelles, proteins, and other cargo. Autophagy underlies multiple diseases, including neurodegenerative disorders, lysosomal storage diseases, and cancers.[77–79] Once the process is initiated, either through starvation or cellular stresses including oxidative stress or infection, an initiation complex consisting of ULK1, FIP200, ATG13, and ATG101 forms. This process is under constant regulation, most prominently by the mammalian target of rapamycin (mTOR) kinase, a potent inhibitor of autophagy. However, under nutrient-depleted conditions, the ULK1 complex is formed and it phosphorylates a class III PI3K, VPS34. VPS34 then forms a second protein complex that is scaffolded by the protein Beclin-1. This complex is responsible for nucleation of

the initial phagophore, a double membrane which elongates and closes to mature into the autophagosome. Simultaneously, the microtubule-associated protein 1A/1B light chain 3 (LC3) protein is conjugated with phosphatidylethanolamine by core autophagy proteins including ATG4B and ATG7. This converts LC3-I to LC3-II for incorporation into the developing autophagosome membrane. Once the autophagosome has matured, it and its contents are transported to the lysosome, followed by autophagosome-lysosome fusion and degradation.[77–80] Autophagy allows cells to survive harsh environmental stresses, and to defend against disease pathogenesis. Deletion of core autophagy proteins in cells has been linked to neurodegenerative disease and cardiac cell dysfunction.[77–79,81] For example, mutations in the autophagy gene ATG16L1, and corresponding lower ATG16L1 protein levels, is a major risk factor for Crohn's Disease.[82] Meanwhile, mutations in ATG16L2 are associated with systemic lupus erythematosus.[83] Loss-of-function mutations in the ATG5 gene can result in ataxia, systemic sclerosis, and also lupus.[84] Beyond the core machinery of autophagy, many upstream regulators also result in the pathogenesis of many diseases, including lysosomal storage diseases, cardiomyopathies, and protein misfolding diseases such as Parkinson's, ALS and Huntington's.[78] While direct connections can often be made between impaired autophagy and many of these diseases, research into the relationship between autophagy and cancer paints a more complicated picture.

1.2.2. Autophagy and Cancer Cell Signaling

The relationship between autophagy and cancer is complex. There is considerable evidence to suggest autophagy is protective against tumorigenesis.[81,85,86] For example, Qu and colleagues demonstrated that mice heterozygous for Beclin1 disruption developed lung and liver tumors as well as mammary hyperplasia.[86] Fernandez and colleagues demonstrated that autophagy induction in mice through the homozygous

Beclin1 F121A knock-in, inhibiting the interaction of Beclin1 with a negative regulator, Bcl-2, not only results in significantly longer lifespan, but also in markedly lower levels of spontaneous tumorigenesis compared to wildtype littermates.[85] Further, enhanced autophagy *in vivo*, either by these knock-ins or using a Tat-Beclin1 autophagy-inducing peptide, prevented HER2-mediated breast cancer tumorigenesis as shown by Vega-Rubin-de-Celis and colleagues.[5] Additionally in this work, authors looked at patient data to demonstrate an inverse correlation between Beclin1 mRNA and HER2+ breast cancer incidence. Taken together, this evidence would suggest that autophagy is protective against the development of breast cancer.

This resiliency conferred to cells through autophagy induction, however, can also be beneficial to cancer cells, providing a means of resistance for advanced cancers to chemotherapies and targeted treatments. For example, Guo and colleagues observed that homozygous ATG7 deletion reduces tumor burden in K-Ras driven non small-cell lung cancer.[87] Xie and colleagues used ATG7-deficient mice to demonstrate markedly reduced proliferation of a $Braf^{V600E}$ pten-null melanoma xenograft model, conferring significant improvement in survival.[88] Santanam and colleagues also demonstrated that ATG7-null pten-null prostate carcinoma in mice exhibited delayed tumor progression compared to pten-null ATG7 competent mice.[89] Further, Gammoh and colleagues showed that siRNA targeting Atg7, Atg13, or Ulk1 strongly reduced K-Ras driven glioblastoma development *in vivo* and *in vitro*.[90] Autophagy has appears to enhance not only survival of primary tumor cells, but also tumor cell intravasation to the circulation and subsequent metastasis to distal tissues.[79,91,92] Peng and colleagues showed that lentivirus-mediated silencing of ATG5 or BECN1 in a mouse model of hepatocellular carcinoma significantly reduced the incidence of pulmonary metastasis compared to the wildtype HCC mice.[91] Katheder and colleagues demonstrated in Drosophila that tumor

growth and invasiveness depends on autophagy induction in the tumor microenvironment.[93] All this taken together paints a different picture of the relationship between autophagy and cancer. In the absence of malignancy, autophagy appears to be a protective mechanism which may prevent tumorigenesis. However, in the setting of advanced malignancies, autophagy may provide a benefit to the developed cancer, enhancing tumor growth and even metastasis.

As such, over the past decade, significant work has been done to assess the clinical benefit of pharmacologic autophagy inhibition in advanced and aggressive malignancies. Clinical trials combining autophagy inhibition with standard of care therapies have demonstrated enhanced benefit for patients with difficult to treat cancers, including glioblastoma and pancreatic ductal adenocarcinoma.[94–96] For example, in a randomized controlled clinical trial of patients with glioblastoma multiforme, patients treated with a daily 150 mg dose of chloroquine (a nonselective inhibitor of autophagy) with standard of care chemotherapy, temozolomide and radiation had an average overall survival of 33 months, compared to 11 months for those treated with only the standard of care.[94] Chloroquine and hydroxychloroquine, FDA approved anti-malarial agents, have demonstrated potent inhibition of autophagic flux through their shared mechanism of lysosomal deacidification. As a result, these have been the primary inhibitors tested in cancer clinical trials. While this mechanism of action results in an inability of autophagosomes to degrade their contents via lysosomal fusion, it results in more than just autophagy inhibition. Loss of lysosomal acidification additionally halts the breakdown of other materials in late endosomes and multivesicular bodies that depend on lysosomal activity. These inhibitors are also not free of side effects. Chloroquine and hydroxychloroquine use can lead to hypoglycemia, aplastic anemia, thrombocytopenia, retinopathy, and hearing loss. Additional ways to inhibit autophagy that have been used

frequently in preclinical studies include bafilomycin, a vATPase inhibitor that, like chloroquine analogs, results in increased lysosomal pH, as well as 3-methyl adenine, a nucleotide analog that inhibits class III PI-3Ks.[97] Given these strategies for inhibition are not selective for autophagy, more selective inhibitors of autophagy are still needed. It is possible that results seen in various cancers with genetic knockdown of autophagy proteins may be replicated pharmacologically with more selective inhibitors. Further, chemical probes inhibiting autophagy mechanisms more selectively would be an invaluable resource for the study of autophagy and its role in cancer.

1.2.3. Targeting LC3 and its Many Isoforms

One strategy to achieve a more autophagy-selective inhibitor is to target LC3, a protein central to the process of autophagosome maturation. LC3 comprises a small class of paralogs within a larger subset of so-called ATG8 proteins. Mammalian ATG8 proteins are broken down into two classes, LC3s (in humans, comprised of LC3A, LC3B, and LC3C) and GABARAPs (in humans, comprised of GABARAP, GABARAPL1 and GABARAPL2). LC3B shares over 90% sequence homology with LC3A and over 70% with LC3C. Meanwhile, it shares between 59-65% for the GABARAP isoforms.[98] While some functions of these proteins seem to overlap, it is becoming increasingly clear that these different isoforms have some differentially regulated activities and distinct targets. For example, of the 67 proteins identified to interact with the different ATG8 isoforms, roughly one third are shared between all isoforms, a third interact only with GABARAPs and a third interact only with LC3s.[99] Developing inhibitors of individual isoforms or classes of ATG8 would allow for better understanding of the differences in function between these isoforms. Genetic knockout experiments have demonstrated that while both GABARAPs and LC3s contribute to autophagy, LC3s appear more responsible for autophagosome elongation, while GABARAPs are more responsible for autophagosome membrane closure.[100]

Further, GABARAPs but not LC3s appear critical in later stages of autophagy, being necessary for mediating key interactions required for autophagosome-lysosome fusion.[101] LC3s play a more prominent role in mitophagy, the autophagic breakdown of mitochondria, which is required for mitigating accumulation of reactive oxygen species. Work by Lazarou and colleagues suggested that LC3s are recruited to the mitochondrial membrane, but that GABARAPs have no involvement in the process.[102] However, more recent evidence has challenged this notion, finding GABARAPs a required component for mitophagy.[101]

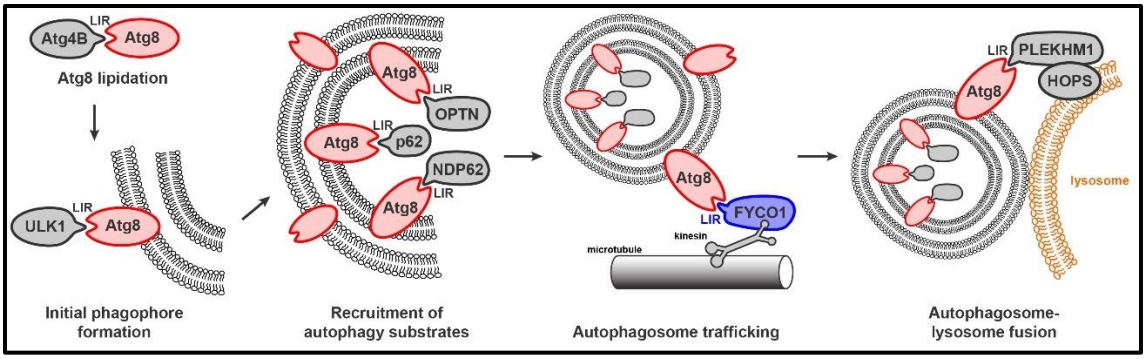

Fig 1.5. Critical Atg8 interactions in the autophagy pathway mediated by LIR motifs. LIR motifs are responsible for docking ULK1 during early phagophore initiation,[103,104] for Atg8 lipid conjugation,[105] for selective recruitment of cargo receptors,[106,107] for autophagosome transport,[108] and ultimately for autophagosome-lysosome fusion.[101,109]

There are several important findings that support the development of inhibitors that selectively inhibit LC3 proteins, LC3B in particular, while avoiding inhibition of GABARAPs. Von Hippel Lindau (VHL), a tumor suppressor protein that is deleted in most clear cell renal carcinomas, is responsible for the upregulation of miR-204. Mikhaylova and colleagues identified LC3B as a direct target of miR-204, and found a positive correlation between LC3B expression levels and higher tumor grade.[110] Meanwhile, authors also identified that VHL expression resulted in increased LC3C levels, which were also responsible for tumor growth suppression.[110] Being able to inhibit LC3B while leaving

LC3C unhindered could provide a more efficacious route to anti-tumor autophagy inhibition in clear cell renal carcinoma. GABRAP itself has also been identified as a tumor suppressor protein. For example, GABARAP levels were found to be significantly suppressed in a number of breast cancer cell lines, including the triple negative cal51 cell line.[111] Reconstituting GABARAP in xenograft mice models was able to significantly impair tumor growth. Additionally, GABARAP has been identified not only to be protective against tumor growth, but also, tumor invasiveness. Genau and colleagues demonstrated that GABARAP was critical for the ubiquitinylation and subsequent degradation of the TIAM1 protein, an activator of RAC1 signaling which is a key protein involved in cell motility and invasion.[112] Being able to avoid the tumor suppressive and anti-invasive benefits of select ATG8 isoforms while still inhibiting autophagy could provide additional benefit in the study of autophagy and cancer.

1.2.4. LIR Motif Peptides as Selective Autophagy Inhibitors

Once LC3/GABARAP is conjugated with PE and incorporated into the developing autophagosome membrane, it is capable of binding many different proteins. These include core autophagy machinery required for maturation and closure of the developing autophagosome, adapters, transporters, and specific cargo and organelles to be targeted for degradation.[113] Many of these proteins bind LC3 via an LC3-interacting region, or “LIR” motif. This motif typically consists of the core consensus [W/F/Y]-X-X-[L/I/V], with the residues at positions 1 and 4 engaging with two hydrophobic pockets on the target ATG8 surface.[113]

Many LIR motifs exhibit different preferences for binding ATG8 isoforms. Multiple recent publications have surveyed the landscape of LIR motifs and identified binding affinities and preferences of these LIR peptides to each of the ATG8 proteins.[114–116] For example, Atkinson and colleagues, using Time-Resolved FRET, looked at the affinities of 14

different LIR peptides for all six human ATG8 paralogs.[116] Many of the trends identified were well-supported in the literature, such as FYCO1 demonstrating a strong preference for LC3A and LC3B,[117,118] and ULK1 having a strong preference for the GABARAP subfamily over the LC3s.[104] Using biolayer interferometry, Wirth and colleagues measured K_d values for a number of GABARAP-selective LIR peptides, including Ulk1, with K_d values of 50 and 48 nM for GABARAP and GABARAP-L1 respectively, compared to 2.5 - 48.2 µM for the LC3 orthologs.[115] Some of the most interesting and high-affinity LIR peptides reported to date were described by Li and colleagues, derived from the giant ankyrin proteins.[114] These peptides, derived from two neuron-specific ankyrin proteins, termed AnkG and AnkB, are considerably longer in length than the average LIR motif with an additional 10 residues within the C-terminal helix. Interestingly, these long peptides displayed very potent affinity. AnkG was very selective for the GABARAP subfamily, with K_d values of 2.6 – 40 nM compared to 339 – 2930 nM for the LC3s. Meanwhile, AnkB displayed less selectivity, binding binding GABARAPs with K_d values of 0.21 – 0.29 nM and LC3s with 3.7 – 10.5 nM.[114] The authors attributed this improved binding affinity over shorter LIR motifs to the amphipathic, extended C-terminal alpha helix.[114,119]

One LIR motif that is particularly relevant to the work described in chapter 3 is derived from the FYVE and coiled coil protein 1 (FYCO1). FYCO1 is known to play a role in trafficking late endosomes and autophagosomes, acting as an adapter protein that binds Rab7 and kinesin to move cargo along microtubules in a kinesin-dependent, plus-end direction.[108,117] Johansen and colleagues demonstrated a direct binding interaction between FYCO1 and LC3B at the autophagosome membrane that was necessary for autophagosome maturation. When FYCO1 was knocked down or when FYCO1 was expressed with a mutated LIR motif, it led to reduced autophagic flux compared to wild-type FYCO1. Further, Cheng and colleagues demonstrated that this independent LIR motif

peptide sequence could bind the LC3B protein with a K_d of 190 nM as determined by isothermal titration calorimetry, making it a reasonably high-affinity peptide.[118] These works and others highlight the importance of the LIR motif for the necessary communication with ATG8 proteins that regulate autophagic flux. Importantly, multiple works have demonstrated that the FYCO1 LIR motif has a distinct preference for LC3A/LC3B over other ATG8 paralogs.[104,116–118] Ultimately, while there are several LIR motifs that bind LC3B with higher affinity than the FYCO1 LIR motif, the FYCO1 LIR motif represents the highest affinity starting point for an LC3-selective ATG8 inhibitor.

We reasoned that further study of FYCO1 LIR motif peptides would reveal new insights into the binding of LC3B. Such structure-activity information could allow for the generation of LC3-selective inhibitors with more drug-like properties, including improved binding affinity, improved stability, and better cell penetration. Inhibitors that selectively inhibit ATG8 isoforms would represent new tools for combination therapies in cancer.

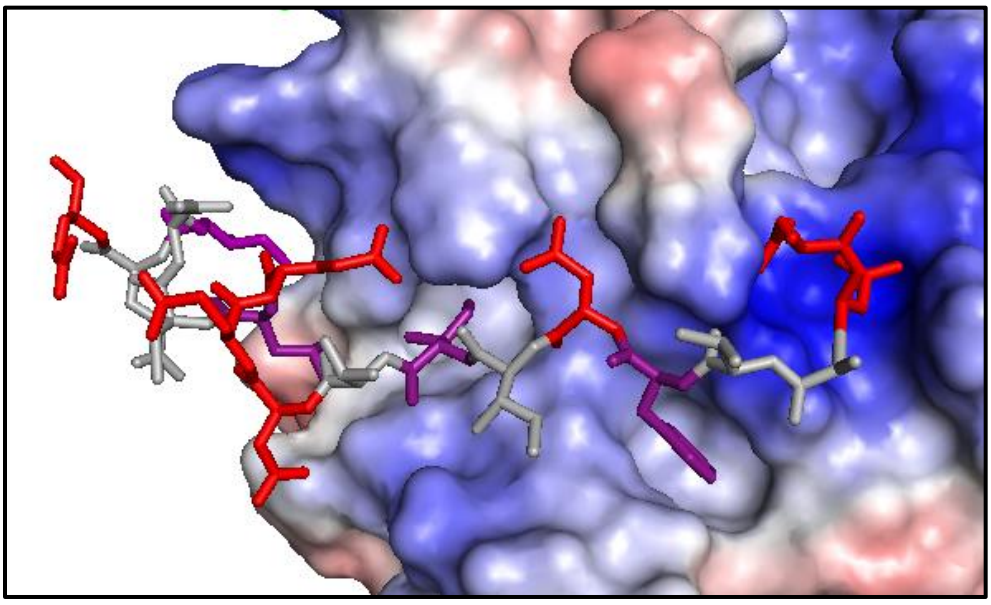

Fig 1.6. Crystal structure of FYCO1 LIR peptide binding LC3B protein. Highlighted are the seven negatively charged residues (red), and numerous hydrophobic residues (purple) including those targeting hydrophobic pockets HP1 and HP2 which we substitute throughout this work. (PDB: 5WRD)[120]

The work described in the manuscript in chapter 3 describes our efforts to study the FYCO1 LIR:LC3B interaction. We developed a broad set of structure-activity relationships which provided new insights for the generation of LC3B-selective inhibitors. Specifically, we studied the impact of N- and C-terminal truncations, as well as individual contribution of many negatively charged and hydrophobic residues. Further, we attempted to improve FYCO1 LIR peptide binding through the use of artificial amino acids and peptide macrocyclization via diversity-oriented peptide stapling. Our efforts generated LIR peptides with improved affinity and biological stability which also maintain the same LC3B/GABARAP selectivity profile as the native FYCO1 LIR.

Chapter 2: Cytosolic Delivery of Peptidic STAT3 SH2 Domain Inhibitors[1]

[1] Cerulli, RA., Shehaj, L., Tosic, I., Jiang, K., Wang, J., Frank, DA., Kritzer, JA. Cytosolic delivery of peptidic STAT3 SH2 domain inhibitors. Submitted to *Bioorg. Med. Chem.*, 3/20/20.

2.1. Introduction

The signal transducer and activator of transcription 3 (STAT3) protein is a transcription factor frequently dysregulated in hematological malignancies such as leukemias and lymphomas, as well as in solid tumors such as breast cancers, prostate cancers, and glioblastoma multiforme.[2,121,122] Cytokine stimulation with IL-6 or oncostatin M leads to phosphorylation of gp130, which recruits STAT3 to the cell membrane via its Src Homology 2 (SH2) domain. Once localized to the plasma membrane, STAT3 is phosphorylated by Janus kinases. Phosphorylated STAT3 dimerizes via its SH2 domains, and the dimer translocates to the nucleus where it acts as a transcription factor.[1,2] STAT3 upregulates numerous genes critical for cancer cell survival, including: survivin, Bcl-2, and Bcl-xL, which allow evasion of apoptosis; VEGF, which promotes angiogenesis; MMPs, which enhance cell motility; and PD-L1, which allows for immune evasion.[3–6,8] Importantly, STAT3 was shown to be necessary for malignant transformation of mouse fibroblasts, but not for normal fibroblast growth, suggesting a potential therapeutic window as a cancer target.[7]

Membrane localization and dimerization are both critical steps in STAT3 activity, and both require the function of the STAT3 SH2 domain. This has prompted the hypothesis that inhibitors of the STAT3 SH2 domain could block STAT3 activity.[13,123] However, SH2 domains are challenging targets for drug discovery. SH2 domains recognize phosphotyrosine (pTyr)-containing sequences, yet pTyr is rapidly hydrolyzed in the cytosol by protein tyrosine phosphatases. Additionally, pharmacological agents with pTyr have poor cytosolic penetration, which is typically ascribed to their multiple negative charges.[19] Numerous pTyr isosteres have been developed over the last several decades in order to address these issues. Phosphonates, including phosphonomethyl phenylalanine (Pmp) and difluorophosphonomethyl phenylalanine (F_2Pmp), have been

applied as phosphatase-stable SH2 domain inhibitors.[20,21,23] However, these and other pTyr isosteres still have multiple negative charges, and typically still suffer from poor cytosolic delivery.[19]

Cell-penetrating peptides (CPPs) offer a promising solution for the cytosolic delivery of peptidomimetics containing pTyr or pTyr isosteres.[66–68] CPPs including Tat, polyarginine, and penetratin have been used to deliver peptides containing pTyr and pTyr isosteres, resulting in inhibition of various SH2 domains and protein tyrosine phosphatases.[69–73] Most of these prior efforts delivered phosphopeptides, which are prone to dephosphorylation in serum (vide infra) and in the cytosol. A handful of prior efforts have incorporated pTyr isosteres to prevent phosphate hydrolysis.[72,73] For example, Watson and colleagues developed a bicyclic peptide inhibitor of the Grb7 SH2 domain containing a carboxyphenylalanine (cF) residue, and conjugated it to penetratin to promote cell uptake. This peptide inhibited Grb7 binding to FAK, HER2, and SHC in SKBR3 breast cancer cells when assessed by coimmunoprecipitation.[72] Additionally, Lian and colleagues incorporated F_2Pmp into a bicyclic peptide targeting the phosphatase PTP1B, in which one macrocycle incorporated the binding motif and the other incorporated a cyclic CPP, cyclo(FφR$_4$) where φ is 2-naphthylalanine. This peptide produced a two-fold increase in insulin receptor phosphorylation in HepG2 liver cells when applied at 200 nM.[73] These studies demonstrated that combining non-hydrolyzable pTyr isosteres, macrocyclization, and CPPs, one can develop relatively potent and cell-penetrant inhibitors of SH2 domains and protein tyrosine phosphatases.

Based on this prior work, we sought to apply a similar strategy to the inhibition of STAT3. To take advantage of recent advances in CPP development,[74–76] we chose to apply an improved version of cyclo(FφR$_4$), CPP12, to deliver STAT3-targeted peptides to the cytosol. CPP12 was demonstrated by Qian and colleagues to improve cytosolic delivery

efficiency by 6-fold compared to cyclo(FφR$_4$), and 30 to 60-fold compared to polyarginine and Tat, respectively.[74] We found that STAT3-selective binding sequences from gp130 could be substituted with F_2Pmp and maintain micromolar binding affinity for STAT3. Since micromolar inhibitors of STAT3 have been shown to be effective in cellular models of STAT3 activation, we tested CPP12-fused peptides to measure their effects on STAT3 activity in relevant STAT3-driven cancer cell lines. When the peptides did not act as effective STAT3 antagonists, we followed up by quantitatively measuring the serum stability, cell lysate stability, and cytosolic penetration of selected CPP12 fusions, producing a rich data set that addresses the delicate balance that must be achieved between target affinity, resistance to degradation, and cytosolic penetration for pTyr-mimetic SH2 domain inhibitors.

2.2. Results

We began by directly substituting pTyr with phosphonomethyl phenylalanine (Pmp) in a previously described, high-affinity STAT3-binding peptide derived from gp130.[124] We prepared fluorescein-labeled versions of the native pTyr peptide (flu-pTyr) and the Pmp-containing analog (flu-Pmp) to permit direct fluorescence polarization (FP) binding assays. flu-pTyr bound recombinant STAT3 with a K_d of 60 nM (**Fig 2.1a**, **Fig 2.4a-c**), consistent with previously observed binding affinities.[124] However, flu-Pmp showed poor binding even at micromolar protein concentrations; this represented over a 100-fold loss in binding affinity (**Fig 2.1a**). We concluded that Pmp was not a suitable replacement for pTyr in the context of this STAT3-SH2 ligand.

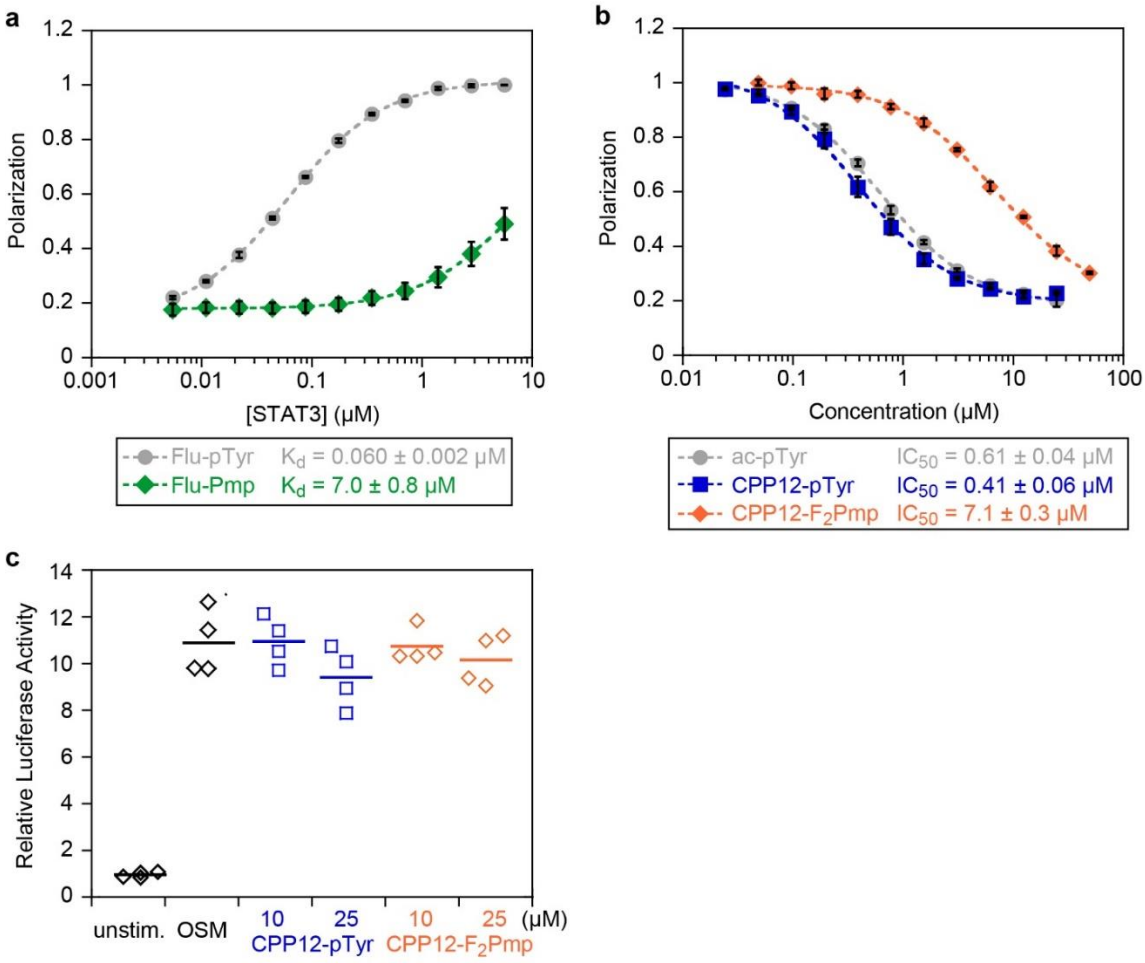

Figure 2.1. Binding affinities and cellular STAT3 inhibition of selected peptides. a) Fluorescence polarization binding data for selected peptides with recombinant STAT3. Fluorescein-labeled peptides were incubated at 10 nM with serial dilutions of STAT3 at room temperature for 45 min. Data points represent the averages of three biological replicates, each performed with three technical replicates, normalized to the maximum observed polarization (raw data shown in **Fig. 2.4**). Error bars show standard error of the mean for the three biological replicates. K_d values are the mean and standard error of the mean for three independent K_d curve fits to the three biological replicates. b) Competition FP for selected peptides with STAT3. flu-pTyr was incubated at 10 nM with 300 nM STAT3 protein and serial dilutions of peptide inhibitors at room temperature for 45 min. Data points represent the averages of three biological replicates, each performed with three technical replicates, normalized to the no-inhibitor control (raw data shown in **Figs. 2.5, 2.6**). Error bars show standard error of the mean for the three biological replicates. IC_{50} values are the mean and standard error of the mean for three independent curve fits to the three biological replicates. c) STAT3 transcription inhibition. STAT3-luc U3A fibrosarcoma cells were pretreated with 10 or 25 μM of CPP12-pTyr and CPP12-F_2Pmp for 24 hours at 37 °C in DMEM supplemented with 10% FBS, followed by 6 hour stimulation with OSM (10 ng/mL). Controls included OSM-treated cells without peptide, and unstimulated cells. This experiment was performed with two biological replicates, each with two technical replicates (all four values displayed).

We anticipated that fusion to a CPP might alter binding affinity, so we prepared CPP12-pTyr, a pTyr-containing g130 sequence fused to CPP12 (**Fig 2.2**). CPP12 was synthesized N-terminal to the gp130-derived sequence with a linker of two β-alanines.[74] Because CPP12 uses the N-terminus for cyclization, we did not attach fluorescein to these peptides, and instead used the competition FP assay to measure competitive inhibition of the STAT3-gp130 phosphopeptide interaction. CPP12-pTyr inhibited this interaction slightly better than ac-pTyr, with IC_{50} values of 410 nM and 610 nM, respectively (**Fig 2.1b**). This demonstrated that fusion to CPP12 did not greatly impact the inhibitory potency. Next, we substituted pTyr with difluorophosphonomethyl phenylalanine (F_2Pmp), a pTyr isostere that has shown improved properties over Pmp for SH2 domain binding.[21–23] CPP12-F_2Pmp had an IC_{50} of 7.12 μM, which was 17-fold less potent than CPP12-pTyr (**Fig 2.1b**).

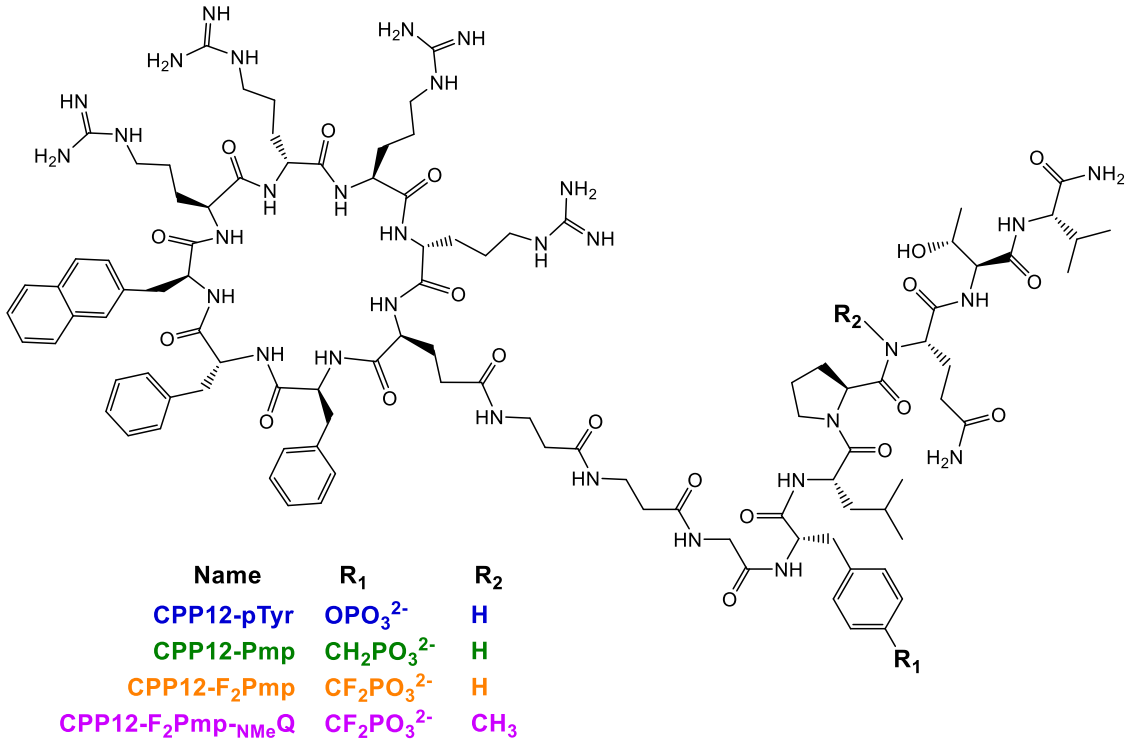

Figure 2.2. Structures of CPP12-conjugated STAT3 SH2-targeting peptides.

While CPP12-F_2Pmp was less potent than CPP12-pTyr, this was a significant improvement over the Pmp-containing peptide and merited additional characterization. Next, we tested CPP12-pTyr and CPP12-F_2Pmp in a STAT3 transcriptional reporter assay in a U3A fibrosarcoma cell line.[125] However, even at 25 μM peptide incubated for 24 hours, neither CPP12-pTyr nor CPP12-F_2Pmp inhibited OSM-stimulated STAT3 activity (**Fig 2.1c**). There are multiple examples in the literature of small molecule STAT3 SH2 domain inhibitors with single- to double-digit micromolar IC_{50} values when tested *in vitro* under the same conditions as our STAT3 fluorescence polarization assay, yet display potent cell-based phenotypes.[37,38] As such, the lack of an observable phenotype with our peptides led us to investigate what barriers were responsible.

One possibility was that CPP12 was not sufficiently delivering the peptide into the cytosol. The Kritzer lab previously reported an assay for quantitatively comparing the cytosolic delivery of peptides and other biomolecules.[126] This assay, called the Chloroalkane Penetration Assay or CAPA, uses a HeLa cell line that stably expresses HaloTag in the cytosol to measure the relative cytosolic penetration of molecules labeled with a small chloroalkane tag. We prepared a representative CPP12-linked peptide with a chloroalkane tag (CPP12-Pmp-ct, **Fig. 2.8a**) as well as a non-CPP-linked analog ct-Pmp. The cytosolic delivery of these peptides were compared to control molecules ct-W, a small-molecule with excellent cytosolic penetration, and ct-Tat, a molecule with moderate cytosolic penetration.[126] ct-Pmp showed little cytosolic delivery except at the highest concentration tested (25 μM), while CPP12-Pmp-ct showed substantial cytosolic delivery at concentrations above 750 nM. By fitting IC_{50} curves to the dose-dependence data, we have derived "CP_{50} values" which allow direct, quantitative comparison of the extent of cytosolic delivery. CPP12-Pmp-ct had a CP_{50} value of 720 nM, while the Pmp-containing peptide without CPP12 (ct-Pmp) had a CP_{50} value of 18.9 μM (**Fig 2.3a**). A

chloroalkane-linked version of the commonly used CPP Tat (ct-Tat) had a CP_{50} value of 7.74 μM under these conditions (**Fig 2.3a**). These data indicated that fusion to CPP12

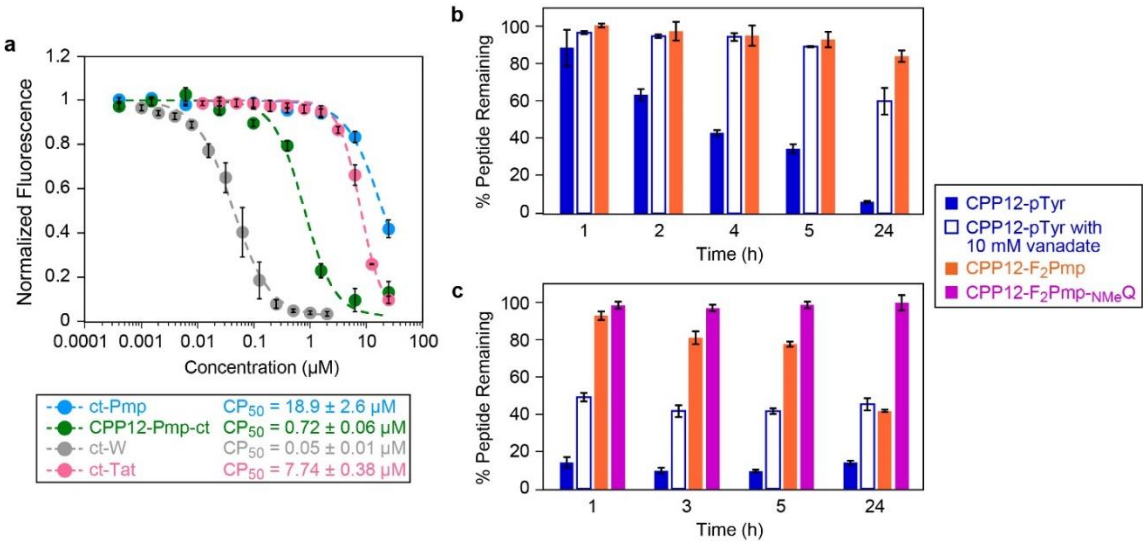

Figure 2.3. Cytosolic penetration, serum stability, and cell lysate stability of selected CPP12-gp130 peptide fusions. a) Chloroalkane penetration assay with CPP12-Pmp-ct (structure shown in **Fig 2.8a**), non-CPP-linked peptide ct-Pmp, and control molecules ct-Tat and ct-W. The figure shows data normalized to the no-molecule control (100% fluorescence), which indicates signal when no molecule accessed the cytosol, and no-dye control (0% fluorescence), which indicates signal if 100% of cytosolic HaloTag was blocked by chloroalkane-tagged molecules. Data show averages of three biological replicates (four biological replicates for CPP12-Pmp-ct), and within each biological replicate each data point represents the mean red fluorescence of 5,000 cells. CP_{50} values are reported as the mean and standard error of the mean for three separate curve fits to the three biological replicates (individual replicates shown in **Fig. 2.8b-d**). b) Serum stability assay for selected CPP12-gp130 peptides. Peptides were incubated for various time points in DMEM supplemented with 10% FBS at 37 °C, with and without 10 mM sodium orthovanadate. Areas under each peptide chromatogram peak were normalized to the area under the zero timepoint chromatogram peak. c) Lysate stability assay for selected CPP12-gp130 peptides. Peptides were incubated for various time points in HeLa cell lysate at 37 °C, with and without 10 mM sodium orthovanadate. Areas under each peptide chromatogram peak were normalized to the area under the zero timepoint chromatogram peak.

improved cytosolic delivery of the Pmp-containing peptide by roughly 20-fold, and the CPP12-linked anionic peptide was roughly 10-fold more cytosolically penetrant than cargo-free Tat peptide. Because this assay was performed in serum-free medium and the STAT3 reporter assay was performed in DMEM with 10% FBS, we repeated CAPA in DMEM with 10% FBS and observed no difference in cytosolic penetration (**Fig. 2.8e**).

The CAPA data indicated that CPP12-gp130 fusions with pTyr isosteres effectively access the cytosol when incubated at high nanomolar to low micromolar concentrations for 4 hours or longer. Thus, we concluded that the CPP12 cell-penetrating peptide was likely sufficient to deliver the anionic gp130-derived peptides into the cytosol under the conditions used for the cell-based assays.

Another potential barrier to cellular activity is degradation, either in serum or within cells. We investigated the first possibility by measuring degradation of selected CPP-gp130 peptides in serum-containing media. We incubated CPP12-pTyr and CPP12-F_2Pmp at 150 μM in DMEM with 10% FBS, took aliquots at various time points over the course of 24 hours, and analyzed those samples via reverse-phase HPLC. In serum, the CPP12-pTyr peptide was degraded by almost 50% at 4 hours, and it was almost completely absent at 24 hours (**Fig 2.3b, Fig 2.9a**). Mass spectrometry analysis revealed that the primary product was the dephosphorylated peptide (**Fig 2.10a,b**). When the serum stability assay was repeated in the presence of 10 mM sodium orthovanadate, a general inhibitor of protein tyrosine phosphatases, dephosphorylation was blocked, with nearly 60% of CPP12-pTyr still intact after 24 hours (**Fig 2.3b**, **Fig 2.9b**). Consistent with these results, CPP12-F_2Pmp showed little degradation, even after 24 hours in serum (**Fig 2.3b, Fig 2.9c, 2.10c,d**).

Testing peptide stability in a cell lysate was recently reported as a particularly demanding assay for benchmarking the cellular stability of peptide therapeutics.[127] When tested in HeLa cell lysate, CPP12-pTyr was degraded much more quickly than in serum-containing media, with less than 20% of the original peptide remaining after just 1 hour (**Fig 2.3c**). This process could be slowed but not completely prevented with the addition of sodium orthovanadate (**Fig 2.3c**). Mass spectrometry revealed that, in the first hour of incubation, CPP12-pTyr is rapidly dephosphorylated. Following

dephosphorylation, the peptide undergoes proteolysis at multiple positions including at the tyrosine generated by pTyr dephosphorylation (**Fig 2.11a, 2.12a**). CPP12-F_2Pmp was more stable in cell lysate, with about 80% of the peptide remaining after 5 hours and 50% remaining after 24 hours of incubation (**Fig 2.3c, Fig 2.11b**). Interestingly, while CPP12-pTyr had numerous end products consistent with proteolysis at multiple positions, the mass spectrometry data revealed that CPP12-F_2Pmp was proteolyzed at a single site. Specifically, this peptide was cleaved just N-terminal to the glutamine residue (**Fig 2.12b**).

In order to slow the intracellular degradation of CPP12-F_2Pmp, we substituted the glutamine residue with N-methyl glutamine. This peptide, CPP12-F_2Pmp-$_{NMe}$Q, was completely resistant to degradation in cell lysate at 24 hours (**Fig 2.3c, Fig 2.11c, 2.12c**). Therefore, substitution of just two artificial amino acids (the pTyr isostere F_2Pmp and a single N-methyl glutamine) produced a cell-permeable peptide with considerable stability to degradation by intracellular enzymes. Finally, we tested CPP12-F_2Pmp-$_{NMe}$Q in the STAT3 luciferase reporter assay (**Fig 2.7a,b**), as well as a 72-hour viability assay in the STAT3-dependent MDA-MB-468 breast cancer cell line.[128] However, at 25 μM no activity was observed in either assay (**Fig 2.13**). The cause of this was revealed when we tested CPP12-F_2Pmp-$_{NMe}$Q in the competition FP assay. CPP12-F_2Pmp-$_{NMe}$Q had very poor STAT3 binding affinity (**Fig 2.6a-c**), so despite its high stability, it was unsuitable for further development as a STAT3 inhibitor.

2.3. Discussion

In this work, we sought to use CPP12 to enhance cellular delivery of peptides containing pTyr and pTyr isosteres, with the goal of producing more effective inhibitors of the STAT3 SH2 domain. Despite extensive development of STAT3 SH2 inhibitors, and prior applications of CPPs to deliver pTyr-mimicking peptides, to the best of our knowledge

there are no reported efforts to develop CPP-peptide fusions to inhibit STAT3-SH2 in living cells. We quantitated the STAT3 affinity and cytosolic delivery of these CPP12 conjugates, evaluated their stability in cell lysate and serum, and measured their activity in cell culture. The medicinal chemistry of peptidomimetic pTyr isosteres has always required a difficult balance among cellular stability, cytosolic penetration, and target affinity.[19] In this work, we directly measure each of these properties for CPP-linked peptides containing pTyr and pTyr isosteres.

We observed that the substitution of the pTyr with F_2Pmp within the native gp130 sequence led to a 17-fold loss in STAT3 affinity, while substitution with Pmp led to over 100-fold loss in affinity. This generally matches previous reports examining Pmp and F_2Pmp isosteres in other peptide-SH2 interactions, which showed large losses in affinity with Pmp but anywhere from 5-fold losses to 5-fold gains in affinity with F_2Pmp.[23] While Mandal and colleagues reported cellular effects on STAT3 activity using prodrug-functionalized 4-phosphonodifluoromethylcinnamate analogs of the gp130 sequence,[28,129] this is the first reported application of F_2Pmp to STAT3 inhibitors. It is possible that a similar prodrug approach could promote greater cytosolic penetration for gp130-derived peptides.

We chose to apply CPP12 because it was shown to be more efficient than older CPPs at delivering peptides and peptidomimetics, including negatively charged cargoes.[74–76,126,130,131] Since the delivery efficiency of CPP12 has been shown to vary depending on the cargo attached and the cell line employed, we used the chloroalkane penetration assay to conclusively demonstrate cytosolic delivery of a CPP12-gp130 fusion containing a pTyr isostere. These data must be interpreted carefully due to possible perturbations from the CPP, the linker between the CPP and the gp130-derived sequence, the pTyr isostere, and the chloroalkane group. Still, the data clearly show that

cytosolic delivery can be achieved for pTyr-isostere-containing peptides at concentrations as low as 720 nM. Considering that the small molecule control, ct-W, had a CP_{50} value of 50 nM under these conditions,[126,132] this is an impressive degree of cytosolic delivery for an anionic peptide. For comparison, the CPP12-fused peptide showed cytosolic localization at over 10-fold lower concentrations than Tat without cargo, and over 20-fold lower concentrations than a Pmp-containing control peptide without CPP12. Interestingly, while Song and colleagues observed significantly poorer uptake of CPP12 in media containing 10% FBS,[76] we observed no difference in uptake of CPP12-conjugated anionic peptides between serum-free media and media with 10% FBS (**Fig 2.8e**). Ultimately, while results can vary depending on the nature of the cargo and chemical tags, our results suggest that CPP12 is a viable delivery system for delivering small anionic peptides such as those containing pTyr and pTyr isosteres.

Serum and intracellular stability are also important considerations for peptidomimetic design, since biological degradation can severely limit efficacy.[127] We measured extent of degradation over 24 hours in serum and in cell lysates, including analysis of degradation products by mass spectrometry. Our results suggest that CPP12 itself is completely stable in serum and in the presence of cellular enzymes including lysosomal proteases. Additionally, these results highlight that phosphopeptides are dephosphorylated rapidly in serum, and even more rapidly by intracellular enzymes. Interestingly, protection from dephosphorylation provided a significant boost to proteolytic stability, implying that dephosphorylation likely precedes proteolysis in many cases. Further, we were able to completely block proteolysis of CPP12-F_2Pmp by incorporating a single N-methylated residue. These modifications allowed a 17-residue peptide, which was almost entirely degraded in cell lysate after 1 hour, to become completely stable under these conditions for 24 hours. Unfortunately, the N-methylation

greatly disrupted binding to STAT3, highlighting the difficulty in balancing target affinity and bioavailability.

Ultimately, the most difficult challenges for peptidomimetics containing pTyr isosteres continue to be cell permeability and proteolytic stability. Here we used quantitative measurements to better understand each of these properties for gp130-derived inhibitors of STAT3. While limited STAT3 affinity is the most likely reason for the lack of cellular activity, there are other potential causes including nonspecific binding to other proteins within the cell. If affinity is indeed the limiting factor, our data demonstrate that degradation-resistant, anionic SH2 domain inhibitors can be optimized for cytosolic delivery using advanced CPPs. We also anticipate application of this strategy to other SH2 domains that better tolerate F_2Pmp, such as PI-3K and Src, as well as cancer-relevant phopshotyrosine phosphatases.[23,133,134]

2.4. Methods

2.4.1. Peptide Synthesis

All peptides were synthesized via standard Fmoc solid phase peptide synthesis on an automated Tribute Peptide Synthesizer (Gyros Protein Technologies). Peptides were synthesized on low-loading Rink amide resin (substitution 0.36mmol/g) with deprotection in 20% piperidine in DMF, and coupling with 5 equiv. Each of amino acid, HBTU, and HOBt, and 10 equiv. of DIPEA. DMF washes were performed between each step. F_2Pmp was allowed to couple overnight to ensure complete coupling. For on-resin CPP12 synthesis and cyclization, C-terminally allyl-protected glutamate was coupled via its sidechain to the growing peptide. When synthesis of the linear CPP was complete, the allyl group was removed with three 15-minute incubations with 0.1 equiv. palladium tetrakis and 10 equiv. of phenylsilane in anhydrous DCM. After N-terminal Fmoc deprotection, the peptide was cyclized overnight in DMF with 5 equiv. PyBOP, 5 equiv.

HOBt, and 10 equiv. DIPEA.[74] To prepare chloroalkane-tagged peptides, an MTT-protected lysine was deprotected with two 10-minute incubations with 1% TFA in DCM. After DMF washes, 2.5 equiv. of chloroalkane tag was coupled with 2.5 equiv. of PyBOP and 6.5 equiv. of DIPEA in DMF for 1.5 hours. To prepare fluorescein-labeled peptides, 5 equiv. of 5,6-carboxyfluorescein were coupled overnight with 10 equiv. DIPEA in DMF. To couple N-methyl glutamine, 5 equiv. each of amino acid, HATU and 10 equiv. DIPEA were coupled for 30 minutes, followed by a second coupling with the same reagents. The subsequent deprotection in 20% piperidine was followed by a second deprotection with 2% piperidine and 2% DBU in DMF. The amino acid following the N-methyl glutamine was double-coupled as well. All peptides were globally deprotected and cleaved from resin using a TFA cleavage cocktail (95:2:2:1, TFA:H_2O:EDT:TIPS) for 3 hours. Following cleavage, peptides were diethyl ether precipitated and pelleted, followed by an additional diethyl ether wash and centrifugation. Peptides were then dried before resuspending in water/acetonitrile for reverse-phase HPLC purification on a preparative-scale C_8 column (Agilent Technologies) at a 5 – 100% acetonitrile in 30 min gradient. Masses were determined using MALDI-TOF mass spectrometry (Bruker Microflex). MALDI Matrix used was 10mg/mL α-cyano-4-hydroxycinnamate in 50/50 water acetonitrile with 0.1% TFA. Peptides were at least 95% pure as determined via analytical HPLC on a C_{18} column at a 5 – 100% acetonitrile in 20 min gradient. Following purification, peptides were lyophilized and resuspended in DMSO for working solutions, which were quantified based on absorbance at 280 nm (Thermo Scientific Nanodrop 1000). Observed masses of final products are given in supplemental figure S8.

2.4.2. Protein Expression

STAT3 protein was expressed and purified as described.[135] Rosetta BL21 E. coli were transfected with an expression plasmid for His6-STAT3 (codons 127-711). Transfected

cells were grown on kanamycin agar plates and colonies were selected and grown in LB culture medium. At an optical density of 0.6 to 0.8, 1 mM IPTG was added and cells were incubated for 3 hours at 37 °C. Cells were pelleted, resuspended in lysis buffer (50 mM Tris pH 8.0, 300 mM NaCl, 5 mM imidazole, 0.2% lysozyme, 1 protease inhibitor cocktail pellet (Roche), and 2.5U/mL universal nuclease (Pierce), sonicated and lysed, and the lysate was centrifuged to pellet debris. The protein was purified from clarified lysate using Ni-NTA resin by incubating protein with resin for 45 min at 4 °C, rinsing with wash buffer (50 mM Tris pH 8.0, 300 mM NaCl, 5 mM imidazole), and then eluting in 50 mM Tris pH 8.0, 300 mM NaCl, 250 mM imidazole at 4°C. The eluate was further purified by size exclusion chromatography using an automated FPLC system (AKTA, GE) on a Superdex S200 prep column in 10 mM HEPES pH 7.5, 50 mM NaCl, 1 mM EDTA, and 2 mM DTT. Protein fractions were analyzed via SDS-PAGE, and pure fractions were pooled together. Concentration of protein was quantified via absorbance at 280 nm and confirmed via BCA assay. Protein was stored in frozen aliquots at -80°C.

2.4.3. Fluorescence Polarization Assays

FP assays were performed as described.[124] For direct FP assay, fluorescent peptide was mixed at a final concentration of 10 nM with a serial dilution of STAT3 protein [5.6 µM to 0.0055 µM] in a final reaction volume of 50 µL in a black, flat-bottomed 384-well polypropylene plate (Greiner Bio-One). The buffer composition was 10 mM HEPES pH 7.5, 50 mM NaCl, 1 mM EDTA, and 2 mM DTT. The plate was incubated in the dark for 45 min at room temperature, then read at 494 nm excitation and 519 nm emission. Data was normalized to the maximum polarization observed (raw data shown in supplement). For competition FP assays, fluorescent probe at a final concentration of 10 nM was mixed with STAT3 protein at a final concentration of 300 nM and a serial dilution of inhibitor peptide [25 or 50 µM to 0.025 µM]. DMSO was normalized across the plate to a

final concentration not exceeding 0.5%. The final reaction volume was 50 µL in a black 384-well plate. The buffer composition was 10 mM HEPES pH 7.5, 50 mM NaCl, 1 mM EDTA, and 2 mM DTT. The plate was incubated in the dark for 45 min at room temperature before reading at 494 nm excitation and 519 nm emission. Data was normalized to the no inhibitor (maximum polarization) control. K_d and IC_{50} values were obtained from curve fits using KaleidaGraph graphic software as described.[136]

2.4.4. STAT3 Luciferase Reporter Assay

Luciferase reporter assay was performed as described.[125] STAT3-luc/U3A fibrosarcoma reporter cells were seeded in a 96-well plate at 10^4 cells per well overnight. Then, cells were treated with selected concentrations of peptide or vehicle [10 or 25 µM] for 1 or 24 hours at 37 °C, and then stimulated with OSM at 10 ng/mL for 6 hours at 37 °C. Luciferase activity was quantified using the Bright-Glo Luciferase Assay system (Promega) and a Luminoskan Ascent Luminometer (Labsystems).

2.4.5. Chloroalkane Penetration Assay

CAPA assay was performed as described.[126,132] Halo-GFP-Mito HeLa cells were cultured using DMEM + 10% FBS + 1% Pen/Strep + 1µg/mL puromycin. Cells were seeded in a 96-well plate at 1.0 x 10^5 cells/well and incubated overnight. Cells were then rinsed with Opti-MEM and treated with a serial dilution of peptides [25 µM to 0.0004 µM] or ct-W control [2 µM to 0.001 µM] in Opti-MEM for 4 hours. Media was aspirated and cells were washed with Opti-MEM. Cells were then treated with 5 µM ct-TAMRA for 30 minutes before washing and trypsinizing cells. Cells were pelleted and resuspended in PBS twice before resuspending in a final volume of 250 µL of PBS and transferring them to a 96-well plate for flow cytometry analysis (Guava EasyCyte 6HT-2L benchtop flow cytometer), gating for live cells and measuring 5000 cells per sample. Fluorescence was normalized to the ct-TAMRA treated (100% fluorescence) and untreated (0%

fluorescence) cells. ct-W and ct-TAMRA were prepared and characterized as described.[126]

2.4.6. Peptide Stability Assays

Serum stability assays were performed as described.[137] 10% FBS in DMEM was warmed to 37 °C prior to adding peptide. For lysate stability assays, HeLa cells were trypsinized, washed in PBS, and pelleted before treating with lysis buffer (50 mM Tris, 250 mM NaCl, 0.5% IGEPAL CA-630 detergent, pH 8.0) on ice for 15 min. Then, lysates were centrifuged for 10 min at 4 °C at 14,800 rpm and the clarified lysate was collected. Peptides were added to either the serum or the lysate to a concentration of 150 µM and were incubated at 37 °C. Aliquots of 40 µL were taken at each time point and quenched in 160 µL of ice-cold methanol. Samples were spun down for 10 min at 14,800 rpm prior to analysis via reverse-phase analytical HPLC on a C_{18} column (Agilent Technologies). Peptide chromatogram peaks were integrated to determine area under each curve. Areas for each timepoint were normalized to the zero-hour timepoint to determine percentage of peptide remaining. Data presented is the average of three biological replicates performed on different days. Peptide masses present in each sample were determined using MALDI-TOF mass spectrometry (Bruker Microflex).

2.4.7. Cell Viability Assay

Cell viability assay was performed as described.[128] MDA-MB-468 breast cancer cells were seeded 3 x 10^3 cells/well in white opaque 96-well plates overnight. Peptide or vehicle [10 or 25 µM] was added to a final volume of 100 µL and incubated at 37 °C for the specified time. Cell viability was assessed using the CellTiter-Glo Luminescent Cell Viability kit (Promega).

2.5. Supplemental Materials

Name	Sequence	Expected Mass [M+H$^+$]	Observed Mass [M+H$^+$]
ac-pTyr	ac-G(pTyr)LPQTV-NH_2	898.9	898.5
flu-pTyr	flu-G(pTyr)LPQTV-NH_2	1215.2	1214.9
flu-Pmp	flu-G(Pmp)LPQTV-NH_2	1213.2	1213.1
CPP12-Pmp-ct	cyclo(FfφRrRrE)-ßß-G(Pmp)LPQTV-ßß-K(Ct)W-NH_2	2986.9	2984.7
ct-Pmp	ct-WßßG(Pmp)LPQTV-NH_2	1489.1	1487.9
ct-TAT	ct-YGRKKRRQRRR-NH_2	1865.7	1864.9
CPP12-pTyr	cyclo(FfφRrRrE)-ßß-G(pTyr)LPQTV-NH_2	2226.5	2225.6
CPP12-F_2Pmp	cyclo(FfφRrRrE)-ßß-G(F_2Pmp)LPQTV-NH_2	2260.5	2261.2
CPP12-F_2Pmp-NMeQ	cyclo(FfφRrRrE)-ßß-G(F_2Pmp)LPQ*TV-NH_2	2274.5	2274.9

flu denotes N-terminal 5,6-carboxyfluorescein, ß denotes beta-alanine, φ denotes 2-naphthylalanine, K(ct) denotes lysine with side chain acylated with chloroalkane tag, ac denotes N-terminal acetyl, NH_2 denotes C-terminal amide
pTyr denotes phosphotyrosine, Pmp denotes phosphonomethyl phenylalanine, F_2Pmp denotes difluorophosphonomethyl phenylalanine, lowercase letters denote D-amino acids, Q* denotes N-methyl glutamine
cyclo() denotes lactam formation between the N-terminus and the C-terminus of the glutamate residue; side chain of glutamate is attached to N-terminus of the rest of the peptide. See[74] for details.

Table 2.1. Expected and observed masses for all peptides.

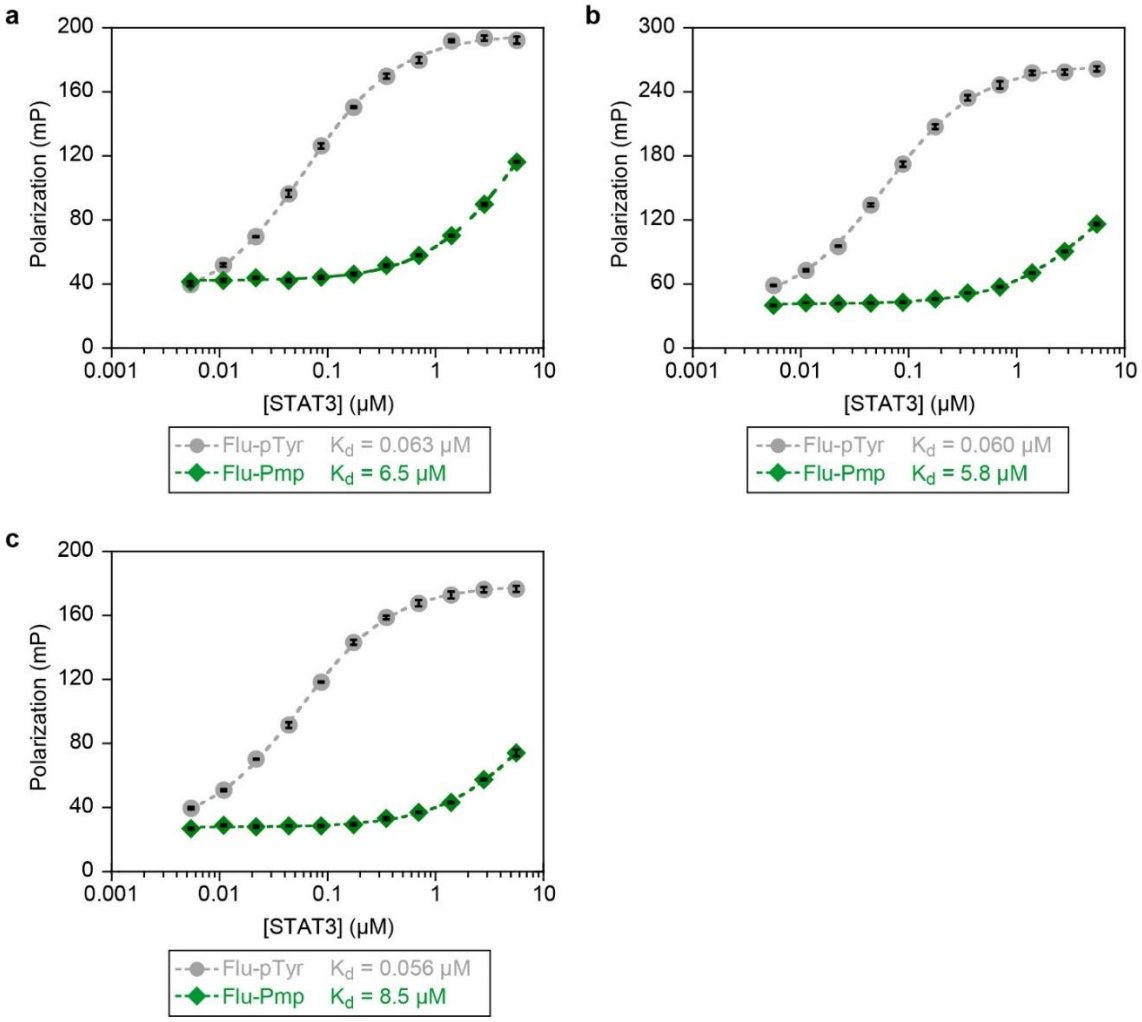

Figure 2.4. STAT3 binding affinities of selected peptides. a-c) Fluorescence polarization binding data for selected peptides with recombinant STAT3. Fluorescein-labeled peptides were incubated at 10 nM with serial dilutions of STAT3 at room temperature for 45 min. a-c each show raw polarization values for a biological replicate, each performed with three technical replicates. Averaged, normalized data shown in **Fig. 2.1a**. Error bars show standard error of the mean for the three technical replicates. K_d values are derived from independent K_d curve fits to each of the three biological replicates.

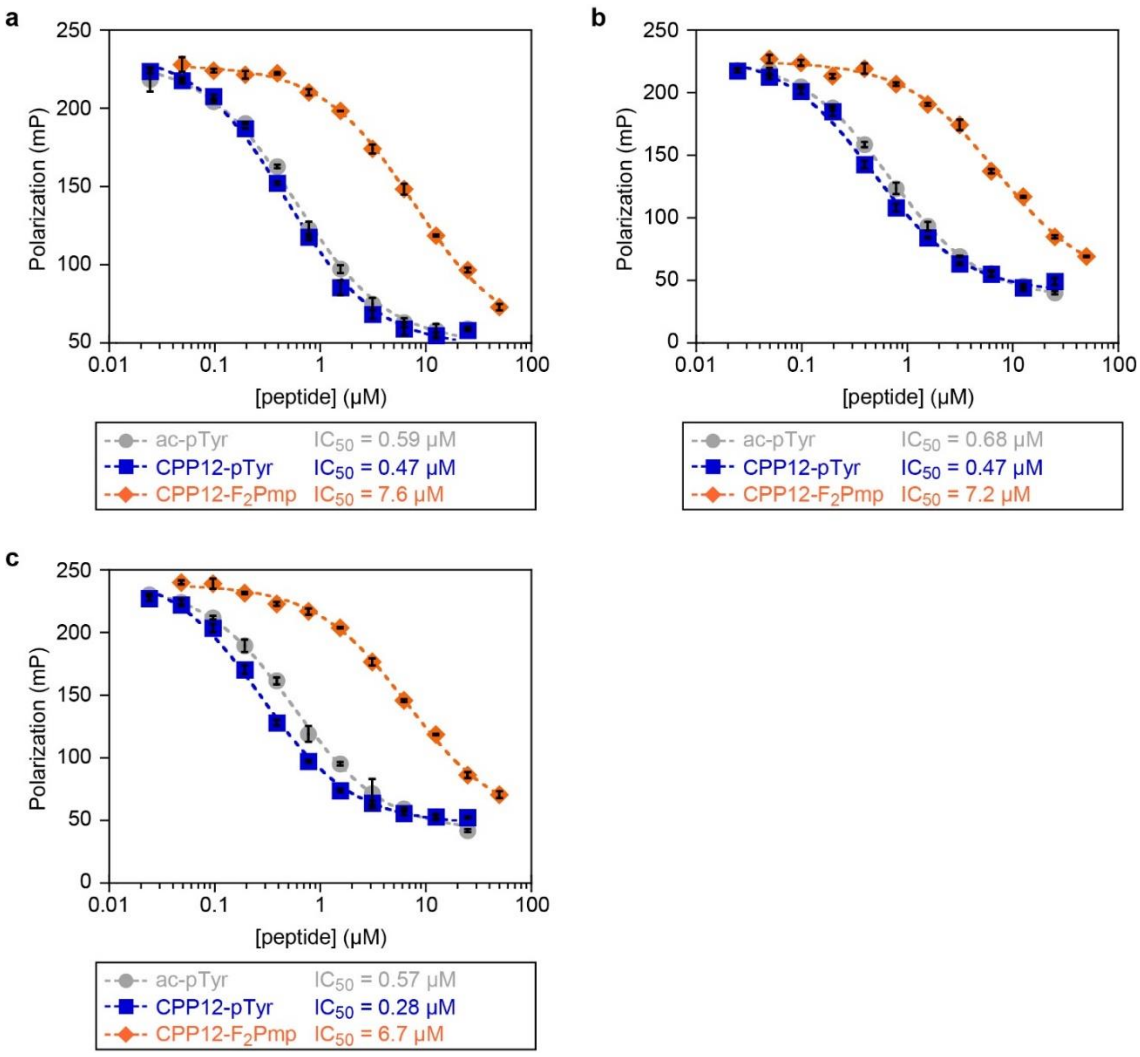

Figure 2.5. Competition FP for selected peptides with STAT3. flu-pTyr was incubated at 10 nM with 300 nM STAT3 protein and serial dilutions of peptide inhibitors at room temperature for 45 min. a-c each show raw polarization values of a biological replicate, each performed with three technical replicates. Averaged, normalized data are shown in **Fig. 2.1b**. Error bars show standard error of the mean for the three technical replicates. K_d values are derived from independent K_d curve fits to each of the three biological replicates.

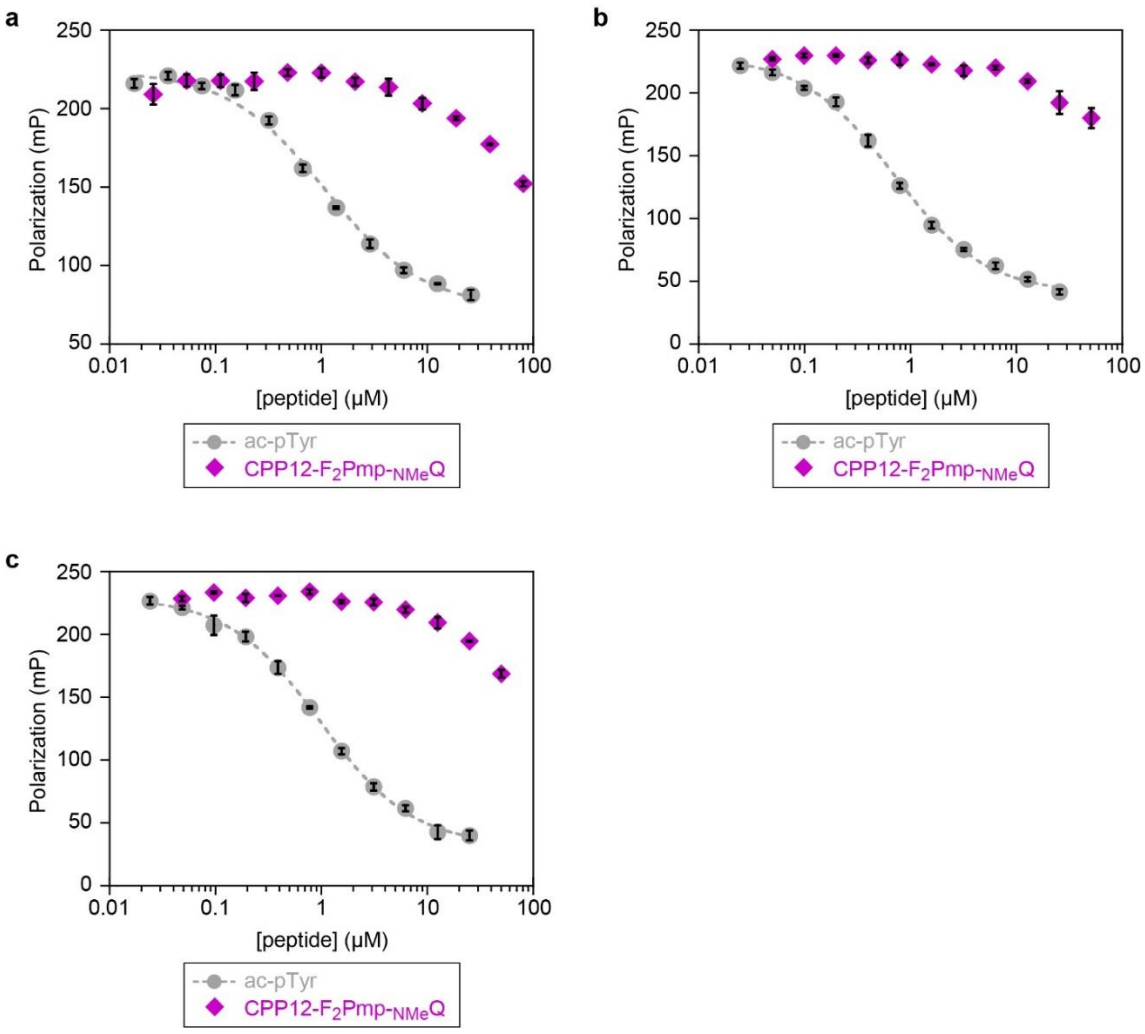

Figure 2.6. Competition FP for selected peptides with STAT3. flu-pTyr was incubated at 10 nM with 300 nM STAT3 protein and serial dilutions of peptide inhibitors at room temperature for 45 min. a-c each show raw polarization values of a biological replicate, each performed with three technical replicates. Error bars show standard error of the mean for the three technical replicates. K_d values are derived from independent K_d curve fits to each of the three biological replicates.

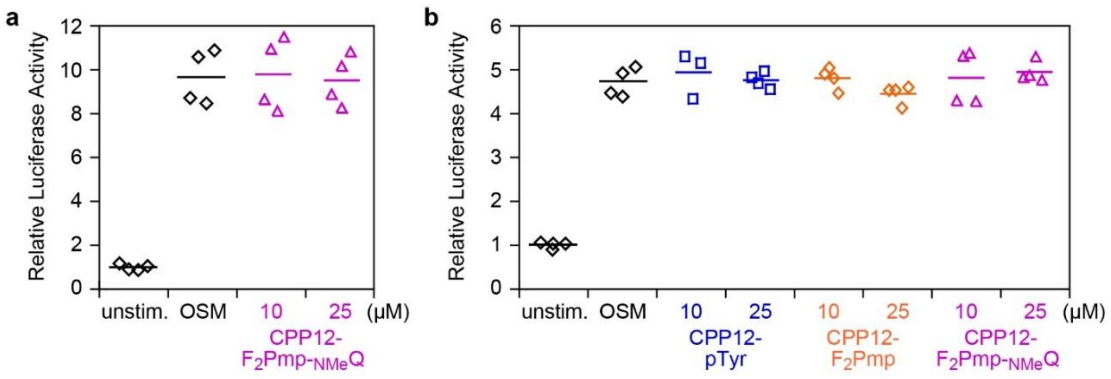

Figure 2.7. Cellular STAT3 inhibition of selected peptides. STAT3-luc U3A fibrosarcoma cells[125] were pretreated with 10 or 25 μM of selected peptides for 24 hours (a) or 1 hour (b) at 37 °C in DMEM supplemented with 10% FBS, followed by 6 hour stimulation with OSM (10 ng/mL). Controls included OSM-treated cells without peptide, and unstimulated cells. This experiment was performed with two biological replicates, each with two technical replicates (all four values displayed).

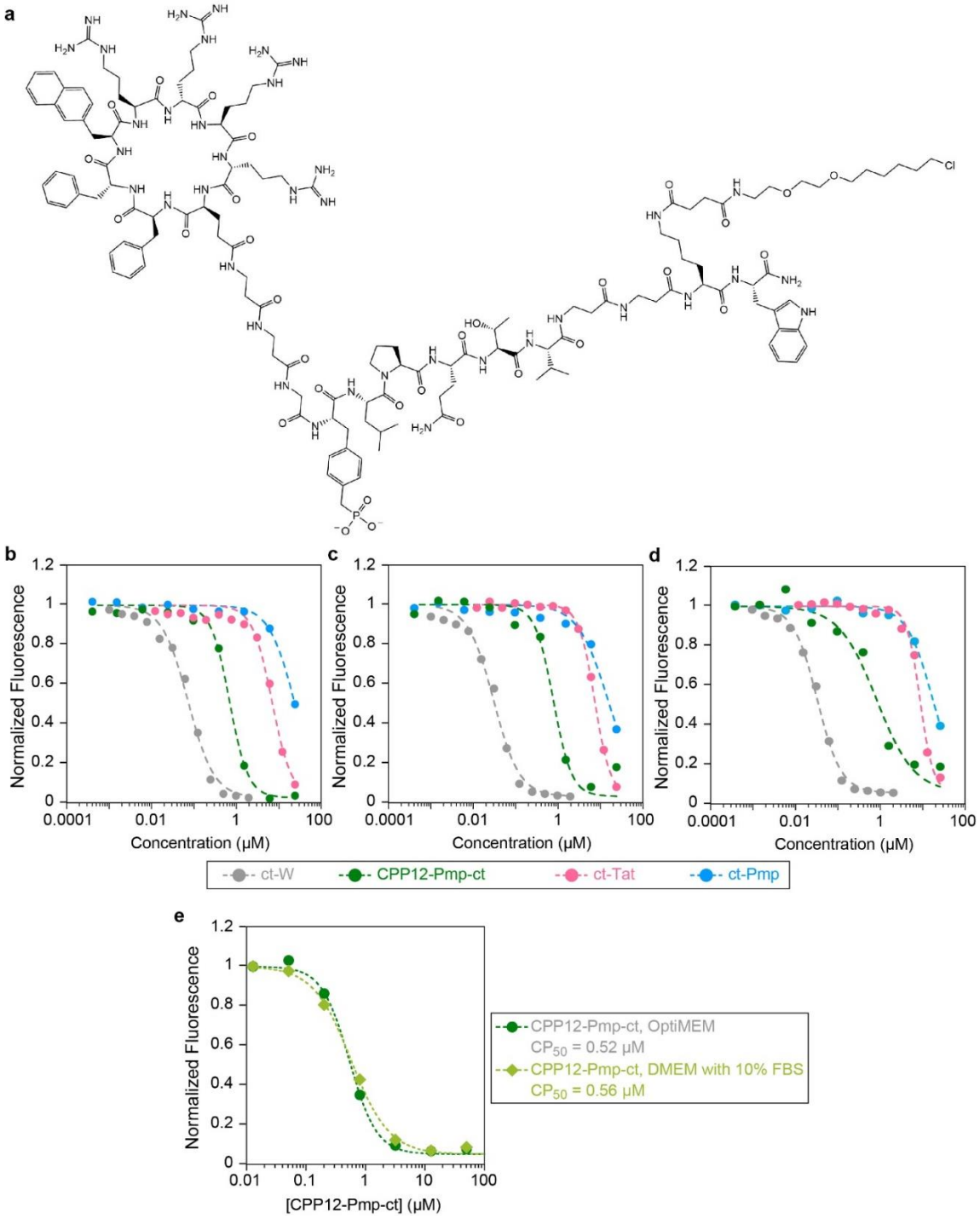

Figure 2.8. Cytosolic penetration of ct-Pmp, CPP12-Pmp-ct and control molecules. a) Chemical structure of CPP12-Pmp-ct. b-d) Chloroalkane penetration assay[126,132] with CPP12-Pmp-ct incubated with Halotag-expressing HeLa cells in Opti-MEM for 4 h at the indicated concentrations. The figures show data normalized to the TAMRA-only (100% fluorescence) and no TAMRA (0% fluorescence) controls, as described.[126,132] Each point represents the mean red fluorescence of 5,000 cells measured for that biological replicate. CP_{50} values are derived from independent CP_{50} curve fits to each of the three

biological replicates (averaged CP_{50} and standard error of the mean in **Fig. 2.3a**). e) Additional biological replicate of CPP12-Pmp-ct with a single biological replicate of this experiment comparing cytosolic delivery when incubated in Opti-MEM vs. 10% FBS in DMEM.

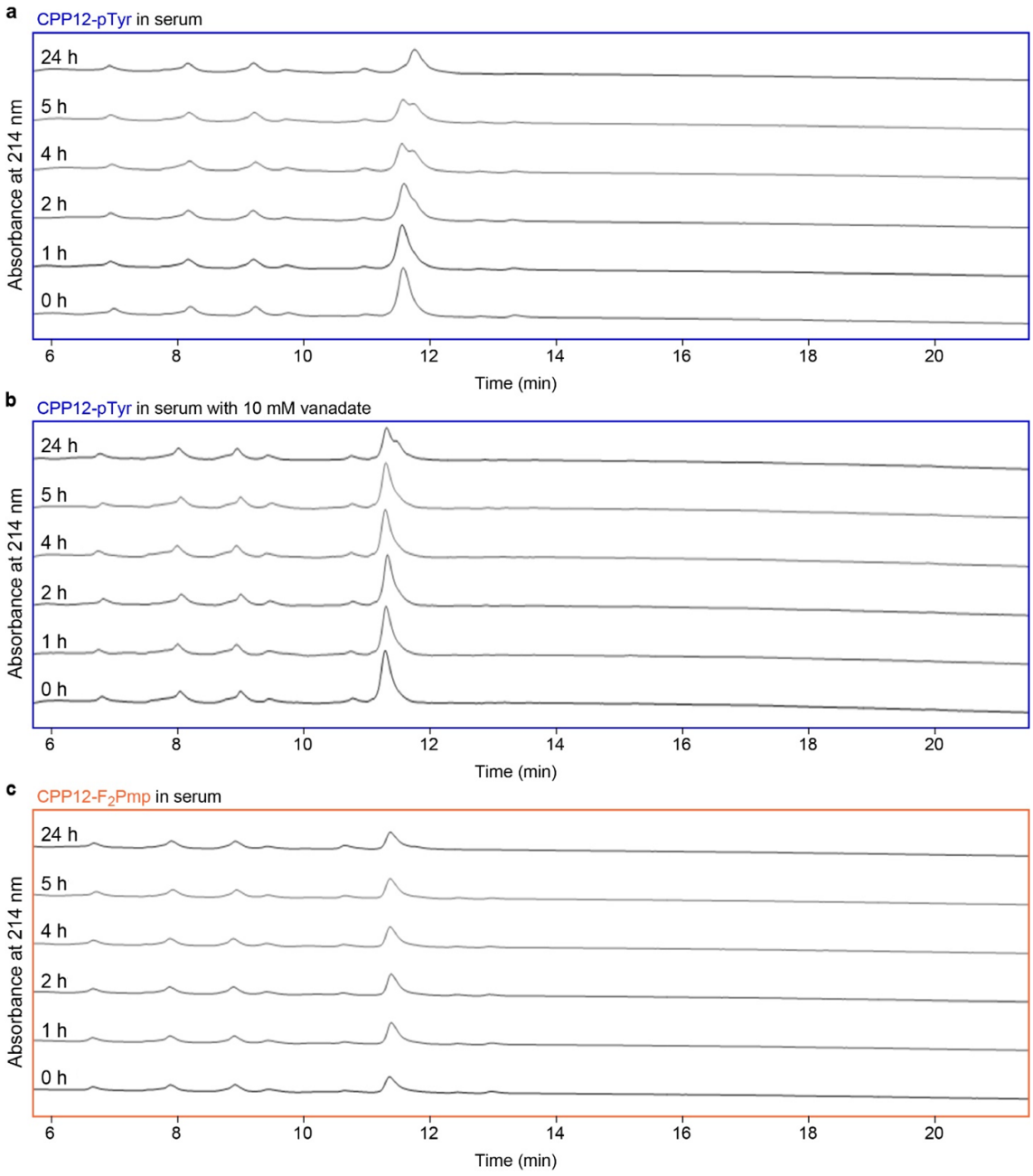

Figure 2.9. HPLC analysis of degradation in serum for selected CPP12-gp130 peptides.[127,137] HPLC traces at various time points for selected CPP12-gp130 peptides in 10% FBS in DMEM at 37 °C with and without 10 mM sodium orthovanadate. Areas under each peptide chromatogram peak were normalized to the area under the zero timepoint chromatogram peak (**Fig. 2.3b**).

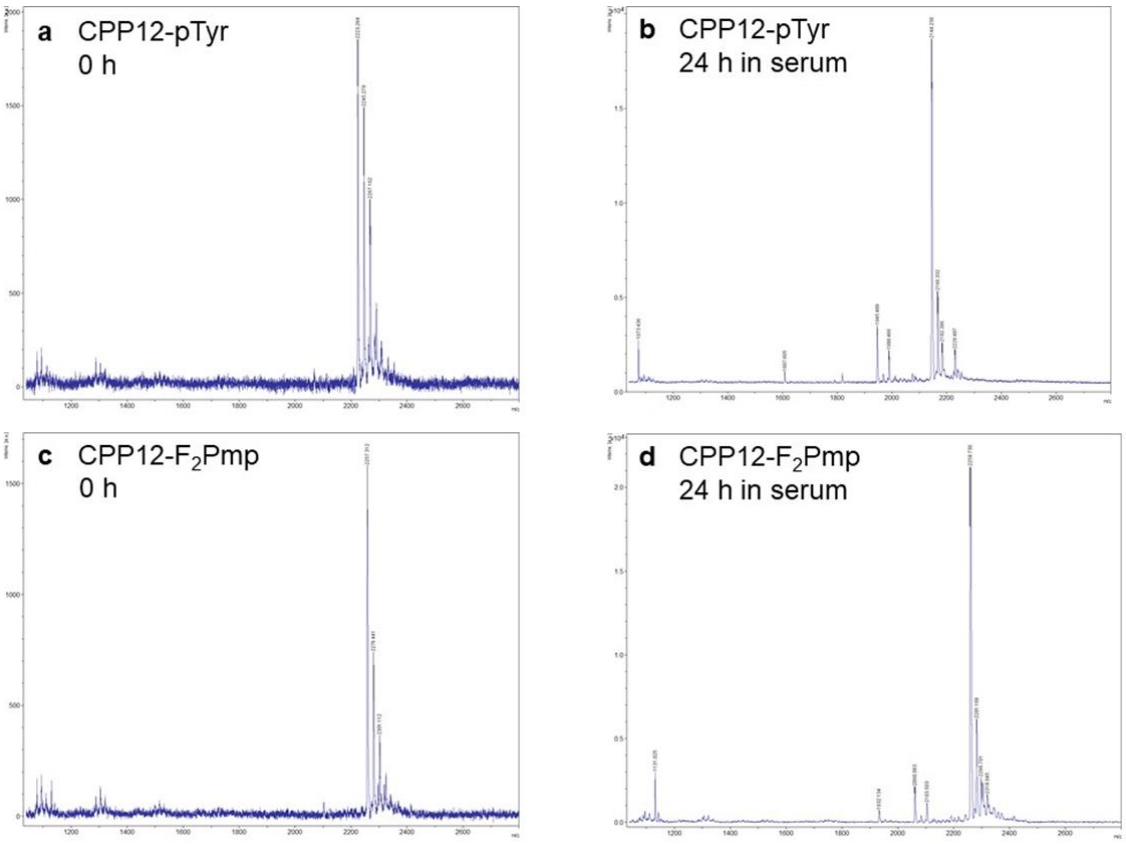

Figure 2.10. MALDI mass spectrometry traces for (a) CPP12-pTyr, (b) CPP12-pTyr after 24 h in serum, (c) CPP12-F_2Pmp, and (d) CPP12-F_2Pmp after 24 h in serum.

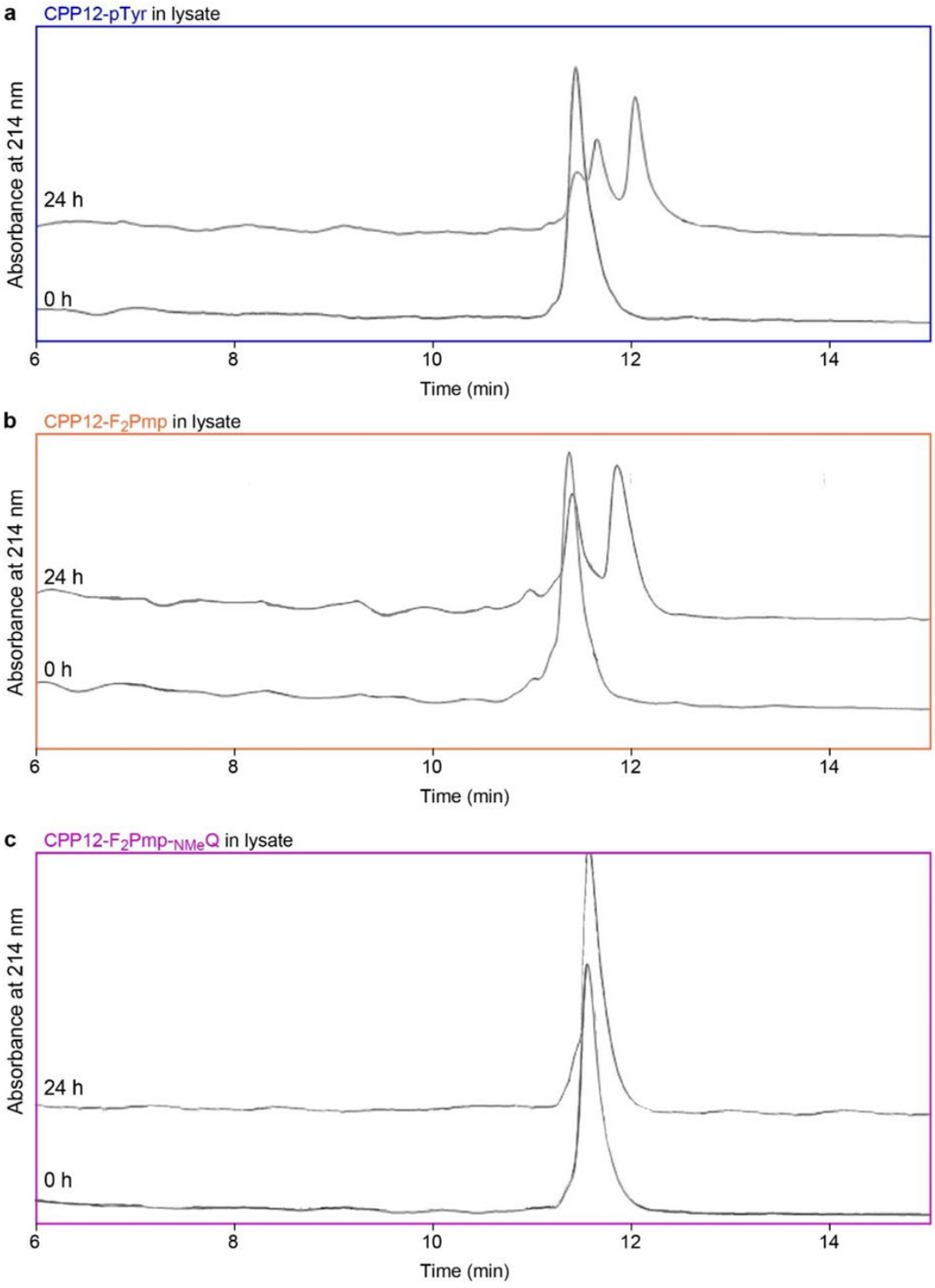

Figure 2.11. HPLC analysis of degradation in cell lysate for selected CPP12-gp130 peptides.[127,137] Overlays of HPLC traces at zero hour and 24 h timepoints for selected CPP12-gp130 peptides in HeLa cell lysate at 37 °C. Areas under each peptide chromatogram peak were normalized to the area under the zero timepoint chromatogram peak (**Fig. 2.3c**).

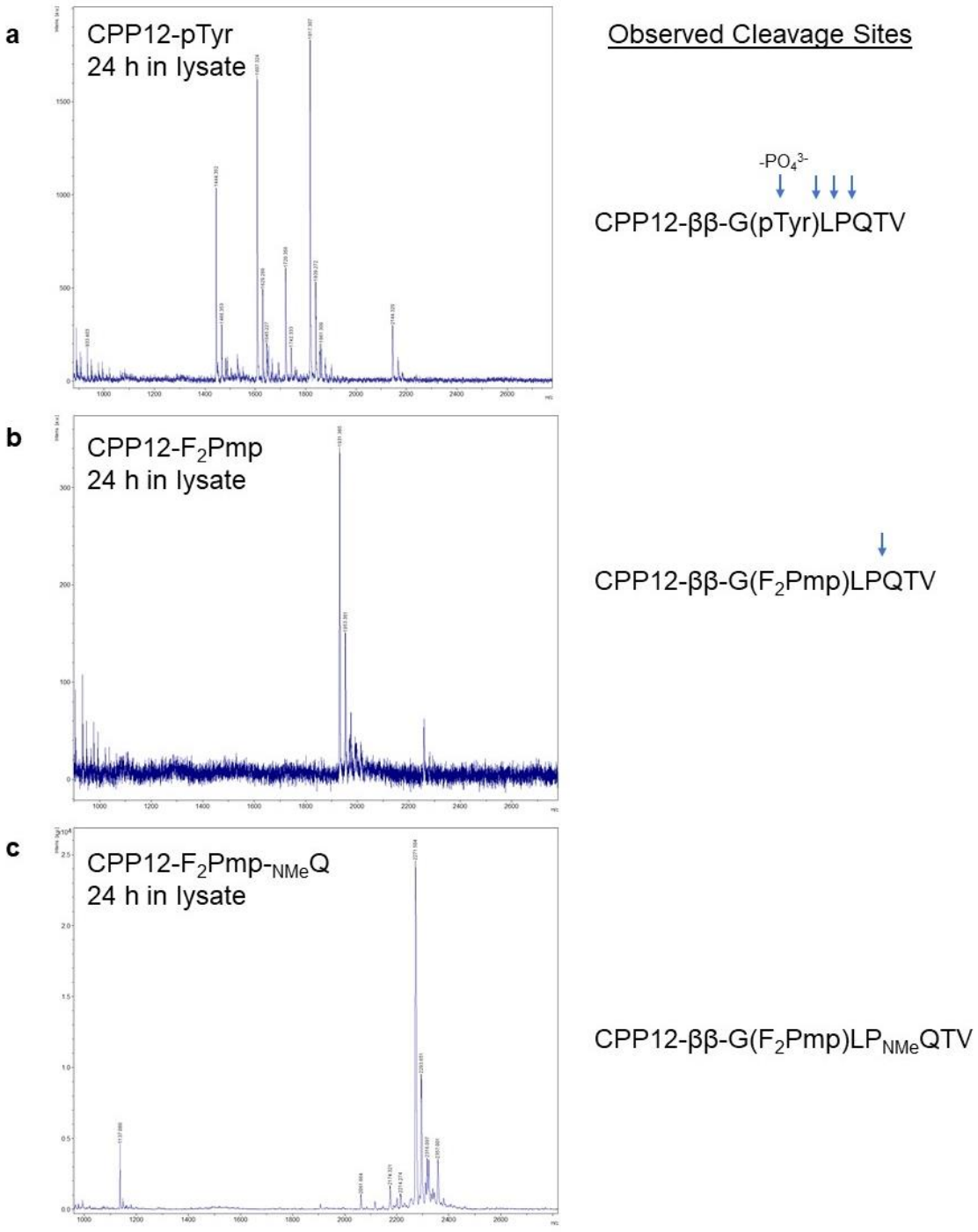

Figure 2.12. MALDI mass spectrometry traces for (a) CPP12-pTyr after 24 h in cell lysate, (b) CPP12-F_2Pmp after 24 h in cell lysate, and (c) CPP12-F_2Pmp-$_{NMe}$Q after 24 h in cell lysate.

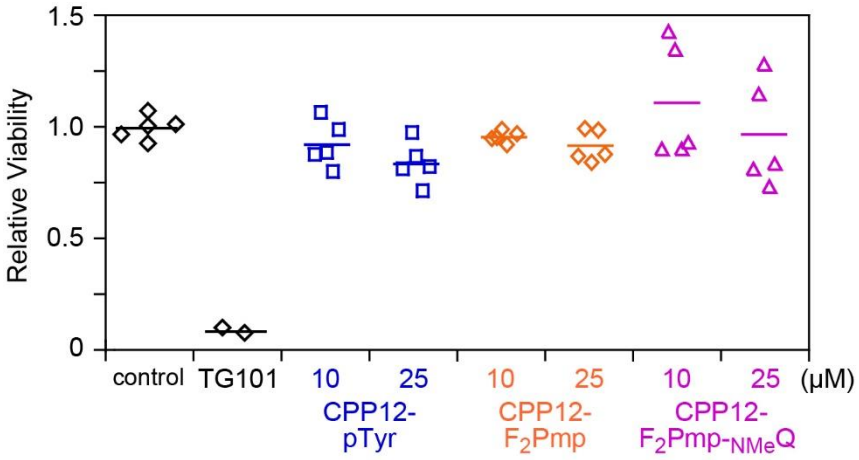

Figure 2.13. Viability of MDA-MB-468 cells after treatment with CPP12-pTyr, CPP12-F_2Pmp, and CPP12-F_2Pmp-$_{NMe}$Q peptides.[128] MDA-MB-468 breast cancer cells were seeded at 3 x 10^3 cells/well in white opaque 96-well plates overnight. Cells were treated with 10 or 25 μM of CPP12-gp130 peptides or vehicle and incubated at 37 °C for 72 hours. Cell viability was assessed using the CellTiter-Glo Luminescent Cell Viability kit (Promega). This experiment was performed with two biological replicates, one with two technical replicates and the other with three technical replicates (all five values displayed). Control Jak inhibitor, TG101, was run at 4.5 μM for one biological replicate with two technical replicates.

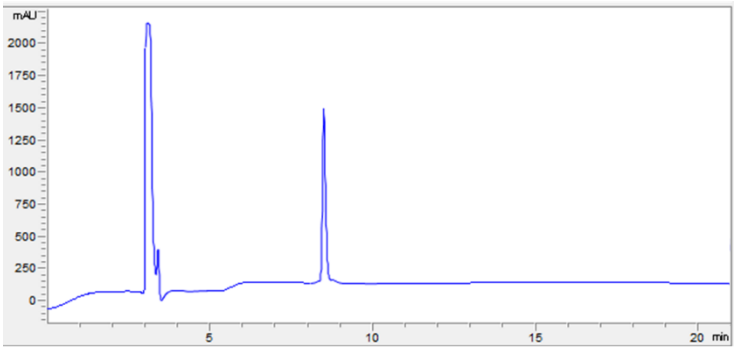

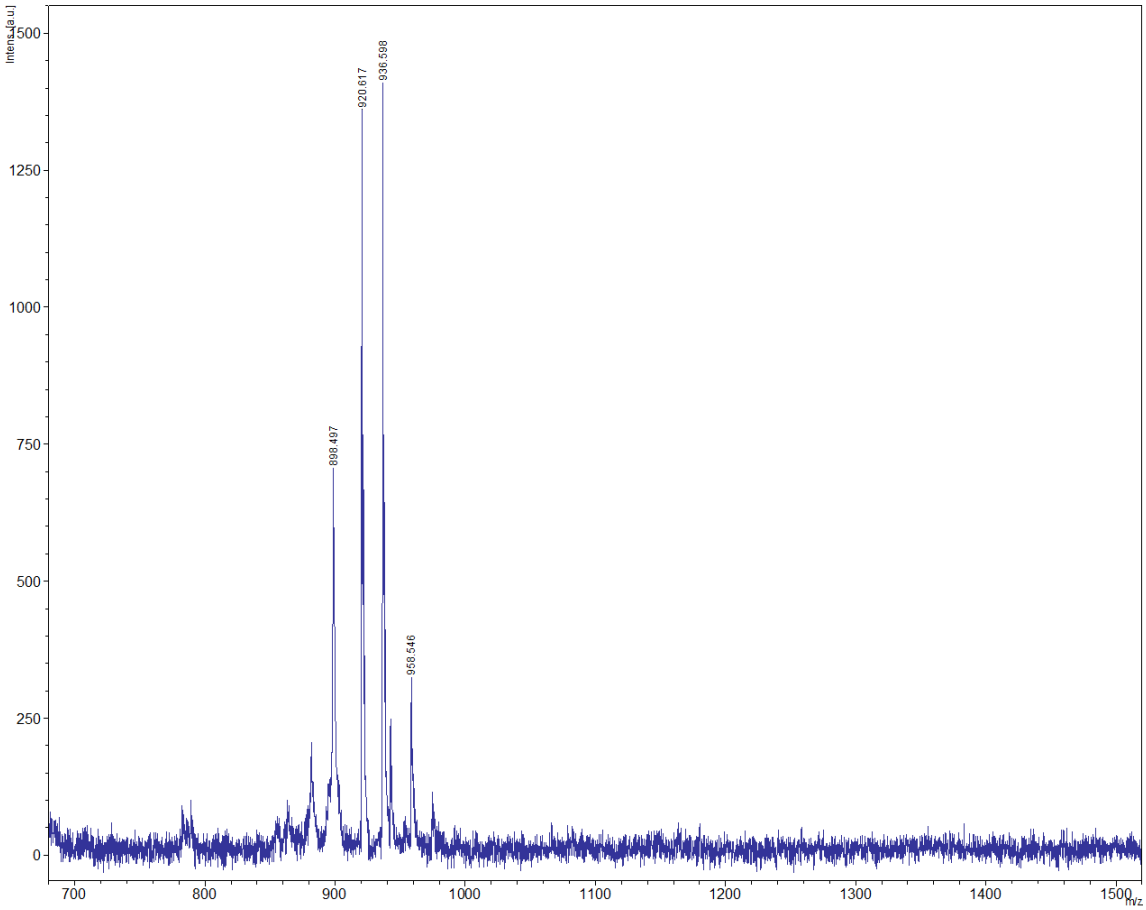

Figure 2.14. Analytical HPLC trace at 214 nm and MALDI-TOF mass spectrometry trace for peptide ac-pTyr.

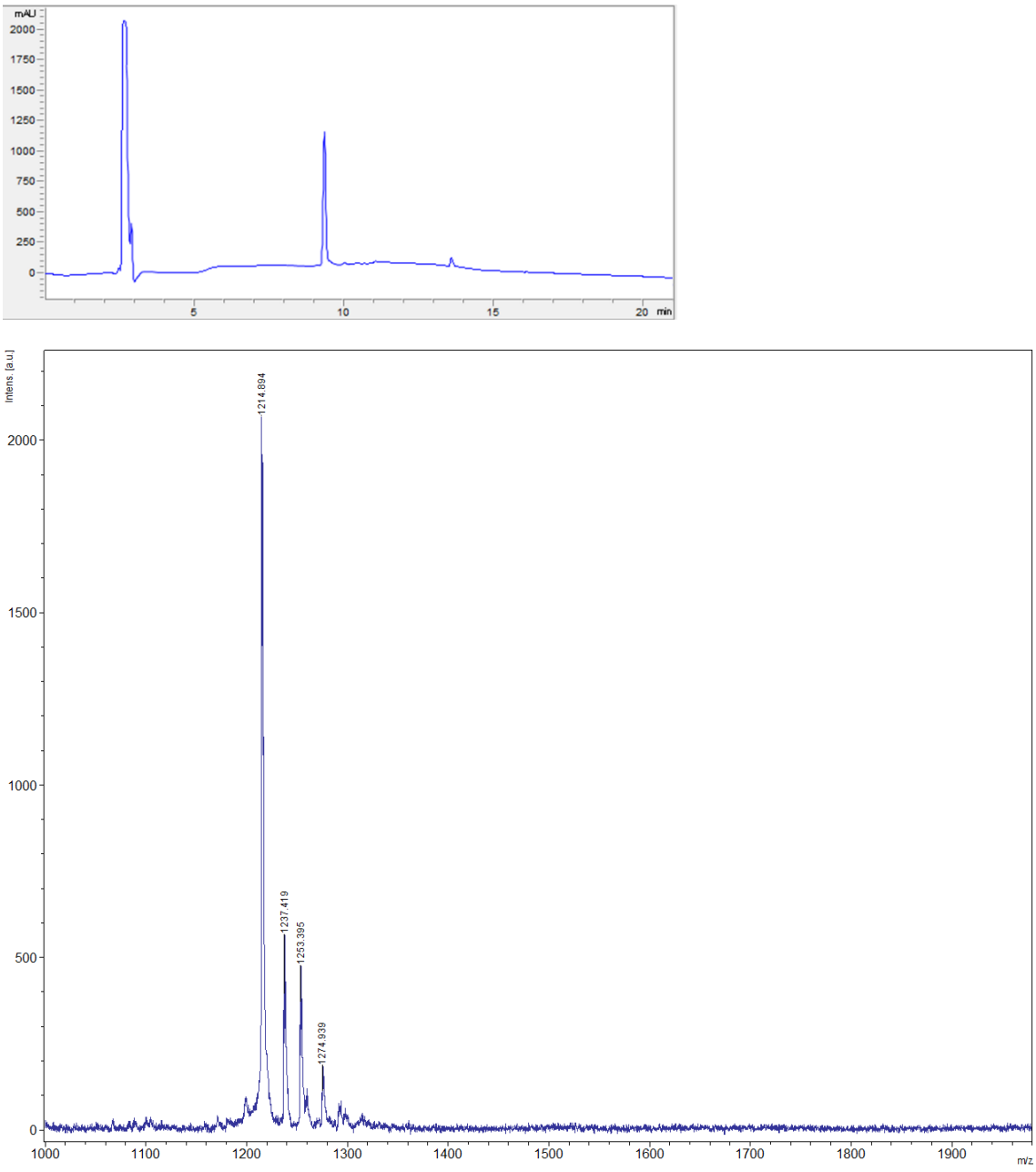

Figure 2.15. Analytical HPLC trace at 214 nm and MALDI-TOF mass spectrometry trace for peptide flu-pTyr.

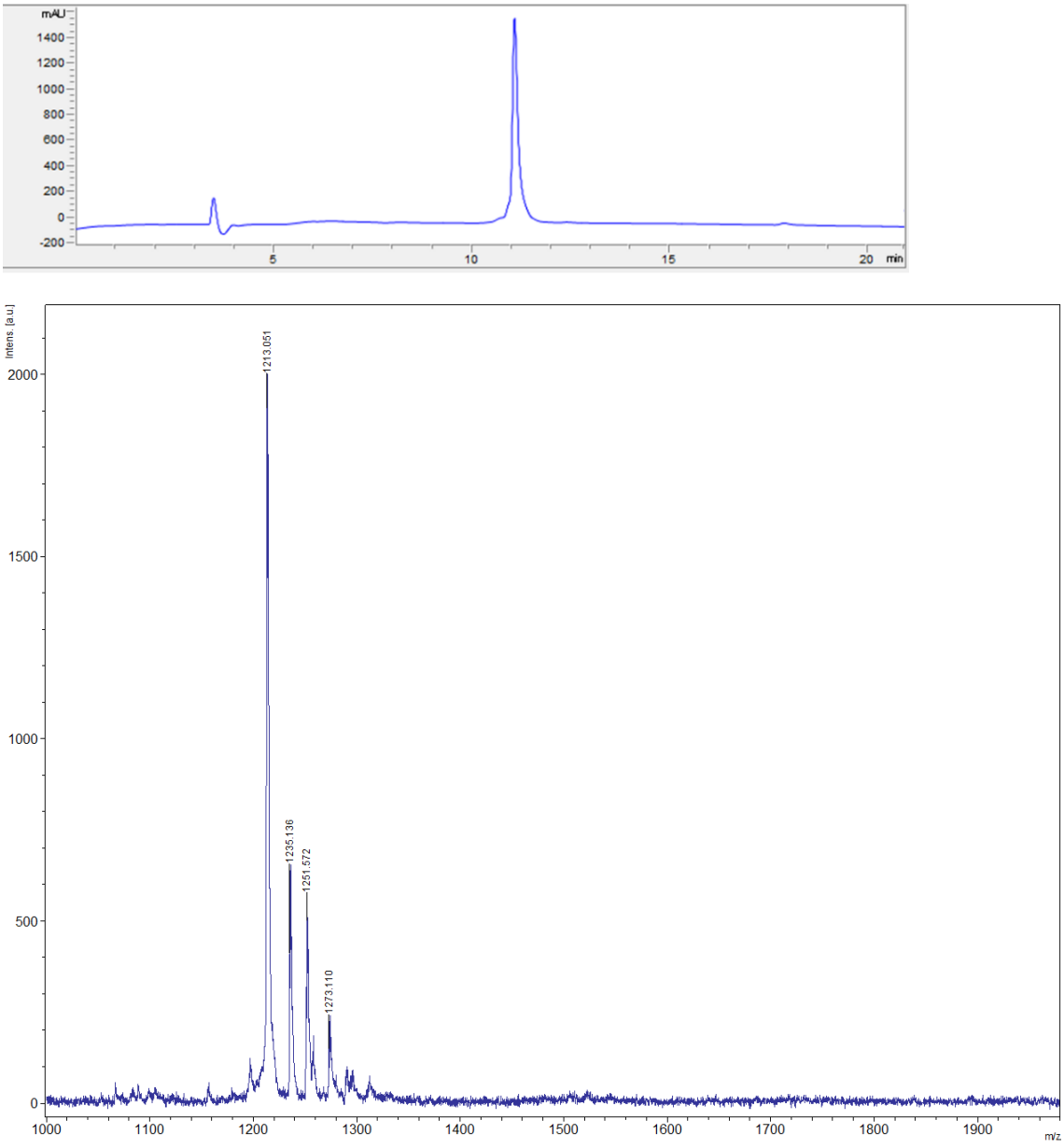

Figure 2.16. Analytical HPLC trace at 214 nm and MALDI-TOF mass spectrometry trace for peptide flu-Pmp.

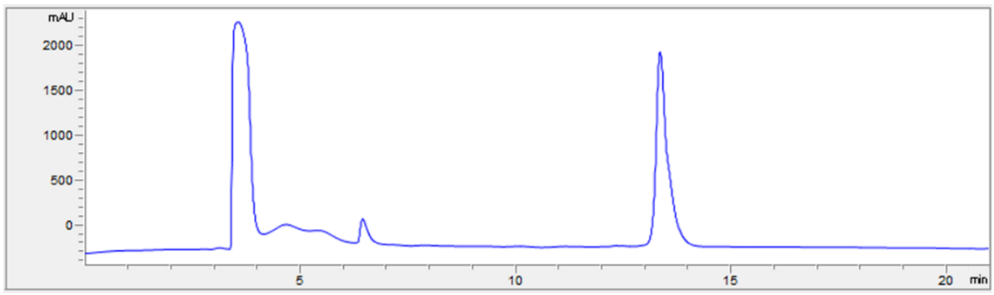

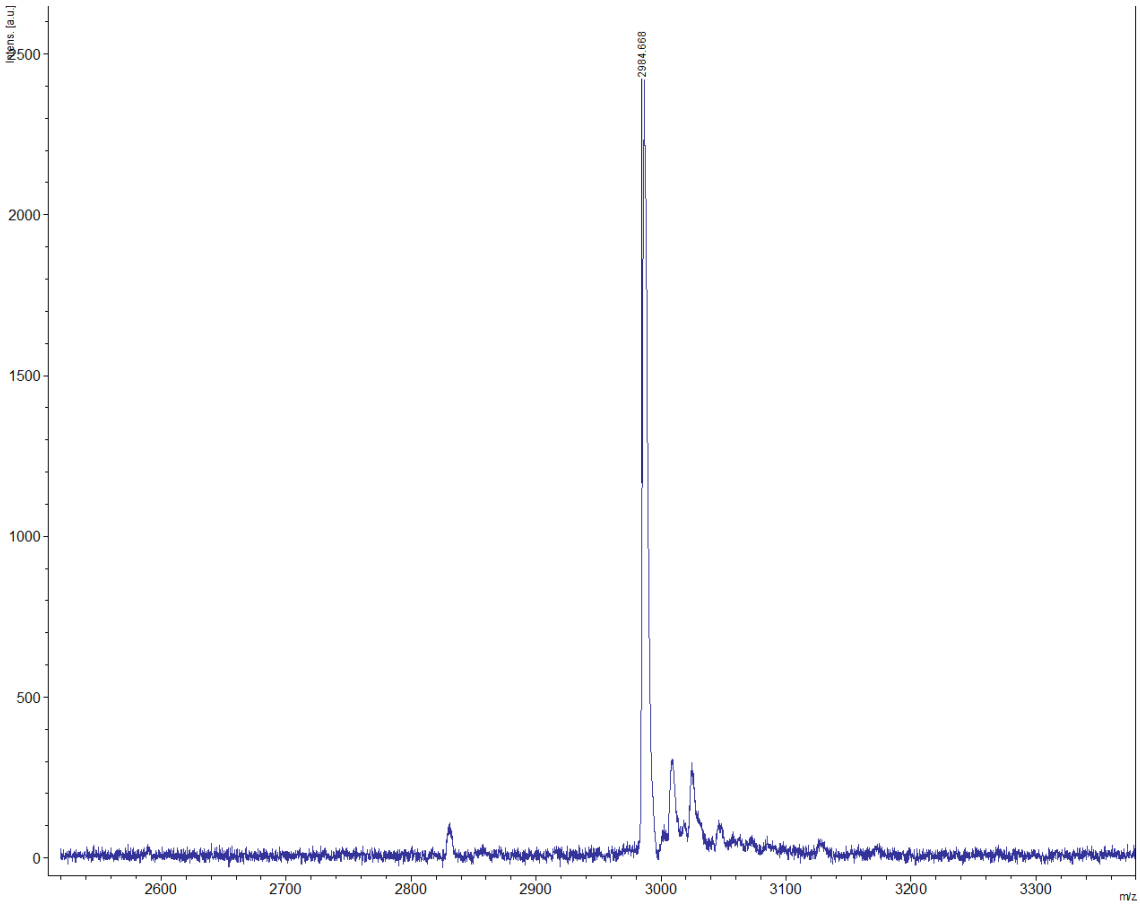

Figure 2.17. Analytical HPLC trace at 214 nm and MALDI-TOF mass spectrometry trace for peptide CPP12-Pmp-ct.

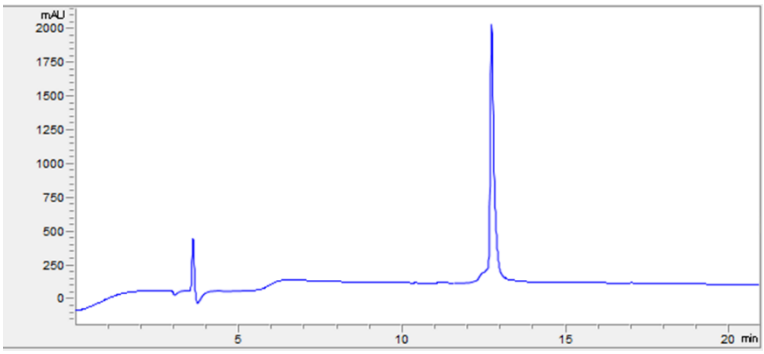

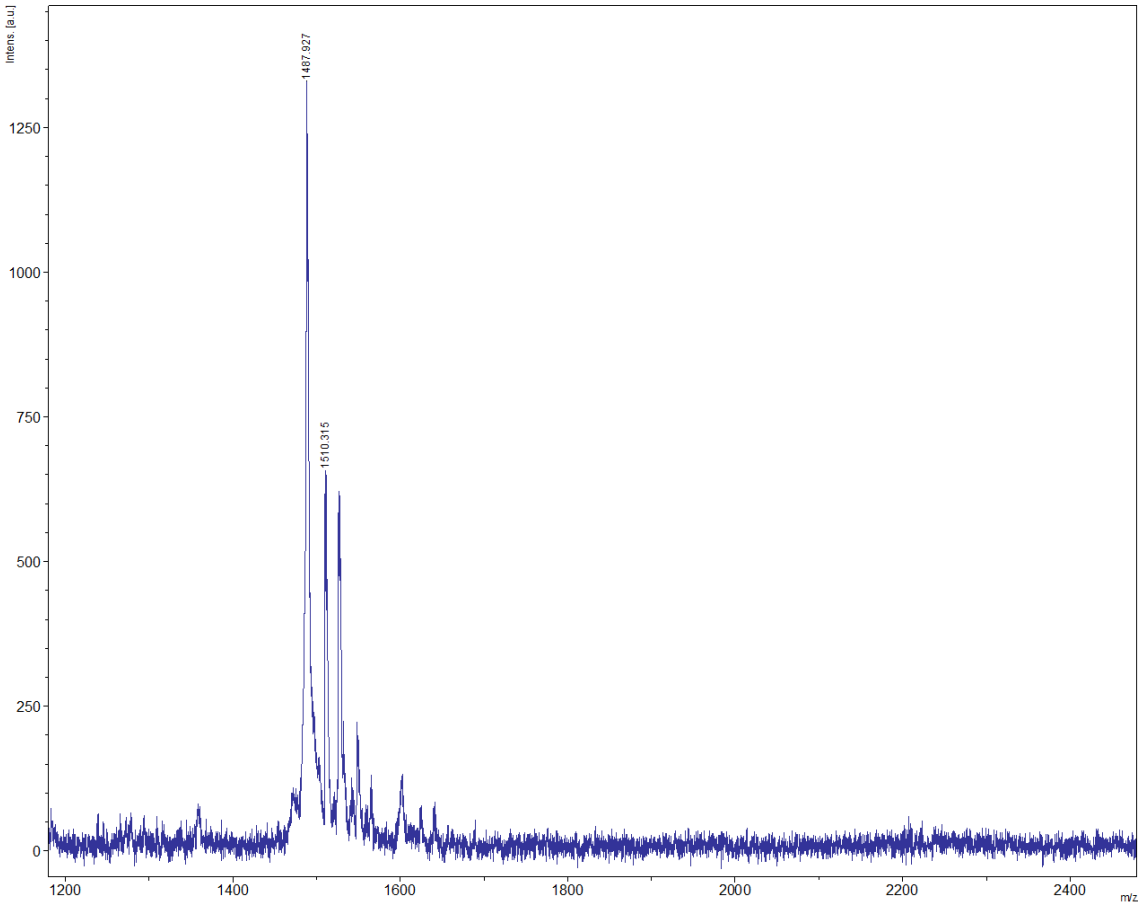

Figure 2.18. Analytical HPLC trace at 214 nm and MALDI-TOF mass spectrometry trace for peptide ct-Pmp.

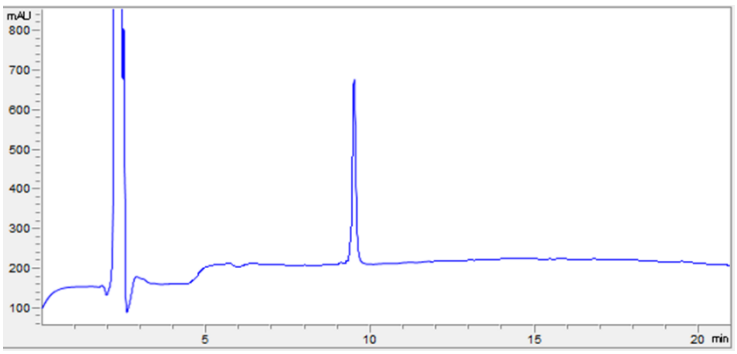

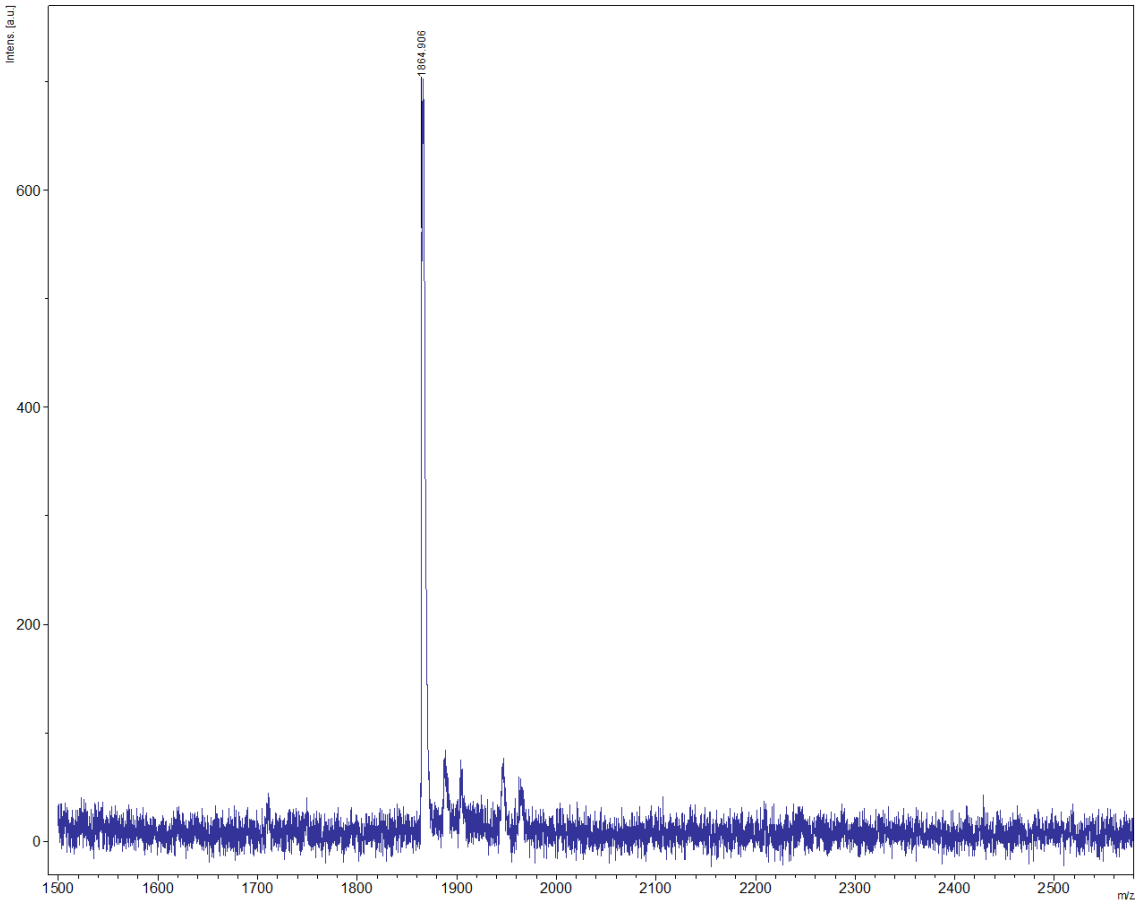

Figure 2.19. Analytical HPLC trace at 214 nm and MALDI-TOF mass spectrometry trace for peptide ct-TAT.

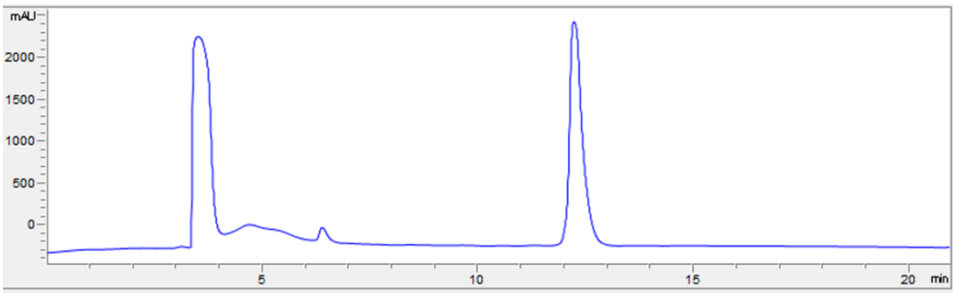

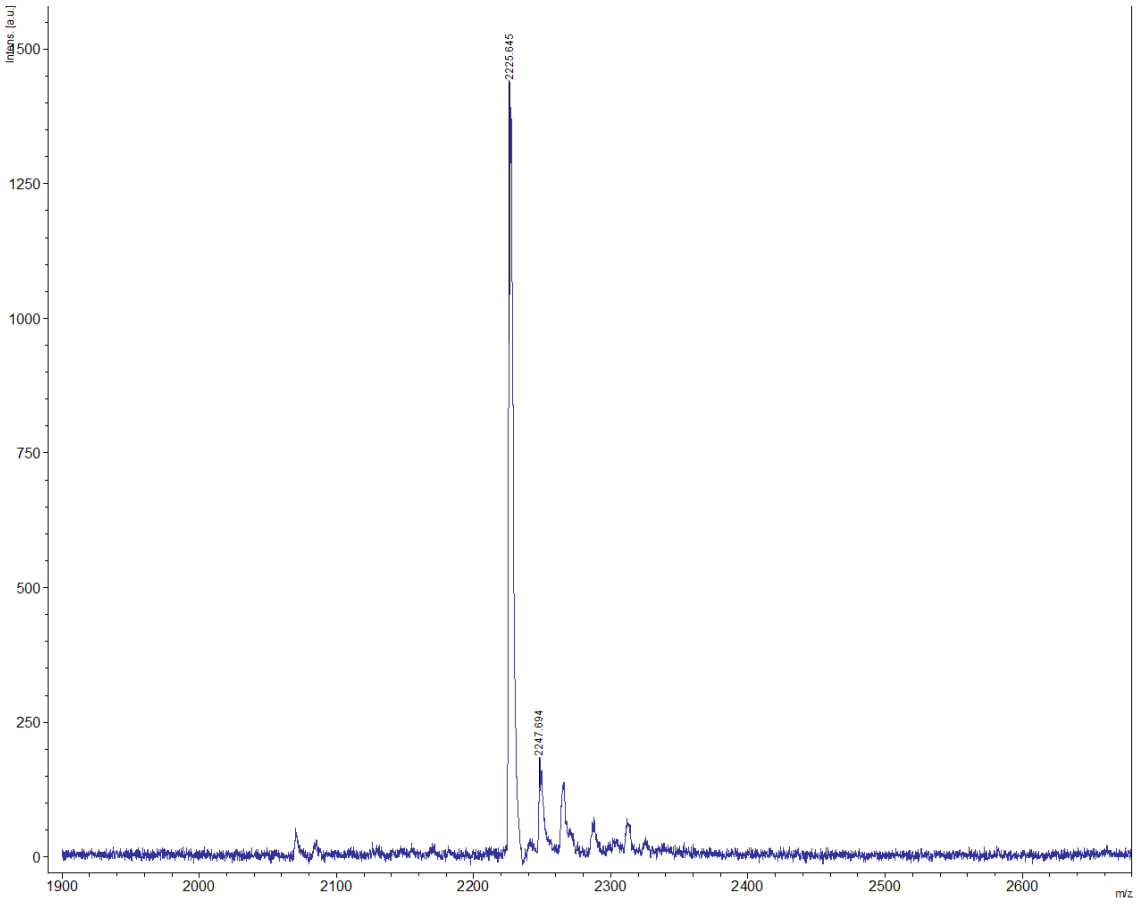

Figure 2.20. Analytical HPLC trace at 214 nm and MALDI-TOF mass spectrometry trace for peptide CPP12-pTyr.

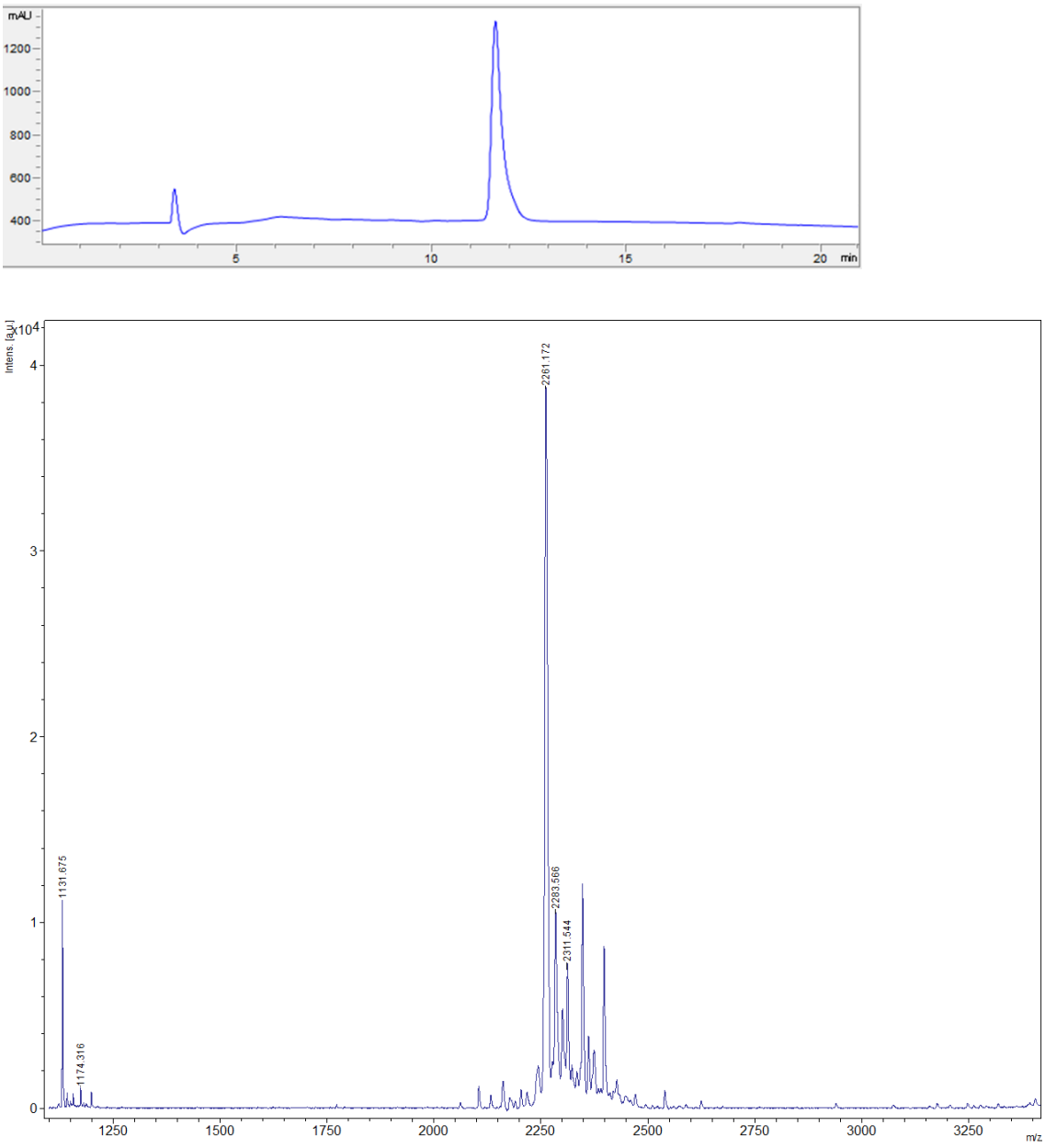

Figure 2.21. Analytical HPLC trace at 214 nm and MALDI-TOF mass spectrometry trace for peptide CPP12-F_2Pmp.

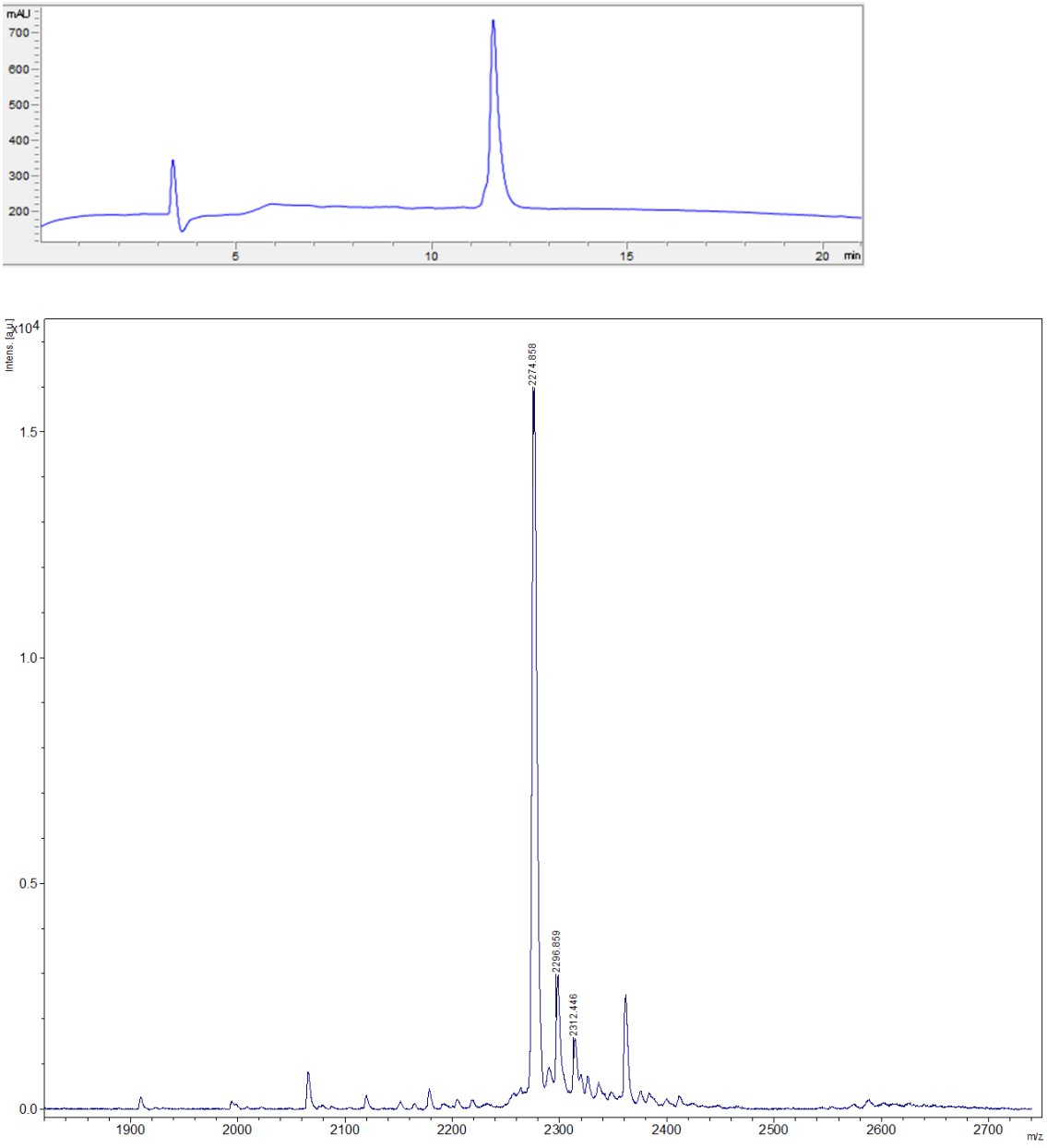

Figure 2.22. Analytical HPLC trace at 214 nm and MALDI-TOF mass spectrometry trace for peptide CPP12-F_2Pmp-$_{NMe}$Q.

*All figures and tables in this chapter were based off of my own experimental results and analysis except for Fig 1c, Fig 3a, Fig S4, Fig S5b-d, and Fig S10. Fig1c, Fig S4, and Fig S10 were performed in collaboration with Isidora Tosic and Kevin Jiang. Fig 3a and Fig S5b-d were performed in collaboration with Livia Shehaj and Jing Wang.

Chapter 3: Stapled Peptide Inhibitors of Autophagy Adapter LC3B[2]

[2] Cerulli, R.A., Shehaj, L., Brown, H., Pace, J., Mei, Y., Kritzer, J.A. Stapled peptide inhibitors of autophagy adapter protein LC3B. Submitted to *ChemBioChem*, 4/7/20.

3.1. Introduction

Autophagy is a highly conserved eukaryotic pathway for recycling proteins, organelles, and other cellular components.[77,78,138] Dysregulated autophagy is associated with many diseases including lysosomal storage diseases, neurodegenerative disorders, and cancers.[77–79,138–140] Inhibiting autophagy has been suggested as a potential cancer therapy, though the relationship between autophagy and cancer is complex. Some evidence suggests autophagy is protective against tumorigenesis, so autophagy inhibition may not be useful for preventing or treating early-stage cancers.[81,85,86] However, advanced malignancies depend on autophagy as a quality control mechanism, much like they depend on the ubiquitin-proteasome system.[79,140] In fact, autophagy inhibition has been shown to be effective both in solid tumors and in hematological malignancies.[87,88,90–93,141] A number of clinical trials have demonstrated improved overall survival when combining autophagy inhibition with standard-of-care chemotherapy and radiation in aggressive cancers, including glioblastoma multiforme and pancreatic adenocarcinoma.[94–96] Currently, the only autophagy inhibitors used in clinical studies have been the FDA-approved antimalarials chloroquine and hydroxychloroquine. However, their mechanism of action is thought to target lysosomal function, which is a relatively nonselective route to autophagy inhibition.[79,142] Inhibitors that are more selective for autophagy are sorely needed in order to better understand autophagy's role in advanced malignancies, and to develop more selective autophagy-inhibiting chemotherapies.

One strategy for developing selective autophagy inhibitors is to antagonize key protein-protein interactions. The Atg8 protein family mediates critical protein-protein interactions at several points in autophagic pathways, and thus represents an ideal target for selective inhibition (**Fig 3.1a**). In humans, Atg8 proteins are comprised of two protein

subclasses, LC3 (LC3A, LC3B, and LC3C) and GABARAP (GABARAP, GABARAPL1, and GABARAPL2). In this work, we focus on LC3B since it is the most-studied human Atg8 protein, and one with clear connections to cancer. For instance, Mikhaylova and colleagues demonstrated in clear cell renal carcinoma that LC3B expression correlated with higher tumor grade, and LC3B was a direct target for miR-204, a microRNA frequently upregulated in VHL-mutated clear cell renal carcinomas.[110] At the same time, several studies have demonstrated that other Atg8 proteins like GABARAP can function as tumor suppressors.[111,112] Therefore, being able to inhibit LC3B selectively over GABARAP would allow a direct pharmacological method for investigating these proteins' roles in autophagy and in cancer.

LC3B directly interacts with numerous autophagy cargo receptors, initiation complexes, processing enzymes, adapters, and trafficking proteins. Its many binding partners all use a conserved "LC3-interacting region" (LIR) motif to bind LC3 (**Fig 3.1a**).[101,103–109] We hypothesized that LIR motif peptides could be used as starting points to develop selective inhibitors of LC3B. Specifically, we started with a LIR motif peptide derived from the microtubule-associated vesicle transport protein FYCO1.[108,117] The LIR motif within FYCO1 is among the higher-affinity LIR motifs reported to date, and it is the most selective for LC3 proteins over GABARAPs. [104,116–118] Here we report detailed structure-activity relationships of the FYCO1 LIR motif with LC3B. We also applied artificial side chains to improve binding to key hydrophobic pockets. Finally, we designed stapled peptides which maintain selectivity for LC3B but improve affinity and biological stability. Notably, most peptide stapling strategies are limited to helical motifs. Because LIR motifs bind LC3B in an extended conformation, we applied an innovative diversity-oriented stapling strategy that does not assume any specific secondary structure.[132,136,143–149]

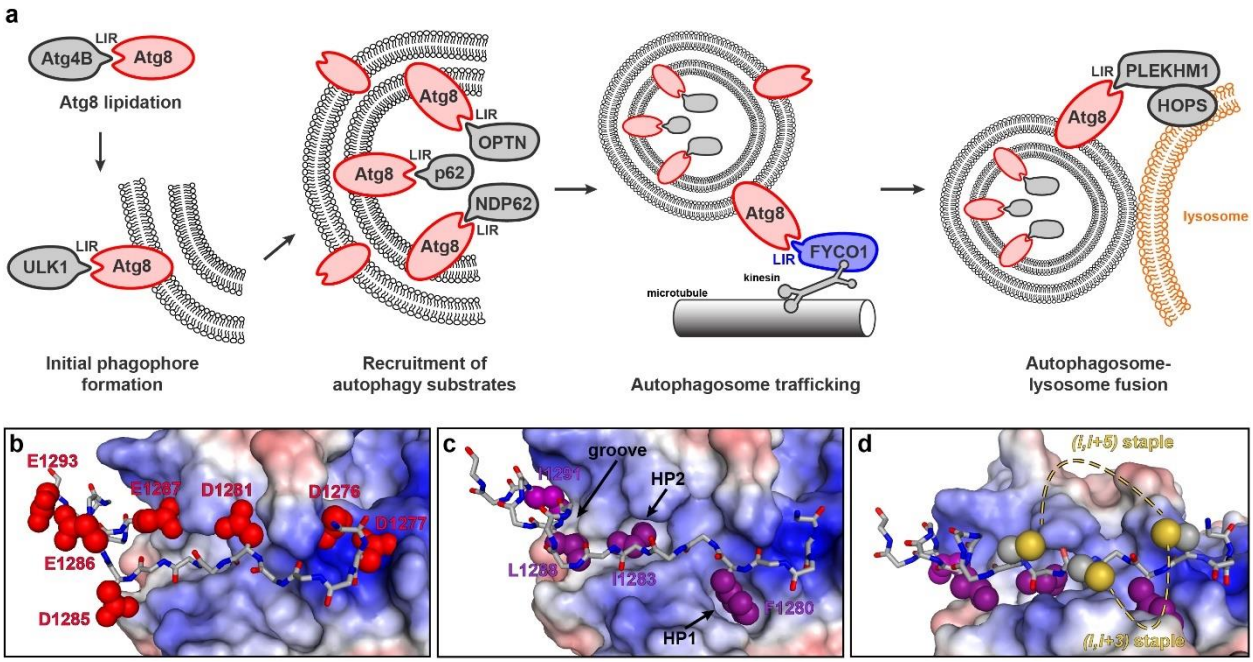

Figure 3.1. Protein-protein interactions of Atg8 proteins involving the LC3-interacting region (LIR) motif. a) LIR-dependent protein-protein interactions are involved in several stages of autophagy, including phosphatidylethanolamine conjugation to Atg8 proteins[105], ULK1 initiation complex tethering and early phagophore formation[103,104], selective cargo recruitment including mitophagy adapters[106] and ubiquitinylated aggregate adapter p62[107], autophagosome transport[108], and autophagosome-lysosome fusion.[101,109] b-d) Crystal structure of a LIR motif-containing peptide from FYCO1 bound to LC3B (PDB: 5CX3).[118] These images highlight key positions investigated in this study, including hydrophobic pockets (b), charged residues (c), and positions in close proximity suitable for stapling (d).

3.2. Results

Many interactions between LC3B and various LIR motif-containing proteins have been validated, but only a handful of studies have quantitatively measured binding affinities of LIR peptides for LC3B.[104,115–118] To compare directly to prior work, we explored two different binding assays for measuring binding of synthetic peptides to recombinant LC3B and recombinant GABARAP. One assay used fluorescence polarization and the other used biolayer interferometry (BLI). As controls for these assays, we prepared analogs of two previously reported LIR peptides, FYCO1 (residues D1276 through

E1293), which is selective for LC3B over GABARAP, and K1, which is selective for GABARAP over LC3B.[117,150] In fluorescence polarization assays, we measured a K_d value of 50 nM for fluorescein-labeled FYCO1 peptide (flu-FYCO1) binding to LC3B, and no appreciable binding of flu-FYCO1 to GABARAP at concentrations as high as 4 μM (**Fig 3.2a-b**, Fig 3.4,3.5). As a positive control for GABARAP binding, we prepared fluorescein-labeled K1 peptide (flu-K1) and measured K_d values of 40 nM for flu-K1 binding GABARAP, and 1.2 μM for flu-K1 binding to LC3B. (**Fig 3.2a-b**, Fig 3.5). These data are roughly consistent with prior work with the FYCO1 and K1 peptides.[117,118,150]

While these assays were comparable to prior fluorescence polarization assays performed with similar dye-labeled peptides, we sought a more efficient and convenient method for measuring the binding of LC3B and GABARAP with synthetic peptides. We found that biolayer interferometry (BLI) allowed for rapid, reproducible results for protein-peptide binding using biotinylated peptides immobilized on BLI biosensors. In BLI assays with biotinylated FYCO1 peptide (FYCO1), we measured K_d values of 290 nM for LC3B, and 1.4 μM for GABARAP (**Fig. 3.2c-d**). In BLI assays with biotinylated K1 peptide (K1), we measured K_d values of 19 μM for LC3B and 390 nM for GABARAP (Fig. 3.6). Overall, these data more closely match prior work with the FYCO1 and K1 peptides than the data from the fluorescence polarization assay. Thus, we proceeded to use BLI with biotinylated peptides to measure the LC3B and GABARAP binding affinities of FYCO1 peptides and their analogs.

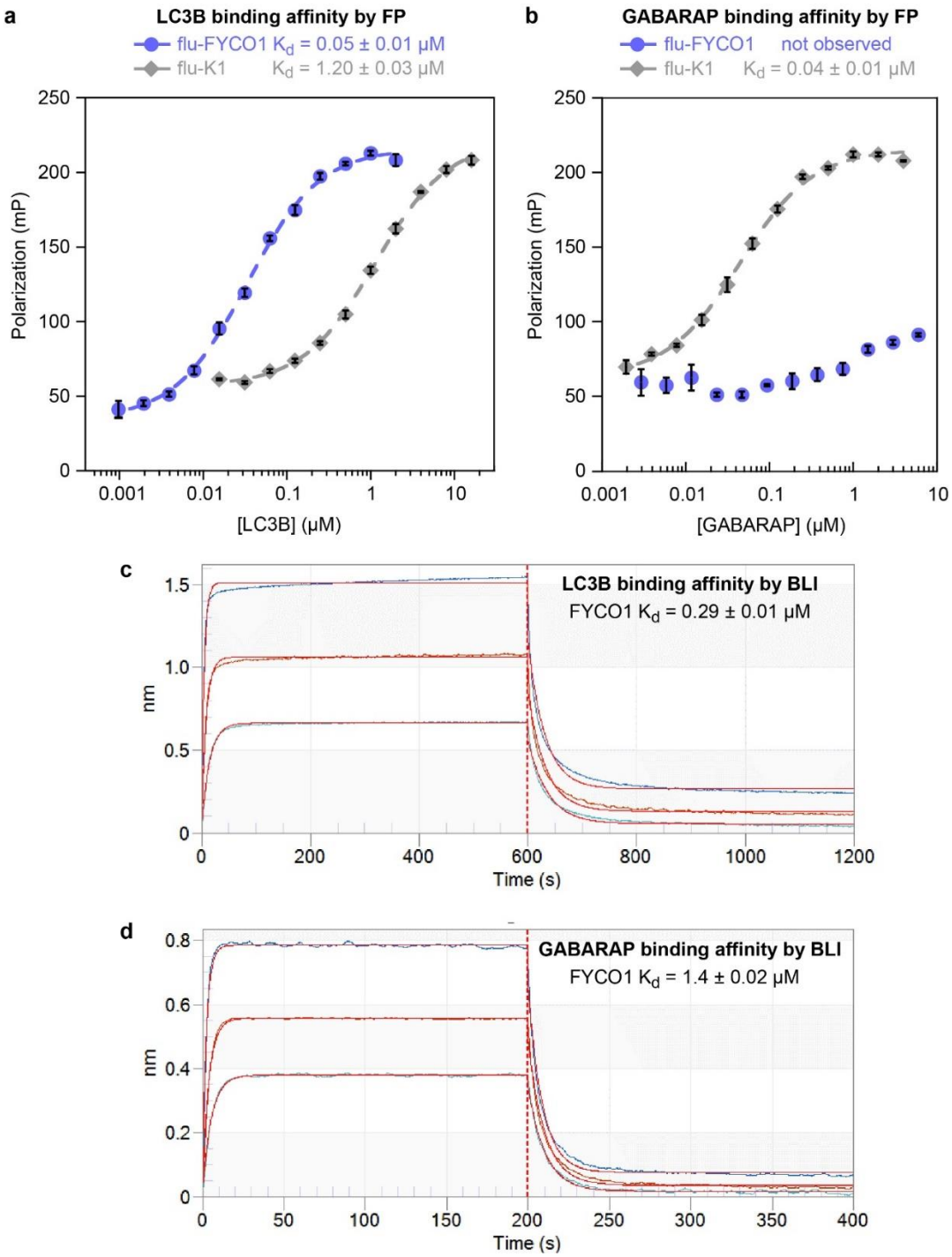

Figure 3.2. Binding affinities of FYCO1 and K1 peptides with the human Atg8 proteins LC3B and GABARAP. a,b) Fluorescence polarization binding assays for fluorescein-labeled FYCO1 peptide (flu-FYCO1) with recombinant human GABARAP and LC3B proteins. Peptide K1, a previously described GABARAP-selective peptide, is used as a positive control. Curve fitting was performed using KaleidaGraph graphing software as described.[136] Average K_d values and standard error were calculated from the individual curve fits of three independent replicates, each with three technical replicates (individual

replicates with raw polarization values shown in Fig 3.4,3.5). c,d) Biolayer interferometry data (BLI) for biotinylated FYCO1 peptide (FYCO1) with recombinant human GABARAP and LC3B. BLI was performed with 0.5 μg/mL of biotinylated peptides loaded onto streptavidin-coated biosensors with serial dilutions of protein at 30 °C. Association and dissociation steps were measured for 200 seconds each. Curve fitting was performed using the Octet DataAnalysis software (Forté Bio) and K_d values were calculated as described in Methods. Shown are primary data (dark blue, orange and light blue traces) and curve fits (red curves) for incubation with 1.5, 0.75, and 0.375 μM for LC3, and 4, 2, and 1 μM for GABARAP. Average K_d values and standard errors of the mean (Tables 3.1 and 3.2) were calculated from the individual curve fits of three independent replicates (Tables 3.5-3.10).

The FYCO1 peptide consists of residues 1276 through 1293 of the human FYCO1 protein, with a C-terminal tryptophan included to allow more accurate spectrophotometric concentration determination; the core LIR motif within FYCO1 is residues F1280 through I1283.[117] First, we assessed the importance of residues outside the core LIR motif. Truncating the four N-terminal residues (peptide Δ1276-1279) completely abrogated binding, implying an important role for these residues (**Table 3.1**). By contrast, truncating the five C-terminal residues (peptide Δ1289-1293) led to a 10-fold loss in binding affinity (K_d of 3.1 μM compared to 0.29 μM for the full-length FYCO1 peptide). Truncating only two C-terminal residues (peptide Δ1292-1293) led to a 1.6-fold loss in binding affinity (K_d of 0.46 μM), implying an important role for residues 1289-1291. These results are consistent with the binding mode observed in the crystal structure of the FYCO1 peptide bound to LC3B, in which I1291 makes hydrophobic contacts in a shallow groove of LC3B, while Q1292 and E1293 face solvent (**Fig 3.1c**).

In general, LIR motifs that bind LC3B often have multiple negatively charged residues within and surrounding the core LIR motif.[113] It is unclear from the literature whether these negative charges contribute substantially to the binding affinity. Thus, we next measured the individual contributions of each of the seven negatively charged residues

Name	Sequence	K_d (μM)	Std Err (μM)
FYCO1	DDAVFDIITDEELCQIQEW	0.29	0.01
Termini Truncations			
Δ1276-1279	FDIITDEELCQIQEW	ND	ND
Δ1289-1293	DDAVFDIITDEELW	3.1	0.6
Δ1292-1293	DDAVFDIITDEELCQIW	0.46	0.03
Gln/Asn Scan of Negative Residues			
D1276N	**N**DAVFDIITDEELCQIQEW	0.35	0.02
D1277N	D**N**AVFDIITDEELCQIQEW	0.48	0.04
D1281N	DDAVF**N**IITDEELCQIQEW	1.1	0.2
D1285N	DDAVFDIIT**N**EELCQIQEW	0.41	0.02
E1286Q	DDAVFDIITD**Q**ELCQIQEW	0.76	0.07
E1287Q	DDAVFDIITDE**Q**LCQIQEW	2.7	0.4
E1293Q	DDAVFDIITDEELCQIQ**Q**W	0.30	0.005
D1276N/D1277N	**NN**AVFDIITDEELCQIQEW	1.2	0.03
Hydrophobic Mutations			
F1280Nap2	DDAV**2**DIITDEELCQIQEW	0.14	0.02
F1280Nap1	DDAV**1**DIITDEELCQIQEW	0.17	0.01
I1283F	DDAVFDI**F**TDEELCQIQEW	5.9	0.2
I1283Nap2	DDAVFDI**2**TDEELCQIQEW	2.6	0.1
L1288NL5	DDAVFDIITDEE**ν**CQIQEW	0.58	0.04
L1288tbA	DDAVFDIITDEE**α**CQIQEW	0.25	0.01
I1291tbA	DDAVFDIITDEELCQ**α**QEW	0.44	0.03
I1291F	DDAVFDIITDEELCQ**F**QEW	0.73	0.03
Introduction of Positive Charge			
A1278r	DD**r**VFDIITDEELCQIQEW	0.90	0.06
R-FYCO1	**R**DDAVFDIITDEELCQIQEW	0.20	0.01
RR-FYCO1	**RR**DDAVFDIITDEELCQIQEW	0.33	0.01
Optimized Combination			
Comb1	**R**DDAV**2**DIITDEE**α**CQIQEW	0.12	0.004

Table 3.1. Binding affinities for FYCO1-derived peptides with LC3B protein. BLI and curve fitting were performed as described in Figure 3.2 and in Methods. Average K_d values and standard errors of the mean (Tables 3.1 and 3.2) were calculated from the individual curve fits of three independent replicates (Tables 3.5-3.7). **2** denotes 2-naphthylalanine, **1** denotes 1-naphthylalanine, **ν** denotes 5,5-dimethylnorleucine, **α** denotes *tert*-butylalanine, and **r** denotes D-arginine. All peptides have a C-terminal amide group and an N-terminal biotin separated from the peptide by two beta-alanine residues. ND denotes no binding affinity detected up to 20 μM LC3B protein.

in the FYCO1 peptide (**Fig. 3.1b**). We prepared a panel of analogs that represented individual substitutions of asparagine in place of aspartate, or glutamine in place of glutamate (**Table 3.1**). While we found that an N-terminal truncation completely abrogated binding (peptide Δ1276-1279), peptides D1276N and D1277N each had well under 2-fold reduced affinity, with K_d values of 0.35 and 0.48 μM, respectively (**Table 3.1**). Following up on these results, we prepared and tested a double mutant, D1276N/D1277N. D1276N/D1277N had a K_d of 1.2 μM, which is poorer than a simple combination of the effects of the individual substitutions. These data suggest that hydrogen bonding or other non-electrostatic interactions at the N-terminus contribute to LC3B binding, and also that the charged N-terminus contributes to the binding interaction in a cooperative manner.

Most of the other negatively charged residues appear to contribute very little to the binding affinity of the FYCO1 peptide, including D1276, D1277, D1285, and E1293 (**Table 3.1**). The most important negatively charged residue was E1287, as peptide E1287Q had a 9.3- fold loss in binding affinity relative to FYCO1. D1281N and E1286Q peptides had a moderate loss in affinity, 3.8-fold and 2.6- fold less than FYCO1, respectively.

After demonstrating the relative contributions of the terminal residues and negative charges, we next investigated the hydrophobic residues. The FYCO1 peptide binds LC3B in an extended conformation, with F1280 and I1283 binding separate, conserved hydrophobic pockets on LC3B (HP1 and HP2, **Fig 3.1c**).[118] Based on the crystal structure, we observed that HP1 (the binding pocket for F1280) may be able to accommodate a larger hydrophobic side chain, so we prepared analogs with either 1-naphthylalanine or 2-naphthylalanine in this position (F1280Nap1 and F1280Nap2). Both substitutions improved binding, each by roughly 2-fold (**Table 3.1**). The crystal structure

also suggested that HP2 (the binding pocket for I1283) might accommodate larger side chains, but substituting I1283 with either a phenylalanine or a 2-naphthylalanine resulted in ligands with poorer LC3B affinity (20- and 9-fold losses in affinity, respectively). These data support that HP1 of LC3B, but not HP2, is amenable to binding larger side chains.

In the crystal structure, L1288 and I1291 of FYCO1 bind a shallow hydrophobic groove adjacent to HP2 (**Fig 3.1c**). In each of these positions, we explored several side chains that might enhance hydrophobic interactions. Substituting I1291 with a *tert*-butylalanine or phenylalanine resulted in 1.5-fold or 2.5-fold poorer affinity, respectively. Substituting L1288 with the larger aliphatic residue 5,5-dimethyl-norleucine led to a 2-fold loss in affinity, but substituting L1288 with a *tert*-butylalanine (peptide L1288tbA) resulted in a very slight improvement in affinity (K_d value of 0.25 μM). These data suggest that the shallow groove may only accommodate moderately-sized aliphatic residues, but that exploration of artificial aliphatic side chains could lead to further improvements in affinity.

Another feature of the crystal structure is the close proximity to the binding site of several negatively charged LC3B residues. Specifically, the N-terminus of the bound FYCO1 peptide is positioned near LC3B residues D48, E18 and D19. Thus, we sought to introduce new electrostatic interactions through the incorporation of one or two arginine residues near the N-terminus of FYCO1. Substitution of solvent-oriented A1278 with D-arginine, which was selected to position the side chain near LC3B residues E18 and D19, produced a peptide with 3-fold poorer binding affinity (**Table 3.1**). Interestingly, addition of one arginine to the N-terminus of the FYCO1 peptide improved binding affinity (peptide R-FYCO1, with a K_d value of 0.2 μM), but incorporation of two arginines demonstrated no benefit (peptide RR-FYCO1, with a K_d value of 0.33 μM).

To this point, three individual substitutions had resulted in a gain in affinity (F1280Nap2, L1288tbA, and R-FYCO1; see **Table 3.1**). Combining these substitutions, we prepared

and tested peptide Comb1 and measured a K_d for LC3B of 0.12 μM, representing a 2.4-fold improvement over the parent peptide.

Name	Sequence	K_d (μM)	Std Err (μM)
FYCO1	DDAVFDIITDEELCQIQEW	0.29	0.01
C1289S	DDAVFDIITDEEL**S**QIQEW	0.33	0.03
***(i,i+3)* Conformational Constraint**			
C1282-o	DDA**C**FD**C**ITDEEL**S**QIQEW (*ortho*)	ND	ND
C1282-m	DDA**C**FD**C**ITDEEL**S**QIQEW (*meta*)	8.3	0.7
C1282-p	DDA**C**FD**C**ITDEEL**S**QIQEW (*para*)	10.5	1.7
***(i,i+5)* Conformational Constraint**			
C1284-m	DDA**C**FDII**C**DEEL**S**QIQEW (*meta*)	6.3	0.3
C1284-p	DDA**C**FDII**C**DEEL**S**QIQEW (*para*)	8.7	1.8
hC1284-o	DDA**C**FDII**C**DEEL**S**QIQEW (*ortho*)	4.5	0.8
hC1284-m	DDA**C**FDII**C**DEEL**S**QIQEW (*meta*)	2.5	0.1
hC1284-p	DDA**C**FDII**C**DEEL**S**QIQEW (*para*)	3.1	0.4
Optimized Combination			
Comb2	**R**DDA**C2**DII**C**DEE**α**SQIQEW (*meta*)	0.26	0.01

Table 3.2. Binding affinities for conformationally constrained FYCO1-derived peptides with LC3B protein. BLI and curve fitting were performed as described in Figure 3.2 and in Methods. Average K_d values and standard errors of the mean (Tables 3.1 and 3.2) were calculated from the individual curve fits of three independent replicates (Tables 3.5-3.7). **2** denotes 2-naphthylalanine, **α** denotes *tert*-butylalanine, and **C** denotes homocysteine. Stapled peptides have their two cysteines or homocysteines bis-alkylated by an *ortho*-, *meta*- or *para*-dibromomethylbenzene, as indicated. All peptides have a C-terminal amide group and an N-terminal biotin separated from the peptide by two beta-alanine residues. ND denotes no binding affinity detected up to 20 μM LC3B protein.

Having elucidated broad structure-activity relationships for the FYCO1 peptide, we next sought to introduce structure-stabilizing covalent cross-links. Side-chain-to-side-chain covalent cross-links, or “staples”, have most often been applied to alpha-helical peptides. In many cases, stapled alpha-helices have a greater extent of secondary structure, improved affinity and selectivity, improved cell penetration, and increased resistance to biological degradation.[151,152] Applying stapling strategies to non-helical peptides is significantly more challenging, but we and others have applied “diversity-

oriented stapling" methods to improve pharmacological properties of non-helical peptides.[132,136,143–149] These approaches do not assume a specific secondary structure, and thus are applicable to peptides that bind their targets in extended conformations such as FYCO1.

As described in previous work, we used solution dithiol bis-alkylation reactions for diversity-oriented stapling.[147,148,153] Before we could apply this strategy to the FYCO1 peptide, we had to substitute the native cysteine C1289. The C1289S analog had very similar binding affinity to the parent FYCO1 peptide (K_d value of 0.33 versus 0.29 μM, **Table 3.2**). Inspecting the crystal structure of the LC3B-bound FYCO1 peptide, we observed that an *(i,i+3)* staple between positions 1279 and 1282 or an *(i,i+5)* staple between positions 1279 and 1284 could potentially accommodate a thioether staple (**Fig. 3.1d**). We prepared analogs of FYCO1 with double substitutions of cysteine at V1279 and I1282, cysteine at V1279 and T1284, or homocysteine at V1279 and T1284 (to help bridge the longer distance), and cross-linked them with *ortho*-, *meta*-, or *para*-dibromoxylene as described.[147,148,153] In this manner, we produced a panel of eight uniquely constrained cyclic peptides (**Table 3.2**). All the *(i,i+3)* stapled peptides (C1282-o, C1282-m, and C1282-p) were poor LC3B ligands, with over a 30-fold loss in binding affinity compared to FYCO1. Both of the *(i,i+5)* stapled peptides that incorporated cysteines (peptides C1284-m and C1284-p) were similarly poor LC3B ligands. However, peptides that used homocysteines for the *(i,i+5)* staple had somewhat better affinity. The highest-affinity stapled peptide of this series, hC1284-m, had a 9-fold loss in affinity for LC3B compared to FYCO1 (K_d value of 2.5 μM).

Finally, we combined the three most beneficial individual substitutions (F1280Nap2, L1288tbA, and R-FYCO1) with the best-performing staple from peptide hC1284-m. Unexpectedly, this stapled peptide (Comb2) had a K_d of 0.26 μM, similar to the parent

peptide FYCO1 and only 2.2-fold poorer than the optimized linear peptide Comb1 (**Table 3.2**).

Comb1 and Comb2 have many alterations to the electrostatic and hydrophobic interactions involved in LC3B binding. We next examined whether these changes altered the selectivity of these peptides for LC3B over GABARAP. Using a BLI assay for GABARAP binding, we determined that Comb1 and Comb2 bound to GABARAP with K_d values of 0.67 and 1.4 μM, respectively (**Table 3.3**). Overall, the parent FYCO1 peptide binds LC3B with 5.1-fold selectivity over GABARAP, and Comb1 and Comb2 bind LC3B over GABARAP with 5.6-fold and 5.4-fold selectivity, respectively. These data demonstrate that LC3B selectivity was retained with the incorporation of multiple substitutions and stapling.

Name	Sequence	K_d for LC3B (μM)	Std Err (μM)	K_d for GABARAP (μM)	Std Err (μM)	LC3B selectivity
K1	DATYTWEHLAWP	18.7	1.9	0.39	0.08	0.02
FYCO1	DDAVFDIITDEELCQIQEW	0.29	0.01	1.4	0.02	5.1
Comb1	**R**DDAV**2**DIITDEE**α**CQIQEW	0.12	0.004	0.67	0.08	5.6
Comb2	**R**DDA**C**2DII**C**DEE**α**SQIQEW (meta)	0.26	0.01	1.4	0.03	5.4

Table 3.3. Binding affinities for FYCO1-derived peptides with GABARAP protein, and selectivities for LC3B over GABARAP. BLI and curve fitting were performed as described in Figure 3.2 and in Methods. Average K_d values and standard errors of the mean (Tables 3.1 and 3.2) were calculated from the individual curve fits of three independent replicates (Tables 3.5-3.10). **2** denotes 2-naphthylalanine, **α** denotes *tert*-butylalanine, and **C** denotes homocysteine. Comb2 has its homocysteines bis-alkylated by a *meta*-dibromomethylbenzene. All peptides have a C-terminal amide group and an N-terminal biotin separated from the peptide by two beta-alanine residues.

Often, introducing artificial amino acids and conformational constraints within a peptide increases its proteolytic stability. To assess the proteolytic stability of LC3B-binding peptides, we employed a rigorous cell lysate stability assay recently described for

stapled alpha-helical peptides.[127] We incubated peptides for various times between 1 and 24 hours in a HeLa cell lysate, then precipitated proteins in ice cold methanol and analyzed the supernatants by analytical HPLC (**Fig 3.3**, Fig 3.7). Surprisingly, the parent FYCO1 peptide showed little degradation for up to three hours, but by 24 hours only a third of the peptide was remaining. The optimized linear peptide, Comb1, had similar results. The optimized stapled peptide, Comb2, showed an unusual proteolytic stability profile. At 3 hours, there was less Comb2 remaining compared to FYCO1, but after 24 hours there was roughly double the amount of Comb2 remaining compared to FYCO1 (59% of intact Comb2 remaining after 24 hours). Despite the unusual result at 3 hours, we concluded that Comb2 was more resistant to degradation than FYCO1 and Comb1 over the long-term.

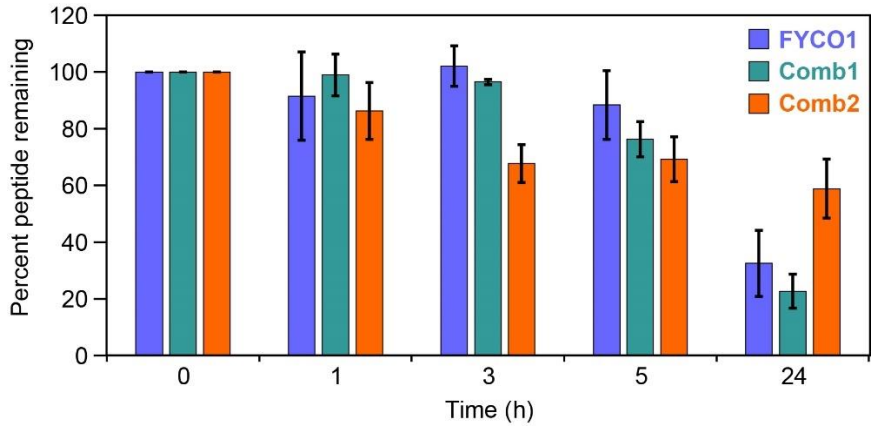

Figure 3.3. Proteolytic stability of peptides in HeLa cell lysates. Peptides FYCO1, Comb1 and Comb2 were incubated for selected time points in HeLa cell lysate at 37 °C.[127] Samples were quenched in methanol and supernatant analyzed by analytical HPLC. Areas under each peptide chromatogram peak were normalized to the area under the zero timepoint chromatogram peak. HPLC chromatograms are shown in Fig 3.7. Average values and standard errors of the mean were calculated from four independent replicates (representative primary data shown in Fig. 3.7).

3.3. Discussion

Many proteins have been shown to bind LC3B through their LIR motifs using co-immunoprecipitation or similar techniques. However, only a few prior studies have characterized LIR motif-LC3B binding quantitatively, and structure-activity relationships for this interaction are limited. Several prior papers showed that the LIR motif from FYCO1 binds LC3A/B selectively over LC3C and GABARAPs,[104,116,118] with varying degrees of selectivity.[115,154] Our work supports that the FYCO1 LIR motif is indeed moderately selective (roughly 5-fold) for LC3B over GABARAP. Additionally, our results extend prior understanding that negatively charged residues are important for LC3B binding,[116,118] showing that the most important contributor to LC3B binding, outside of the core LIR motif, is the negative charge at E1287. The negative charge at D1281 and polar interactions of the N-terminus of FYCO1 also play moderately important roles in LC3B binding.

Comparisons among hydrophobic residues in native LIR motifs have been performed,[104,113,116,117] but this work extends this understanding using artificial aliphatic and aromatic amino acids. Overall, in the context of the FYCO1-LC3B interaction, we found that targeting HP1 with larger hydrophobic amino acids improved binding while HP2 did not tolerate larger substitutions. Given the limited number of artificial amino acids we have tested so far, it is highly likely that further substitution of F1280 will produce analogs with even better affinity. Because the F1280Nap2 substitution and other modifications were synergistic with the *(i,i+5)* staple, these and other continued efforts should be done in the context of both linear and stapled peptides.

Optimized FYCO1 LIR peptides maintain moderate selectivity for LC3B over GABARAP. Recent work demonstrated that the residues C-terminal to the core LIR motif (here, residues 1285-1293) can greatly impact GABARAP/LC3B selectivity.[115] It is therefore

likely that this region of the peptide serves to preserve selectivity even in the presence of the N-terminal staple. While LIR-based peptide inhibitors of LC3B proteins with higher affinity were recently reported,[114] these were not selective for LC3B over GABARAP. Thus, to the best of our knowledge, Comb1 and Comb2 represent the highest-affinity Atg8 ligands that maintain LC3B selectivity over GABARAP.

This work also introduces an *(i,i+5)* stapled peptide, Comb2, with binding affinity and selectivity similar to the native FYCO1. Because peptide stapling has focused primarily on helical peptides which require stapling at *(i,i+3)*, *(i,i+4)* or *(i,i+7)* relative positions, this application of an *(i,i+5)* staple is highly unusual. One of the primary benefits of peptide stapling is improved stability in biological environments.[151,152] We tested this potential benefit in the context of the *(i,i+5)* stapled peptide Comb2 using a rigorous test of proteolytic stability.[127] We observed a roughly 2-fold reduction in peptide degradation over 24 hours compared to the Comb1 peptide, which allows us to attribute this modest benefit to the staple itself. Notably, this is less of an effect than is typically observed for stapled alpha-helices.[151] This may indicate that the extended structure imposed by the *(i,i+5)* staple offers less proteolytic resistance than a cooperatively folded alpha-helix. This explanation may also account for the unusual time dependence of proteolytic degradation observed for Comb2. Further exploration of non-helical stapled peptides will be required to more fully understand how staples affect structure and proteolytic degradation for non-helical peptides.

Comb1 and Comb2 are potent LC3-inhibiting peptides for assays using recombinant proteins, and for assays using cell lysates. Additional work will be required to translate LC3B-selective peptides into useful cellular probes. The most significant hurdle is cytosolic penetration.[66] While this work highlighted numerous negative charges that contribute only moderately to affinity, it remains clear that negative charge is required for

high-affinity binding to LC3B. Anionic peptides can be difficult to deliver to the interior of cells, even as fusions to cell-penetrating peptides. Advanced cell-penetrating peptides have demonstrated the ability to deliver anionic cargo, and these may provide a better means of efficiently delivering LIR motif peptides to the cytosol.[74–76] Future application of a wider diversity of stapling strategies and stapling positions may uncover new synergies that further optimize LC3B affinity, selectivity, proteolytic stability, and cytosolic penetration. The present work will directly inform those efforts, providing valuable tools for research into the basic mechanisms of autophagy and the links between autophagy and cancer.

3.4. Methods

3.4.1. Peptide Synthesis

All peptides were synthesized via standard Fmoc solid-phase peptide synthesis on an automated Tribute Peptide Synthesizer (Gyros Protein Technologies). Peptides were synthesized on Rink amide resin (substitution 0.55 mmol/g) with deprotection in 20% piperidine in DMF, and coupling with 5 equiv. each of amino acid, HBTU, and HOBt, and 10 equiv. of DIPEA. DMF washes were performed between each step. To prepare biotinylated peptides, the N-terminus was deprotected in 20% piperidine in DMF followed by overnight incubation in 5 equiv. of biotin-N-hydroxysuccinimide ester (Millipore Sigma) and 10 equiv. DIPEA in DMF. To prepare fluorescein-labeled peptides, 5 equiv. of 5,6-carboxyfluorescein succinimidyl ester (Thermo Fisher Scientific) were coupled overnight with 10 equiv. DIPEA in DMF. All peptides included a C-terminal tryptophan for spectrophotometric concentration determination, and two beta-alanine residues between the N-terminus of the FYCO1-derived sequence and the fluorescein or biotin. All peptides were globally deprotected and cleaved using a TFA cleavage cocktail (95:2:2:1, TFA:H_2O:EDT:TIPS) for 3 hours. Following cleavage, peptides were precipitated in cold

diethyl ether, pelleted, and washed with additional diethyl ether. Peptides were then dried and resuspended in 50:50 water:acetonitrile for reverse-phase HPLC purification on a preparative-scale C_8 column using a gradient of 5 – 100% acetonitrile in 30 min. Peptides were purified to at least 95% purity as determined by analytical HPLC. Masses were determined using MALDI-TOF mass spectrometry with a matrix of 10 mg/mL α-cyano-4-hydroxycinnamate in 50:50 water:acetonitrile with 0.1% TFA. Observed masses of final products are given in supplemental figure S1. Following purification, peptides were lyophilized and resuspended in DMSO for working solutions, which were quantified based on absorbance at 280 nm (Thermo Scientific Nanodrop 1000).

3.4.2. Protein Expression

LC3B protein was expressed and purified as described.[155] BL21 *E. coli* were transformed with a pET-15b expression plasmid for full-length LC3B (codons 1-125). Transfected cells were grown on ampicillin agar plates and colonies were selected and grown in LB culture medium. At an optical density of 0.6 to 0.8, 1 mM IPTG was added and cells were incubated for 3 hours at 37 °C. Cells were pelleted and resuspended in a lysis buffer of 50 mM Tris pH 8.0, 300 mM NaCl, 5 mM imidazole, 0.2% lysozyme, 1 protease inhibitor cocktail pellet (Roche), and 2.5 U/mL universal nuclease (Pierce). Resuspended cells were sonicated and lysed, and the lysate was centrifuged to pellet debris. The protein was purified from clarified lysate using Ni-NTA resin by incubating protein with resin for 45 min at 4 °C, rinsing with wash buffer (50 mM Tris pH 8.0, 300 mM NaCl, 5 mM imidazole), and then eluting in 50 mM Tris pH 8.0, 300 mM NaCl, 250 mM imidazole at 4°C. The eluate was further purified by size exclusion chromatography using an automated FPLC system (AKTA, GE) on a Superdex S75 analytical column in 25 mM Tris pH 7.5, 150 mM NaCl, 1 mM EDTA, and 0.05% 2-mercaptoethanol. Protein fractions were analyzed via SDS-PAGE, and pure fractions were pooled together.

Concentration of protein was quantified via absorbance at 280 nm and confirmed via BCA assay. Protein was stored in frozen aliquots at -80°C.

For GABARAP protein expression, BL21 *E. coli* were transformed with a pGex-4T-2 expression plasmid for full-length GABARAP (codons 1-117).[156] Expression and lysis was performed in the same manner as with LC3B protein. For purification, glutathione resin was incubated with clarified lysate for 45 min at 4 °C before rinsing with PBS. The GST tag was then removed overnight with thrombin protease treatment at 4 °C and the cleaved protein was eluted from the column. Protein fractions were analyzed via SDS-PAGE and pure fractions were pooled. Concentrations were quantified via absorbance at 280 nm (Thermo Scientific Nanodrop 1000) and confirmed via BCA assay. Protein was stored in frozen aliquots at -80 °C.

3.4.3. Biolayer Interferometry

BLI assays were performed on an Octet K2 System (Forté Bio). Biotinylated peptides and proteins were diluted to 0.5 µg/mL in assay buffer (PBS pH 7.4, 0.02% Tween-20, 0.5 mg/mL BSA) at a final volume of 200 µL in a flat, black 96-well polypropylene plate (Greiner Bio-One). Biotinylated peptides were loaded onto streptavidin-coated tips, tips were washed, and then 200 seconds of association of LC3B or GABARAP protein was measured. Following association of the protein with the immobilized peptide, dissociation of the protein was measured for an additional 200 seconds. Assays were run at 30 °C with shaking at 1000 rpm. Protein concentrations were varied in order to achieve a response of 0.3 nm association or higher, with protein concentration not exceeding 20 µM for LC3B or 4 µM for GABARAP. Curve fitting was generated using a 1:1 fitting model by Octet DataAnalysis software (FortéBio). K_{obs} values were extracted from these curve fits, and K_{obs} was plotted versus protein concentration. The slope of this line provided the association rate (K_{on}). The dissociation rate was extracted from the 1:1

curve fit to the dissociation data. Finally, K_d values were calculated by dividing the K_{off} by the K_{on}. All peptides were tested in three separate replicates and average K_d, K_{on}, and K_{off} values and standard error were calculated (see Tables 3.5-3.10 in Supplementary Information).

3.4.4. Fluorescence Polarization Assays

Fluorescence polarization assays were performed as described.[28] Dye-labeled peptide was mixed at a final concentration of 10 nM with a serial dilution of LC3B or GABARAP protein in a final reaction volume of 20 µL in a black, flat-bottomed 384-well polypropylene plate (Greiner Bio-One). The buffer composition was PBS pH 7.3 with 0.1% Tween-20. The plate was incubated in the dark for 1 hr at room temperature, then read at 494 nm excitation and 519 nm emission. K_d values were obtained from curve fits using KaleidaGraph software as described.[44]

3.4.5. Lysate Stability Assay

For lysate stability assays, HeLa cells were trypsinized, washed in PBS, pelleted, and treated with lysis buffer (50 mM Tris, 250 mM NaCl, 0.5% IGEPAL CA-630 detergent, pH 8.0) on ice for 15 min. Then, lysates were centrifuged for 10 min at 4 °C at 14,800 rpm and the clarified lysate was collected. Peptides were added to the lysate to a concentration of 150 µM and were incubated at 37 °C. Aliquots of 40 µL were taken at each time point and quenched in 160 µL of ice-cold methanol. Samples were spun down for 10 min at 14,800 rpm prior to analysis via reverse-phase analytical HPLC on a C_{18} column. Chromatogram peaks were integrated to measure amount of peptide remaining at each time point. Peak volumes for each timepoint were normalized to the zero-hour timepoint to determine percentage of peptide remaining. Data presented is the average of four biological replicates performed with different lysates on different days.

3.5. Supplemental Materials

Name	Sequence*	Expected Mass [M+H$^+$]	Observed Mass [M+H$^+$]
FYCO1	DDAVFDIITDEELCQIQEW	2650.9	2650.9
Δ1276-1279	FDIITDEELCQIQEW	2250.5	2247.6
Δ1289-1293	DDAVFDIITDEELW	2049.3	2049.1
Δ1292-1293	DDAVFDIITDEELCQIW	2393.7	2395.4
D1276N	NDAVFDIITDEELCQIQEW	2650.0	2648.7
D1277N	DNAVFDIITDEELCQIQEW	2650.0	2649.9
D1281N	DDAVFNIITDEELCQIQEW	2650.0	2647.0
D1285N	DDAVFDIITNEELCQIQEW	2650.0	2648.2
E1286Q	DDAVFDIITDQELCQIQEW	2650.0	2650.1
E1287Q	DDAVFDIITDEQLCQIQEW	2650.0	2648.0
E1293Q	DDAVFDIITDEELCQIQQW	2650.0	2648.0
D1276N/D1277N	NNAVFDIITDEELCQIQEW	2649.0	2649.2
F1280Nap2	DDAV2DIITDEELCQIQEW	2701.0	2698.2
F1280Nap1	DDAV1DIITDEELCQIQEW	2701.0	2699.0
I1283F	DDAVFDIFTDEELCQIQEW	2685.0	2681.5
I1283Nap2	DDAVFDI2TDEELCQIQEW	2735.0	2736.5
L1288NL5	DDAVFDIITDEEνCQIQEW	2679.0	2675.8
L1288tbA	DDAVFDIITDEEαCQIQEW	2665.0	2662.5
I1291tbA	DDAVFDIITDEELCQαQEW	2665.0	2663.0
I1291F	DDAVFDIITDEELCQFQEW	2685.0	2681.8
A1278r	DDrVFDIITDEELCQIQEW	2736.0	2733.5
R-FYCO1	RDDAVFDIITDEELCQIQEW	2807.1	2805.1
RR-FYCO1	RRDDAVFDIITDEELCQIQEW	2963.3	2961.2
C1289S	DDAVFDIITDEELSQIQEW	2634.9	2635.9
C1282-o	DDACFDCITDEELSQIQEW (*ortho*)	2731.0	2729.2
C1282-m	DDACFDCITDEELSQIQEW (*meta*)	2731.0	2728.5
C1282-p	DDACFDCITDEELSQIQEW (*para*)	2731.0	2727.4
C1284-m	DDACFDIICDEELSQIQEW (*meta*)	2743.0	2741.7
C1284-p	DDACFDIICDEELSQIQEW (*para*)	2743.0	2741.0
hC1284-o	DDAC̲FDII C̲DEELSQIQEW (*ortho*)	2771.1	2770.0
hC1284-m	DDAC̲FDII C̲DEELSQIQEW (*meta*)	2771.1	2768.5
hC1284-p	DDAC̲FDII C̲DEELSQIQEW (*para*)	2771.1	2768.7
Comb1	RDDAV2DIITDEEαCQIQEW	2871.2	2868.7
Comb2	RDDAC2DIICDEEαSQIQEW (*meta*)	2991.4	2991.6
K1	DATYTWEHLAWP	1858.1	1855.7
flu-K1	*DATYTWEHLAWP	1990.1	1990.4

flu-FYCO1	*DDAVFDIITDEELCQIQEW	2782.9	2782.1

Table 3.4. Expected and observed masses table of all synthesized LIR peptides. *All peptides have a C-terminal amide and an N-terminal biotin attached to the sequence shown via a linker consisting of two beta-alanines, except for flu-K1 and flu-FYCO1 which each have a fluorescein instead of a biotin. **2** denotes 2-naphthylalanine, **1** denotes 1-naphthylalanine, ν denotes 5,5-dimethylnorleucine, α denotes *tert*-butylalanine, **r** denotes D-arginine, and **C** denotes homocysteine. Stapled peptides have their two cysteines or homocysteines bis-alkylated by an *ortho*-, *meta*- or *para*-dibromomethylbenzene, as indicated.[147]

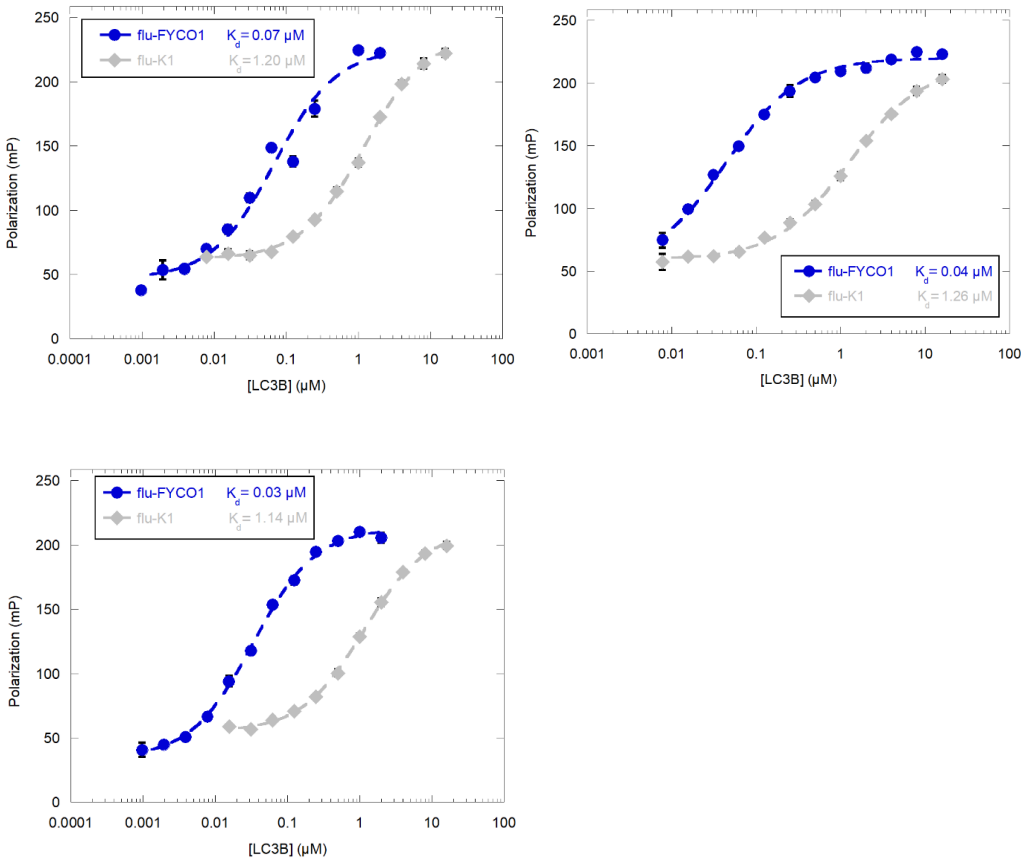

Figure 3.4. Fluorescence polarization data for binding of flu-FYCO1 and flu-K1 with recombinant LC3B. The final concentration of each fluorescein-labeled peptide was 10 nM. Assays were incubated for 45 min at room temperature before measuring, and raw polarization values are displayed. Curve fitting and K_d values were obtained using KaleidaGraph software and first-principles K_d curve fits as described.[136] Each of these three independent replicates were performed with three technical replicates (error bars show standard error of the mean for the three technical replicates). Average K_d values and standard errors of the mean for K_d values were calculated from the individual curve fits of the three independent replicates.

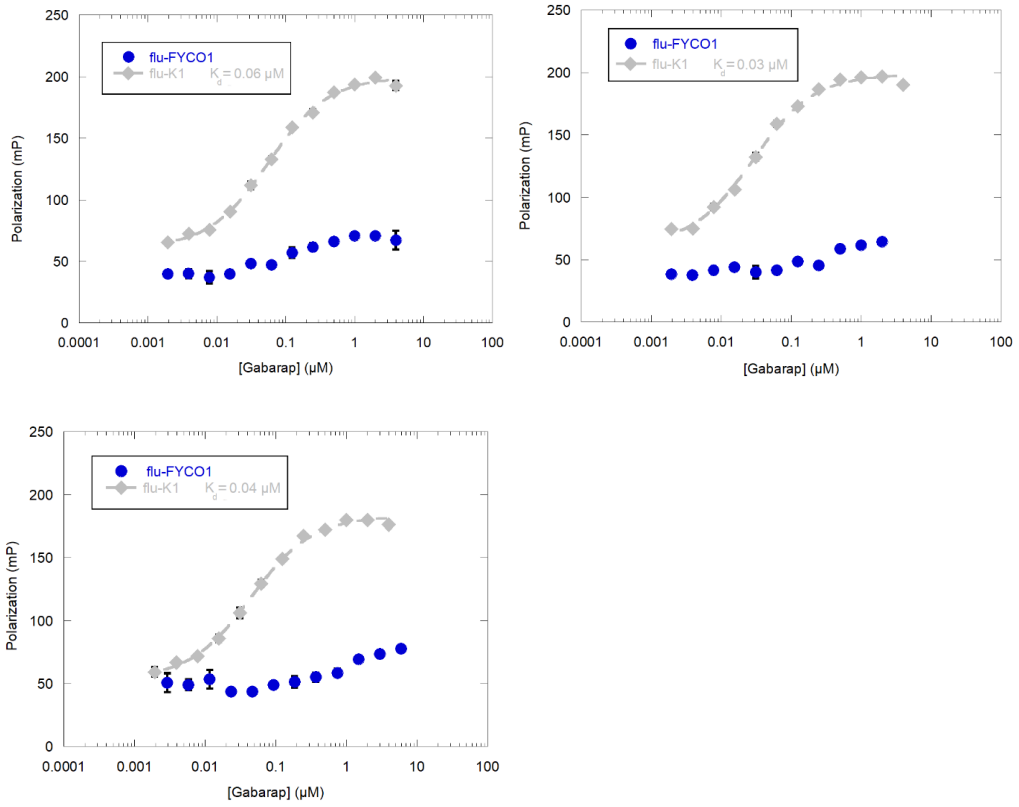

Figure 3.5. Fluorescence polarization data for binding of flu-FYCO1 and flu-K1 with recombinant GABARAP. The final concentration of each fluorescein-labeled peptide was 10 nM. Assays were incubated for 45 min at room temperature before measuring, and raw polarization values are displayed. Curve fitting and K_d values were obtained using KaleidaGraph software and first-principles K_d curve fits as described.[136] Each of these three independent replicates were performed with three technical replicates (error bars show standard error of the mean for the three technical replicates). Average K_d values and standard errors of the mean for K_d values were calculated from the individual curve fits of the three independent replicates.

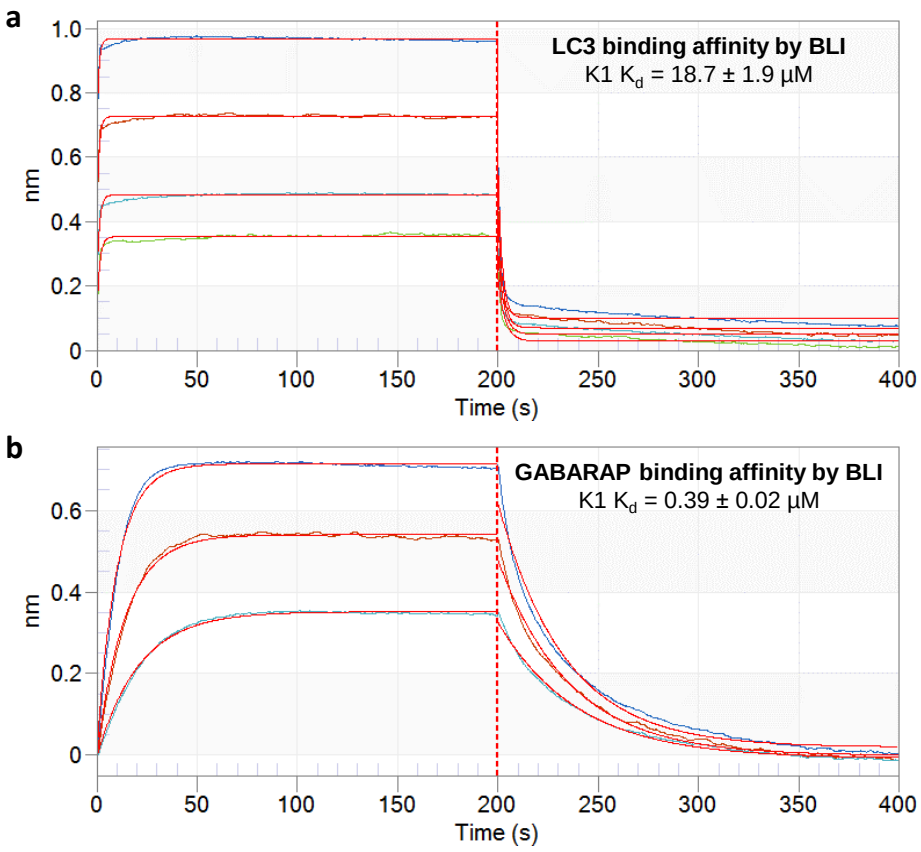

Figure 3.6. Biolayer interferometry data (BLI) for biotinylated K1 peptide (K1) with recombinant human GABARAP and LC3B. BLI was performed with 0.5 µg/mL of biotinylated peptides loaded onto streptavidin-coated biosensors with serial dilutions of protein at 30 °C. Association and dissociation steps were measured for 200 seconds each. Curve fitting was performed using the Octet DataAnalysis software (Forté Bio) and K_d values were calculated as described in Methods. Shown are primary data (colored traces) and curve fits (red curves) for incubation with 2, 1, 0.5, and 0.25 µM for LC3, and 1, 0.5, 0.25 µM for GABARAP. Data shown is one representative data set from three independent replicates.

Name	Peptide Sequence	Trial 1 K_d (µM)	Trial 2 K_d (µM)	Trial 3 K_d (µM)	Avg K_d (µM)	Std Err (µM)
K1	DATYTWEHLAWP	15.5	22.1	18.6	18.7	1.9
FYCO1	DDAVFDIITDEELCQIQEW	0.28	0.28	0.30	0.29	0.01
Termini Truncations						
Δ1276-1279	FDIITDEELCQIQEW	ND	ND	ND	ND	ND
Δ1289-1293	DDAVFDIITDEELW	4.1	2.1	3.1	3.1	0.6

Δ1292-1293	DDAVFDIITDEELCQIW	0.49	0.49	0.41	0.46	0.03
Gln/Asn Scan of Negative Residues						
D1276N	NDAVFDIITDEELCQIQEW	0.31	0.37	0.37	0.35	0.02
D1277N	DNAVFDIITDEELCQIQEW	0.52	0.52	0.40	0.48	0.04
D1281N	DDAVFNIITDEELCQIQEW	1.5	0.93	0.83	1.1	0.2
D1285N	DDAVFDIITNEELCQIQEW	0.38	0.39	0.44	0.41	0.02
E1286Q	DDAVFDIITDQELCQIQEW	0.63	0.89	0.76	0.76	0.07
E1287Q	DDAVFDIITDEQLCQIQEW	3.4	2.2	2.4	2.7	0.4
E1293Q	DDAVFDIITDEELCQIQQW	0.31	0.30	0.30	0.30	0.005
D1276N/ D1277N	NNAVFDIITDEELCQIQEW	1.2	1.1	1.2	1.2	0.03
Hydrophobic Mutations						
F1280Nap 2	DDAV2DIITDEELCQIQEW	0.19	0.14	0.10	0.14	0.02
F1280Nap 1	DDAV1DIITDEELCQIQEW	0.16	0.19	0.17	0.17	0.01
I1283F	DDAVFDIFTDEELCQIQEW	5.6	6.0	6.1	5.9	0.2
I1283Nap 2	DDAVFDI2TDEELCQIQEW	2.7	2.5	2.8	2.6	0.1
L1288NL5	DDAVFDIITDEEνCQIQEW	0.56	0.53	0.66	0.58	0.04
L1288tbA	DDAVFDIITDEEαCQIQEW	0.23	0.26	0.25	0.25	0.01
I1291tbA	DDAVFDIITDEELCQαQEW	0.50	0.42	0.42	0.44	0.03
I1291F	DDAVFDIITDEELCQFQEW	0.77	0.75	0.67	0.73	0.03
Introduction of Positive Charge						
A1278r	DDrVFDIITDEELCQIQEW	0.92	1.0	0.79	0.90	0.06
R-FYCO1	RDDAVFDIITDEELCQIQEW	0.22	0.21	0.18	0.20	0.01
RR-FYCO1	RRDDAVFDIITDEELCQIQEW	0.31	0.32	0.35	0.33	0.01
Conformational Constraints						
C1289S	DDAVFDIITDEELSQIQEW	0.27	0.39	0.34	0.33	0.03
C1282-o	DDACFDCITDEELSQIQEW ortho	ND	ND	ND	ND	ND
C1282-m	DDACFDCITDEELSQIQEW meta	9.3	7.0	8.7	8.3	0.7
C1282-p	DDACFDCITDEELSQIQEW para	7.3	12.8	11.3	10.5	1.7
C1284-m	DDACFDIICDEELSQIQEW meta	5.7	6.8	6.5	6.3	0.3
C1284-p	DDACFDIICDEELSQIQEW para	8.0	5.9	12.2	8.7	1.8
hC1284-o	DDACFDIICDEELSQIQEW ortho	2.9	5.1	5.4	4.4	0.8
hC1284-m	DDACFDIICDEELSQIQEW meta	2.6	2.3	2.7	2.5	0.1
hC1284-p	DDACFDIICDEELSQIQEW para	3.0	2.5	3.7	3.1	0.4

Optimized Combinations						
Comb1	RDDAV2DIITDEEαCQIQEW	0.12	0.11	0.13	0.12	0.004
Comb2	RDDAC2DIICDEEαSQIQEW meta	0.24	0.26	0.27	0.26	0.01

Table 3.5. Individual replicates for binding affinities for FYCO1-derived peptides with LC3B protein. BLI and curve fitting were performed as described in Figure 2 and in Methods. Average K_d values and standard errors of the mean (Tables 3.1 and 3.2) were calculated from the individual curve fits of these three independent replicates. **2** denotes 2-naphthylalanine, **1** denotes 1-naphthylalanine, **ν** denotes 5,5-dimethylnorleucine, **α** denotes *tert*-butylalanine, **r** denotes D-arginine, and **C** denotes homocysteine. Stapled peptides have their two cysteines or homocysteines bis-alkylated by an *ortho*-, *meta*- or *para*-dibromomethylbenzene, as indicated. All peptides have a C-terminal amide group and an N-terminal biotin separated from the peptide by two beta-alanine residues. ND denotes no binding affinity detected up to 20 μM LC3B protein.

Name	Peptide Sequence	Trial 1 K_{on} (1/Ms)	Trial 2 K_{on} (1/Ms)	Trial 3 K_{on} (1/Ms)	Avg K_{on} (1/Ms)	Std Err (1/Ms)
K1	DATYTWEHLAWP	2.6E-05	1.7E-05	2.2E-05	2.2E-05	2.5E-06
FYCO1	DDAVFDIITDEELCQIQEW	1.3E-04	1.1E-04	1.0E-04	1.1E-04	7.0E-06
Termini Truncations						
Δ1276-1279	FDIITDEELCQIQEW	ND	ND	ND	ND	ND
Δ1289-1293	DDAVFDIITDEELW	5.8E-05	5.2E-05	6.9E-05	6.0E-05	4.8E-06
Δ1292-1293	DDAVFDIITDEELCQIW	2.2E-04	2.0E-04	2.0E-04	2.1E-04	5.2E-06
Gln/Asn Scan of Negative Residues						
D1276N	NDAVFDIITDEELCQIQEW	1.7E-04	1.2E-04	1.3E-04	1.4E-04	1.6E-05
D1277N	DNAVFDIITDEELCQIQEW	1.1E-04	1.2E-04	1.6E-04	1.3E-04	1.4E-05
D1281N	DDAVFNIITDEELCQIQEW	1.1E-04	1.5E-04	1.5E-04	1.4E-04	1.4E-05
D1285N	DDAVFDIITNEELCQIQEW	1.4E-04	1.5E-04	1.3E-04	1.4E-04	5.2E-06
E1286Q	DDAVFDIITDQELCQIQEW	1.5E-04	1.3E-04	1.9E-04	1.5E-04	1.9E-05
E1287Q	DDAVFDIITDEQLCQIQEW	6.5E-05	9.8E-05	9.4E-05	8.6E-05	1.0E-05
E1293Q	DDAVFDIITDEELCQIQQW	1.9E-04	1.5E-04	1.7E-04	1.7E-04	1.1E-05
D1276N/ D1277N	NNAVFDIITDEELCQIQEW	9.9E-05	9.4E-05	9.9E-05	9.7E-05	1.6E-06
Hydrophobic Mutations						

F1280Nap2	DDAV2DIITDEELCQIQEW	1.2E-04	1.7E-04	1.8E-04	1.6E-04	1.8E-05
F1280Nap1	DDAV1DIITDEELCQIQEW	1.5E-04	1.4E-04	1.4E-04	1.4E-04	2.7E-06
I1283F	DDAVFDIFTDEELCQIQEW	6.0E-05	6.2E-05	6.2E-05	6.1E-05	4.9E-07
I1283Nap2	DDAVFDI2TDEELCQIQEW	1.2E-04	1.4E-04	1.2E-04	1.3E-04	5.2E-06
L1288NL5	DDAVFDIITDEEνCQIQEW	1.5E-04	1.5E-04	1.3E-04	1.4E-04	6.1E-06
L1288tbA	DDAVFDIITDEEαCQIQEW	1.3E-04	1.3E-04	1.4E-04	1.4E-04	2.0E-06
I1291tbA	DDAVFDIITDEELCQαQEW	1.2E-04	1.3E-04	1.2E-04	1.2E-04	2.4E-06
I1291F	DDAVFDIITDEELCQFQEW	1.2E-04	1.1E-04	1.2E-04	1.2E-04	2.0E-06
Introduction of Positive Charge						
A1278r	DDrVFDIITDEELCQIQEW	1.0E-04	1.0E-04	1.3E-04	1.1E-04	9.7E-06
R-FYCO1	RDDAVFDIITDEELCQIQEW	1.1E-04	8.8E-05	1.2E-04	1.1E-04	1.0E-05
RR-FYCO1	RRDDAVFDIITDEELCQIQEW	9.6E-05	8.5E-05	8.8E-05	9.0E-05	3.3E-06
Conformational Constraints						
C1289S	DDAVFDIITDEELSQIQEW	1.8E-04	1.5E-04	1.3E-04	1.5E-04	1.4E-05
C1282-o	DDACFDCITDEELSQIQEW ortho	ND	ND	ND	ND	ND
C1282-m	DDACFDCITDEELSQIQEW meta	3.8E-05	5.1E-05	3.8E-05	4.2E-05	4.4E-06
C1282-p	DDACFDCITDEELSQIQEW para	3.3E-05	2.9E-05	3.5E-05	3.3E-05	1.7E-06
C1284-m	DDACFDIICDEELSQIQEW meta	2.7E-05	3.0E-05	2.7E-05	2.8E-05	7.7E-07
C1284-p	DDACFDIICDEELSQIQEW para	2.8E-05	3.9E-05	2.5E-05	3.1E-05	4.1E-06
hC1284-o	DDACFDIICDEELSQIQEW ortho	8.9E-05	6.1E-05	5.8E-05	6.9E-05	1.0E-05
hC1284-m	DDACFDIICDEELSQIQEW meta	9.0E-05	8.5E-05	7.9E-05	8.5E-05	3.1E-06
hC1284-p	DDACFDIICDEELSQIQEW para	7.2E-05	7.3E-05	6.7E-05	7.1E-05	1.8E-06

Optimized Combinations						
Comb1	RDDAV2DIITDEEαCQIQEW	1.3E-04	1.4E-04	1.2E-04	1.3E-04	6.3E-06
Comb2	RDDAC2DIICDEEαSQIQEW meta	2.2E-04	2.0E-04	1.9E-04	2.1E-04	8.6E-06

Table 3.6. Individual replicates for binding on-rates for FYCO1-derived peptides with LC3B protein. BLI and curve fitting were performed as described in Figure 3.2 and in

Methods. Average K_d values and standard errors of the mean (Tables 3.1 and 3.2) were calculated from the individual curve fits of these three independent replicates. **2** denotes 2-naphthylalanine, **1** denotes 1-naphthylalanine, **ν** denotes 5,5-dimethylnorleucine, **α** denotes *tert*-butylalanine, **r** denotes D-arginine, and **C** denotes homocysteine. Stapled peptides have their two cysteines or homocysteines bis-alkylated by an *ortho*-, *meta*- or *para*-dibromomethylbenzene, as indicated. All peptides have a C-terminal amide group and an N-terminal biotin separated from the peptide by two beta-alanine residues. ND denotes no binding affinity detected up to 20 μM LC3B protein.

Name	Peptide Sequence	Trial 1 K_{off} (s^{-1})	Trial 2 K_{off} (s^{-1})	Trial 3 K_{off} (s^{-1})	Avg K_{off} (s^{-1})	Std Err (s^{-1})
K1	DATYTWEHLAWP					
FYCO1	DDAVFDIITDEELCQIQEW	0.04	0.03	0.03	0.03	0.002
Termini Truncations						
Δ1276-1279	FDIITDEELCQIQEW	ND	ND	ND	ND	ND
Δ1289-1293	DDAVFDIITDEELW	0.24	0.11	0.21	0.19	0.04
Δ1292-1293	DDAVFDIITDEELCQIW	0.09	0.10	0.10	0.09	0.003
Gln/Asn Scan of Negative Residues						
D1276N	NDAVFDIITDEELCQIQEW	0.05	0.05	0.05	0.05	0.003
D1277N	DNAVFDIITDEELCQIQEW	0.06	0.06	0.06	0.06	0.002
D1281N	DDAVFNIITDEELCQIQEW	0.17	0.14	0.13	0.15	0.01
D1285N	DDAVFDIITNEELCQIQEW	0.05	0.06	0.06	0.06	0.002
E1286Q	DDAVFDIITDQELCQIQEW	0.11	0.11	0.12	0.11	0.003
E1287Q	DDAVFDIITDEQLCQIQEW	0.22	0.21	0.22	0.22	0.004
E1293Q	DDAVFDIITDEELCQIQQW	0.06	0.05	0.05	0.05	0.004
D1276N/ D1277N	NNAVFDIITDEELCQIQEW	0.12	0.11	0.12	0.12	0.005
Hydrophobic Mutations						
F1280Nap2	DDAV2DIITDEELCQIQEW	0.02	0.02	0.02	0.02	0.002
F1280Nap1	DDAV1DIITDEELCQIQEW	0.02	0.03	0.02	0.02	0.001
I1283F	DDAVFDIFTDEELCQIQEW	0.34	0.37	0.38	0.36	0.01
I1283Nap2	DDAVFDI2TDEELCQIQEW	0.34	0.34	0.34	0.34	0.003
L1288NL5	DDAVFDIITDEEνCQIQEW	0.08	0.08	0.09	0.08	0.002
L1288tbA	DDAVFDIITDEEαCQIQEW	0.03	0.03	0.03	0.03	0.001
I1291tbA	DDAVFDIITDEELCQαQEW	0.06	0.05	0.05	0.06	0.003
I1291F	DDAVFDIITDEELCQFQEW	0.09	0.09	0.08	0.09	0.004
Introduction of Positive Charge						
A1278r	DDrVFDIITDEELCQIQEW	0.10	0.10	0.10	0.10	0.003

R-FYCO1	RDDAVFDIITDEELCQIQEW	0.02	0.02	0.02	0.02	0.002
RR-FYCO1	RRDDAVFDIITDEELCQIQEW	0.03	0.03	0.03	0.03	0.001
Conformational Constraints						
C1289S	DDAVFDIITDEELSQIQEW	0.05	0.05	0.05	0.05	0.001
C1282-o	DDACFDCITDEELSQIQEW ortho	ND	ND	ND	ND	ND
C1282-m	DDACFDCITDEELSQIQEW meta	0.35	0.36	0.33	0.34	0.01
C1282-p	DDACFDCITDEELSQIQEW para	0.24	0.37	0.40	0.34	0.05
C1284-m	DDACFDIICDEELSQIQEW meta	0.15	0.20	0.18	0.18	0.01
C1284-p	DDACFDIICDEELSQIQEW para	0.22	0.23	0.31	0.25	0.03
hC1284-o	DDACFDIICDEELSQIQEW ortho	0.26	0.31	0.31	0.29	0.02
hC1284-m	DDACFDIICDEELSQIQEW meta	0.23	0.19	0.22	0.21	0.01
hC1284-p	DDACFDIICDEELSQIQEW para	0.22	0.18	0.25	0.22	0.02
Optimized Combinations						
Comb1	RDDAV2DIITDEEαCQIQEW	0.02	0.02	0.02	0.02	0.0003
Comb2	RDDAC2DIICDEEαSQIQEW meta	0.05	0.05	0.05	0.05	0.0007

Table 3.7. Individual replicates for binding off-rates for FYCO1-derived peptides with LC3B protein. BLI and curve fitting were performed as described in Figure 3.2 and in Methods. Average K_d values and standard errors of the mean (Tables 3.1 and 3.2) were calculated from the individual curve fits of these three independent replicates. **2** denotes 2-naphthylalanine, **1** denotes 1-naphthylalanine, **ν** denotes 5,5-dimethylnorleucine, **α** denotes *tert*-butylalanine, **r** denotes D-arginine, and **C** denotes homocysteine. Stapled peptides have their two cysteines or homocysteines bis-alkylated by an *ortho*-, *meta*- or *para*-dibromomethylbenzene, as indicated. All peptides have a C-terminal amide group and an N-terminal biotin separated from the peptide by two beta-alanine residues. ND denotes no binding affinity detected up to 20 μM LC3B protein.

Name	Peptide Sequence	Trial 1 K_d (μM)	Trial 2 K_d (μM)	Trial 3 K_d (μM)	Avg K_d (μM)	Std Err (μM)
K1	DATYTWEHLAWP	0.36	0.42	0.39	0.39	0.02
FYCO1	DDAVFDIITDEELCQIQEW	1.5	1.4	1.5	1.4	0.02
Comb1	RDDAV2DIITDEEαCQIQEW	0.83	0.61	0.56	0.67	0.08

Comb2	RDDAC2DIICDEEαSQIQEW meta	1.3	1.4	1.3	1.4	0.03

Table 3.8. Individual replicates for binding affinities for K1 and FYCO1-derived peptides with GABARAP protein. BLI and curve fitting were performed as described in Figure 3.2 and in Methods. Average K_d values and standard errors of the mean (Table 3.3) were calculated from the individual curve fits of these three independent replicates. **2** denotes 2-naphthylalanine, α denotes *tert*-butylalanine, and **C** denotes homocysteine. Stapled peptide Comb2 has its homocysteines bis-alkylated by a *meta*-dibromomethylbenzene. All peptides have a C-terminal amide group and an N-terminal biotin separated from the peptide by two beta-alanine residues.

Name	Peptide Sequence	Trial 1 K_{on} (1/Ms)	Trial 2 K_{on} (1/Ms)	Trial 3 K_{on} (1/Ms)	Avg K_{on} (1/Ms)	Std Err (1/Ms)
K1	DATYTWEHLAWP	8.5E-05	6.7E-05	8.1E-05	7.7E-05	5.4E-06
FYCO1	DDAVFDIITDEELCQIQEW	6.7E-05	7.1E-05	6.9E-05	6.9E-05	1.4E-06
Comb1	RDDAV2DIITDEEαCQIQEW	4.0E-05	5.4E-05	6.2E-05	5.2E-05	6.5E-06
Comb2	RDDAC2DIICDEEαSQIQEW meta	7.4E-05	7.2E-05	7.8E-05	7.4E-05	1.7E-06

Table 3.9. Individual replicates for binding on-rates for K1 and FYCO1-derived peptides with GABARAP protein. BLI and curve fitting were performed as described in Figure 3.2 and in Methods. Average K_d values and standard errors of the mean (Table 3.3) were calculated from the individual curve fits of these three independent replicates. **2** denotes 2-naphthylalanine, α denotes *tert*-butylalanine, and **C** denotes homocysteine. Stapled peptide Comb2 has its homocysteines bis-alkylated by a *meta*-dibromomethylbenzene. All peptides have a C-terminal amide group and an N-terminal biotin separated from the peptide by two beta-alanine residues.

Name	Peptide Sequence	Trial 1 K_{off} (s^{-1})	Trial 2 K_{off} (s^{-1})	Trial 3 K_{off} (s^{-1})	Avg K_{off} (s^{-1})	Std Err (s^{-1})
K1	DATYTWEHLAWP	0.03	0.03	0.03	0.03	0.001
FYCO1	DDAVFDIITDEELCQIQEW	0.10	0.10	0.10	0.10	0.002
Comb1	RDDAV2DIITDEEαCQIQEW	0.03	0.03	0.04	0.03	0.001
Comb2	RDDAC2DIICDEEαSQIQEW meta	0.10	0.10	0.10	0.10	0.001

Table 3.10. Individual replicates for binding off-rates for K1 and FYCO1-derived peptides with GABARAP protein. BLI and curve fitting were performed as described in Figure 3.2 and in Methods. Average K_d values and standard errors of the mean (Table 3.3) were calculated from the individual curve fits of these three independent replicates. **2** denotes 2-naphthylalanine, α denotes *tert*-butylalanine, and **C** denotes homocysteine. Stapled peptide Comb2 has its homocysteines bis-alkylated by a *meta*-dibromomethylbenzene. All peptides have a C-terminal amide group and an N-terminal biotin separated from the peptide by two beta-alanine residues.

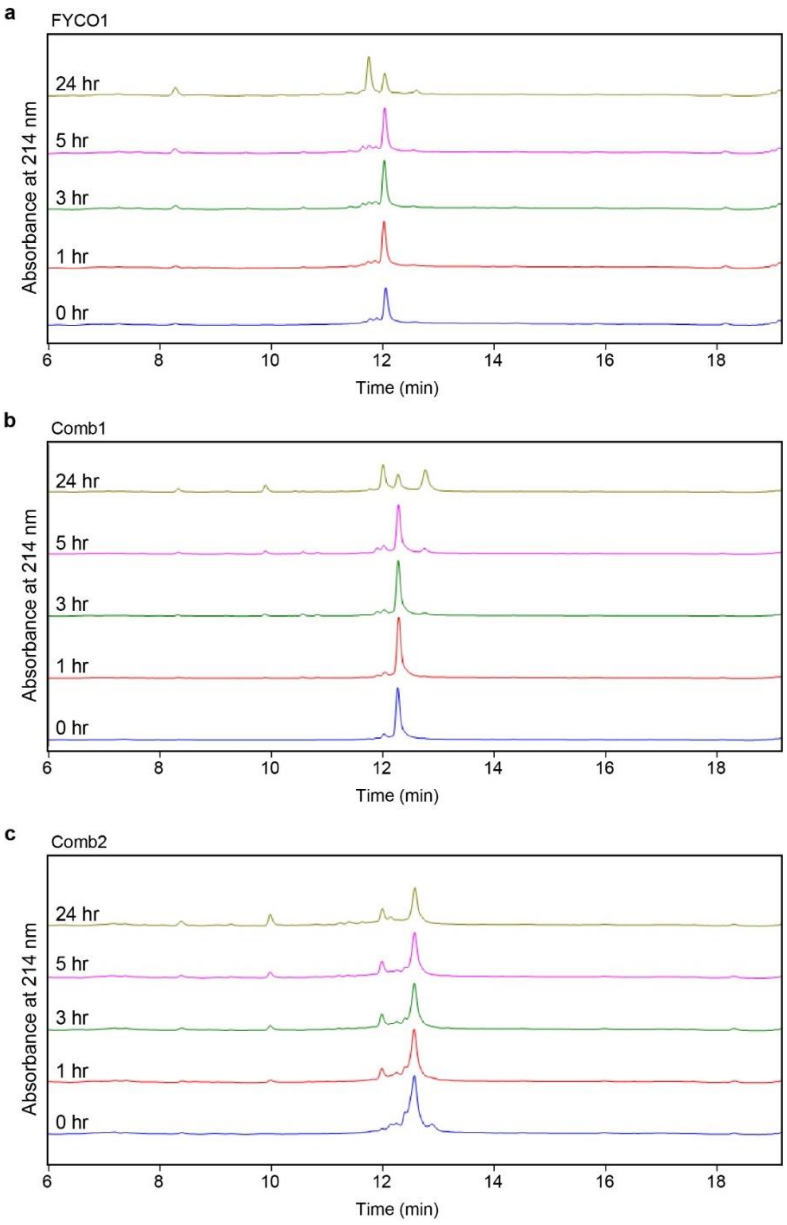

Figure 3.7. Representative HPLC analysis for selected peptides incubated in HeLa cell lysate. Peptides incubated at 37 °C for the time indicated.[127,137] Areas under each peptide chromatogram peak were normalized to the zero hour timepoint area (**Fig 3.3**). Experiments were performed with a total of 4 biological replicates for each peptide.

* All figures and tables in this chapter were based off of my own experimental results and analysis except for Fig 3.2a,b, Fig 3.4, and Fig 3.5. These experiments were performed in collaboration with Hawley Brown. Additional help with project design and BLI assay optimization was provided by Livia Shehaj, Jennifer Pace, and Yang Mei.

Chapter 4: Discussion, Significance, and Future Directions

4.1. CPP-Conjugated pTyr Isosteres Targeting the STAT3 SH2 Domain

4.1.1. CPP12 Cell Penetration Conclusions

In the work described in chapter 2, we chose to use CPP12 for the delivery of pTyr isostere-containing STAT3 peptide inhibitors as CPP12 is one of the most cytosolically efficient CPPs reported in the literature to date and has already proven capable of delivering anionic cargo.[74–76,130,131] We chose to assess cytosolic delivery in this work via the chloroalkane penetration assay (CAPA).[126] In doing so, we could more quantitatively assess the cell penetration of our pTyr isostere-containing peptides, and benchmark them against other frequently used cell-penetrating peptide and small molecule controls. We determined by CAPA that CPP12-conjugated pTyr isostere-containing peptides had a CP_{50} of 720 nM. This is impressive degree of cytosolic penetration for a peptide, given our small molecule control (ct-W) exhibited a CP_{50} of 50 nM under these conditions. By comparison, Tat, a commonly used cell-penetrating peptide, exhibited a CP_{50} of 7.74 μM without any anionic cargo attached. Thus, the CPP12-conjugated peptide was delivered to the cytosol more than 10-fold more efficiently than Tat without cargo. Importantly, this cell penetration can be directly attributed to CPP12, as the pTyr-isostere control without CPP12 had a CP_{50} of just 18.9 μM (over 26-fold worse than with CPP12). This demonstrates that, while pTyr isosteres have intrinsically poor cell penetration, CPP12 is an effective method to deliver them to the cytosol.

4.1.2. Affinities of pTyr Isosteres for the STAT3 SH2 Domain

pTyr isosteres such as Pmp and F_2Pmp are known to be tolerated differently by different SH2 domains.[21–23] For STAT3, Dourlat and colleagues showed that incorporating Pmp into the same gp130-derived peptides that we used resulted in a 15-fold loss in inhibition compared to pTyr.[157] In our direct binding fluorescence polarization assay, we observed

over a 100-fold loss in binding affinity with Pmp substitution. The differences seen here may be a result of the differences in techniques used, given we used a direct binding assay and Dourlat and colleagues used a competition assay of STAT3:DNA binding in nuclear lysates.

When we substituted F_2Pmp into the same gp130-derived peptide, we observed a 17-fold loss in binding affinity to STAT3 compared to pTyr. Unfortunately this loss in affinity proved too difficult a barrier to surmount for observing cell-based efficacy, despite evidence of impressive cell penetration. As such, no intracellular phenotypes were observed with peptide treatment, including inhibition of STAT3 transcriptional activity or STAT3-dependent cancer cell viability. Our work was the first to directly substitute F_2Pmp into this gp130-derived peptide sequence, and demonstrated that the STAT3 SH2 domain does not tolerate this substitution well. Mandal and colleagues have employed similar isosteres, utilizing a 4-phosphonodifluoromethylcinnamate in this peptide and several related peptidomimetics, with pivaloyloxymethyl protecting groups to improve penetration.[28,32,129] These peptidomimetics were capable of inhibiting STAT3 phosphorylation in cells at 100 nM concentrations, suggesting that similar SAR strategies, though arduous, may allow for more efficacious SH2 domain inhibitors originating from phosphopeptides.

4.1.3. pTyr and pTyr Isostere Stability

Our work studying the serum and cell lysate stability of select pTyr and pTyr-isostere containing peptides has also provided several important insights with regards to SH2 domain inhibitors. First, our serum stability results demonstrate that even in 10% FBS in DMEM, considerable dephosphorylation occurs for phosphopeptides. This limits their efficacy, even in cell culture. Further, in cell lysates, phosphopeptides are even more rapidly dephosphorylated. Interestingly, upon dephosphorylation, there appear to be

numerous new proteolytic cleavage products formed that do not exist for F_2Pmp substituted peptides, which cannot undergo dephosphorylation. This suggests that the pTyr residue can protect against proteolysis and so substitution with pTyr isosteres such as F_2Pmp not only prevent phosphate hydrolysis, but also confer significant protection from proteolytic activity.

We also observed that peptides with F_2Pmp substitution still had a solitary cleavage product at the glutamine residue after 24 hours in cell lysate. Replacing this glutamine with an N-methylglutamine conferred complete resistance to proteolytic degradation over 24 hours in cell lysate. This work highlights that while phosphopeptides are intrinsically vulnerable to degradation both in serum and in cells, a very limited number of substitutions can promote stability, thus improving upon the pharmacological properties of these biomolecules.

4.1.4. Significance and Future Directions

Though our explorations of STAT3 inhibitors did not result in peptides capable of inhibiting STAT3 transcriptional activity in cells, it did highlight multiple lessons that can shape future SH2 domain inhibitor development. This work suggests that more recently developed cell penetrating peptides, such as CPP12, can be highly efficient at delivering anionic peptides. Future work aimed at delivering anionic or polyanionic peptide inhibitors of SH2 domains and PTPs should certainly consider using CPP12 to deliver them to their cytosolic targets. Further, CPP12 itself proved to be completely stable in cell lysate over 24 hours. Our evidence suggests this to be a much more efficient delivery than could be achieved with Tat, and likely other linear CPPs.

Additionally, this work has demonstrated that the F_2Pmp substitution does not promote improved STAT3 binding, at least in the context of the gp130-derived peptide sequence. Our inhibitor had IC_{50} values in STAT3 competition FP assays that were similar to small

molecule STAT3 inhibitors which demonstrated intracellular phenotypes.[37,38] However, despite effective cell penetration as assessed by CAPA, this CP_{50} of 720 nM is still an order of magnitude greater than our small molecule controls (50 nM), suggesting that this degree of affinity may be sufficient for small molecule inhibitors, but is insufficient for even a highly cell-penetrant peptide. We anticipate this strategy may work better for SH2 domains or PTPs for which F_2Pmp substitution improves affinity of a peptide substrate.

For STAT3 SH2 domain inhibitors, higher throughput methodologies may still provide solutions to some of the hurdles mentioned above. For example, Lian and colleagues utilized a one-bead-one-compound (OBOC) peptide library incorporating F_2Pmp for the discovery of a high affinity, selective bicyclic peptide inhibitor of PTP1B.[73] Utilizing peptide libraries incorporating F_2Pmp opens up the possibilities of identifying new peptide sequences capable of synergizing with the pTyr isostere, rather than trying to replace pTyr from available STAT3-targeted phosphopeptide sequences. This library approach could similarly be undertaken while incorporating a number of other pTyr isosteres, including carboxy phenylalanine, carboxymethyl phenylalanine, O-malonyl tyrosine, and fluoro-O-malonyl tyrosine. While these pTyr isosteres would have served as lower-affinity starting points in the rational design efforts described in chapter 2, they would be more likely to capture synergies with novel peptide sequences that would not have been predicted from simple structure-activity relationships.

Importantly, use of combinatorial peptide library approaches would require extra caution for assessing not just affinity, but selectivity of these inhibitors, as STAT3 and the proapoptotic STAT1 share considerable sequence homology while having opposing effects on tumorigenesis. As such, negative screens could be employed to remove peptide sequences that bind to STAT1 protein, before proceeding to screens that select for STAT3 binders.

Taken together, there are still numerous ways in which pTyr isosteres like F_2Pmp could be further employed to target the STAT3 SH2 domain, and other SH2 domains and PTPs. The medicinal chemistry of SH2 domain inhibitors has been ongoing for several decades and has faced numerous challenges. Lessons learned in this work should prove useful in the continued development of SH2 domain inhibitors for STAT3 and other disease-relevant proteins.

4.2. LC3B-targeted LIR Motif Peptides

4.2.1. Insights from SAR Studies

In our work studying the FYCO1 LIR motif and its interactions with LC3B, we have uncovered structure-activity relationships that will inform LC3B inhibitor development. To begin, we further validated that FYCO1-derived LIR motif peptides are selective for LC3B over GABARAP, a finding shared by numerous other research groups through a variety of binding techniques.[104,116–118] The preferential binding of LC3s over GABARAPs is a fairly unique feature of FYCO1, and positions FYCO1 LIR-derived peptides to be the most promising starting points for developing LC3B-selective inhibitor peptides.

Additionally, this work showed that residues N-terminal to the core LIR motif are critical for LC3B binding, but the negatively charged side chains are not solely responsible for this affinity. This was supported by the observation that mutating both N-terminal aspartates to asparagines resulted in a 4-fold loss in LC3B binding affinity, while N-terminal truncation completely abrogated binding. C-terminal truncation, on the other hand, did not completely disrupt binding, though it did lead to a 10-fold loss in affinity. When only Q1292 and E1293 were removed from the C-terminus, it had little impact. This work has also highlighted several additional negatively charged residues, including D1285 and E1293, have minimal contributions to binding and could be removed in future efforts to make more cell-penetrant peptides.

In focusing on the improvement of FYCO1-derived LIR motif peptides, we learned that not only can the HP1 hydrophobic pocket accommodate 1- and 2-naphthylalanine in place of natural aromatic side chains (W/F/Y), but there is in fact a preference for them. HP2 proved less tolerable to substitutions of phenylalanine and 2-naphthylalanine, suggesting residues larger than its typical binding partners (I/L/V) cannot be applied. Several additional substitutions improved affinity, such as incorporation of an N-terminal arginine (hypothesized to interact with nearby D46 on the LC3B surface) and mutating L1288 to a *tert*-butyl alanine.

Additionally, an important but unexpected finding was that, while peptide stapling led to poorer binding affinities, one staple exhibited synergy with other favorable substitutions resulting in binding affinity similar to the parent FYCO1 peptide. This observation demonstrates just how much impact conformational constraint can have on peptide binding. This finding in particular suggests that more study into stapled LIR peptides, either through rational design approaches or through high throughput combinatorial approaches, could discover even more potent LC3B inhibitors.

4.2.2. Selectivity and Stability of Optimized LC3B Inhibitors

In the work described in chapter 3, we generated two optimized LC3B-targeting peptides, one linear and one stapled. The optimized stapled peptide (Comb2) had a 2-fold improvement in lysate stability over 24 hours. Meanwhile, the artificial amino acid substitutions in the optimized linear peptide did not confer any protection against degradation. These data suggest that further optimization of the staple, for instance by stapling different positions of the peptides, may not only improve affinity but also stability.

As discussed in section 1.2.3. there is considerable evidence to suggest that selectivity for LC3B over other ATG8 paralogs could provide efficacy as an anticancer agent.[110–112]

Thus, maintaining the selectivity of the FYCO1 LIR motif for LC3s over GABARAPs was an important feature for optimized LIR peptides. Both the linear and stapled optimized peptides maintained over 5-fold selectivity for LC3B over GABARAP when measured by BLI, comparable to the native FYCO1 LIR motif. Overall, this work has generated the most high-affinity LIR peptides that maintain selectivity for LC3s over GABARAPs. Recent evidence by Wirth and colleagues has suggested that C-terminal helices help to dictate selectivity of LIR motifs.[115] As such, it is possible that broader mutational scanning of these C-terminal residues may offer substitutions that not only maintain, but improve LC3B selectivity.

4.2.3. Significance and Future Directions

Ultimately, this work has highlighted a number of important features for LIR peptide:LC3B binding. Future efforts to inhibit LC3B selectively with more cell-penetrant, stable peptide inhibitors can take multiple lessons from these efforts. This includes the removal of multiple negative charges with limited affinity contribution (D1276, D12777, D1285, and E1293) as well as shortening both the N- and C-termini by several residues for shorter peptides.

Further, peptide affinity can be improved through the incorporation of 2-naphthylalanine to target the HP1 pocket. Binding affinity to HP1 could be further improved by testing a larger panel of F/Y/W derivatives, as only 1- and 2-naphthylalanine were tested in this work. Similarly, binding affinity to HP2 could be further improved with smaller artificial residues similar in size to native binding substrates (L/I/V).

A much larger study of peptide stapling could be undertaken to produce even more stable, high-affinity LC3B peptides. This work tested stapling at a few select positions, and yet still was able to identify a staple that synergized with other favorable substitutions and improved stability 2-fold. There remains considerable potential in

continuing diversity-oriented stapling efforts of LIR motif peptides. Further testing of peptides that are stapled in different positions, especially in the context of other favorable mutations, may maximize affinity and synergistic effects for selective LIR peptides. For a more thorough sampling of possible sequences and staples, a one-bead-one-compound peptide library may prove useful. This approach could allow for a more complete picture of where to staple LIR peptides, while also trying out multiple combinations of canonical and artificial residues at various positions.

We anticipate that, despite the optimization of affinity and stability, these LIR peptides may still exhibit poor cell penetration. This would make them unsuitable for cancer studies. As such, a next step could be to conjugate CPPs such as CPP12 to the optimized LIR peptides to better deliver them to the cytosol. As our work has already demonstrated the ability of CPP12 to deliver anionic peptides (chapter 2), this should provide a reasonable strategy for overcoming issues of cell penetration. Further, we could employ CAPA to more quantitatively characterize the cell penetration of our CPP12-LIR conjugates. Generating many analogs of CPP12-LIR conjugates, for instance incorporating and excluding different negatively charged residues, could give an even more detailed picture of the tradeoffs in affinity and permeability for individual glutamate and aspartate residues.

Ultimately, the most cell-penetrant, high-affinity peptides should be tested in cell-based assays to assess autophagy inhibition. This could include looking at typical markers of autophagy modulation such as LC3-I/LC3-II levels and p62 levels by immunoblotting, or quantifying the number of autophagosomes with a GFP-LC3 cell line.[132,158] If these peptides inhibited autophagy in cell culture, this would validate their use in additional studies looking at autophagy inhibition in cancer. For example, they could be used in combination studies with and without chemotherapies in cancer cell lines like

glioblastoma, hepatocellular carcinoma, and others that have already shown benefit from autophagy inhibition.[87–91] Ultimately, there is a great deal more to be done with LIR motif peptides derived from FYCO1 as well as peptides derived from other LIRs for the development of more useful autophagy inhibitors. As an initial exploration of FYCO1-LC3B structure-activity relationships, this work has important insights to help in effort, which will ultimately benefit research into autophagy and cancer.

Bibliography

(1) Johnson, D. E.; O'Keefe, R. A.; Grandis, J. R. Targeting the IL-6/JAK/STAT3 Signalling Axis in Cancer. *Nature Reviews Clinical Oncology* **2018**, *15* (4), 234–248. https://doi.org/10.1038/nrclinonc.2018.8.

(2) Yu, H.; Lee, H.; Herrmann, A.; Buettner, R.; Jove, R. Revisiting STAT3 Signalling in Cancer: New and Unexpected Biological Functions. *Nature Reviews Cancer* **2014**, *14* (11), 736–746. https://doi.org/10.1038/nrc3818.

(3) Wei, D.; Le, X.; Zheng, L.; Wang, L.; Frey, J. A.; Gao, A. C.; Peng, Z.; Huang, S.; Xiong, H. Q.; Abbruzzese, J. L.; Xie, K. Stat3 Activation Regulates the Expression of Vascular Endothelial Growth Factor and Human Pancreatic Cancer Angiogenesis and Metastasis. *Oncogene* **2003**, *22* (3), 319–329. https://doi.org/10.1038/sj.onc.1206122.

(4) Xie, T.; Wei, D.; Liu, M.; Gao, A. C.; Ali-Osman, F.; Sawaya, R.; Huang, S. Stat3 Activation Regulates the Expression of Matrix Metalloproteinase-2 and Tumor Invasion and Metastasis. *Oncogene* **2004**, *23* (20), 3550–3560. https://doi.org/10.1038/sj.onc.1207383.

(5) Gritsko, T. Persistent Activation of Stat3 Signaling Induces Survivin Gene Expression and Confers Resistance to Apoptosis in Human Breast Cancer Cells. *Clinical Cancer Research* **2006**, *12* (1), 11–19. https://doi.org/10.1158/1078-0432.CCR-04-1752.

(6) Lee, T.-L.; Yeh, J.; Waes, C. V.; Chen, Z. Bcl-XL Is Regulated by NF-KappaB and STAT3 through P53-Dependent Control in Head and Neck Squamous Cell Carcinoma. *Cancer Res* **2004**, *64* (7 Supplement), 1115–1115.

(7) Schlessinger, K.; Levy, D. E. Malignant Transformation but Not Normal Cell Growth Depends on Signal Transducer and Activator of Transcription 3. *Cancer Res* **2005**, *65* (13), 5828–5834. https://doi.org/10.1158/0008-5472.CAN-05-0317.

(8) Bu, L. L.; Yu, G. T.; Wu, L.; Mao, L.; Deng, W. W.; Liu, J. F.; Kulkarni, A. B.; Zhang, W. F.; Zhang, L.; Sun, Z. J. STAT3 Induces Immunosuppression by Upregulating PD-1/PD-L1 in HNSCC. *Journal of Dental Research* **2017**, *96* (9), 1027–1034. https://doi.org/10.1177/0022034517712435.

(9) Kitamura, H.; Ohno, Y.; Toyoshima, Y.; Ohtake, J.; Homma, S.; Kawamura, H.; Takahashi, N.; Taketomi, A. Interleukin-6/STAT3 Signaling as a Promising Target to Improve the Efficacy of Cancer Immunotherapy. *Cancer Sci.* **2017**, *108* (10), 1947–1952. https://doi.org/10.1111/cas.13332.

(10) Frank, D. A. STAT3 as a Central Mediator of Neoplastic Cellular Transformation. *Cancer Lett.* **2007**, *251* (2), 199–210. https://doi.org/10.1016/j.canlet.2006.10.017.

(11) Sadowski, I.; Stone, J. C.; Pawson, T. A Noncatalytic Domain Conserved among Cytoplasmic Protein-Tyrosine Kinases Modifies the Kinase Function and Transforming Activity of Fujinami Sarcoma Virus P130gag-Fps. *Molecular and Cellular Biology* **1986**, *6* (12), 4396–4408. https://doi.org/10.1128/MCB.6.12.4396.

(12) Koch, C. A.; Anderson, D.; Moran, M. F.; Ellis, C.; Pawson, T. SH2 and SH3 Domains: Elements That Control Interactions of Cytoplasmic Signaling Proteins. *Science* **1991**, *252* (5006), 668–674. https://doi.org/10.1126/science.1708916.

(13) Kraskouskaya, D.; Duodu, E.; Arpin, C. C.; Gunning, P. T. Progress towards the Development of SH2 Domain Inhibitors. *Chem. Soc. Rev.* **2013**, *42* (8), 3337–3370. https://doi.org/10.1039/C3CS35449K.

(14) Pawson, T.; Nash, P. Assembly of Cell Regulatory Systems Through Protein Interaction Domains. *Science* **2003**, *300* (5618), 445–452. https://doi.org/10.1126/science.1083653.

(15) Waksman, G.; Kominos, D.; Robertson, S. C.; Pant, N.; Baltimore, D.; Birge, R. B.; Cowburn, D.; Hanafusa, H.; Mayer, B. J.; Overduin, M.; Resh, M. D.; Rios, C. B.; Silverman, L.; Kuriyan, J. Crystal Structure of the Phosphotyrosine Recognition Domain SH2 of V- Src Complexed with Tyrosine-Phosphorylated Peptides. *Nature* **1992**, *358* (6388), 646. https://doi.org/10.1038/358646a0.

(16) Waksman, G.; Shoelson, S.; Pant, N.; Cowburn, D.; Kuriyan, J. Binding of a High-Affinity Phosphotyrosyl Peptide to the Src Sh2 Domain - Crystal-Structures of the Complexed and Peptide-Free Forms. *Cell* **1993**, *72* (5), 779–790. https://doi.org/10.1016/0092-8674(93)90405-F.

(17) Zhou, S.; Shoelson, S. E.; Chaudhuri, M.; Gish, G.; Pawson, T.; Haser, W. G.; King, F.; Roberts, T.; Ratnofsky, S.; Lechleider, R. J.; Neel, B. G.; Birge, R. B.; Fajardo, J. E.; Chou, M. M.; Hanafusa, H.; Schaffhausen, B.; Cantley, L. C. SH2 Domains Recognize Specific Phosphopeptide Sequences. *Cell* **1993**, *72* (5), 767–778. https://doi.org/10.1016/0092-8674(93)90404-E.

(18) Bai, L.; Zhou, H.; Xu, R.; Zhao, Y.; Chinnaswamy, K.; McEachern, D.; Chen, J.; Yang, C.-Y.; Liu, Z.; Wang, M.; Liu, L.; Jiang, H.; Wen, B.; Kumar, P.; Meagher, J. L.; Sun, D.; Stuckey, J. A.; Wang, S. A Potent and Selective Small-Molecule Degrader of STAT3 Achieves Complete Tumor Regression In Vivo. *Cancer Cell* **2019**, *36* (5), 498-511.e17. https://doi.org/10.1016/j.ccell.2019.10.002.

(19) Cerulli, R. A.; Kritzer, J. A. Phosphotyrosine Isosteres: Past, Present and Future. *Org. Biomol. Chem.* **2019**. https://doi.org/10.1039/C9OB01998G.

(20) Domchek, S. M.; Auger, K. R.; Chatterjee, S.; Burke, T. R.; Shoelson, S. E. Inhibition of SH2 Domain/Phosphoprotein Association by a Nonhydrolyzable Phosphonopeptide. *Biochemistry* **1992**, *31* (41), 9865–9870.

(21) Burke, T. R.; Smyth, M. S.; Nomizu, M.; Otaka, A.; Roller, P. R. Preparation of Fluoro- and Hydroxy-4-(Phosphonomethyl)-D,L-Phenylalanine Suitably Protected for Solid-Phase Synthesis of Peptides Containing Hydrolytically Stable Analogs of O-Phosphotyrosine. *The Journal of Organic Chemistry* **1993**, *58* (6), 1336–1340. https://doi.org/10.1021/jo00058a009.

(22) Burke, T. R.; Kole, H. K.; Roller, P. P. Potent Inhibition of Insulin Receptor Dephosphorylation by a Hexamer Peptide Containing the Phosphotyrosyl Mimetic F2Pmp. *Biochemical and Biophysical Research Communications* **1994**, *204* (1), 129–134. https://doi.org/10.1006/bbrc.1994.2435.

(23) Burke, T. R. Jr.; Smyth, M. S.; Otaka, A.; Nomizu, M.; Roller, P. P.; Wolf, G.; Case, R.; Shoelson, S. E. Nonhydrolyzable Phosphotyrosyl Mimetics for the Preparation Of Phosphatase-Resistant SH2 Domain Inhibitors. *Biochemistry* **1994**, *33* (21), 6490–6494. https://doi.org/10.1021/bi00187a015.

(24) Shen, K.; Keng, Y.-F.; Wu, L.; Guo, X.-L.; Lawrence, D. S.; Zhang, Z.-Y. Acquisition of a Specific and Potent PTP1B Inhibitor from a Novel Combinatorial Library and Screening Procedure. *Journal of Biological Chemistry* **2001**, *276* (50), 47311–47319. https://doi.org/10.1074/jbc.M106568200.

(25) Patel, D.; Jain, M.; Shah, S. R.; Bahekar, R.; Jadav, P.; Joharapurkar, A.; Dhanesha, N.; Shaikh, M.; Sairam, K. V. V. M.; Kapadnis, P. Discovery of Potent, Selective and Orally Bioavailable Triaryl-Sulfonamide Based PTP1B Inhibitors. *Bioorganic & Medicinal Chemistry Letters* **2012**, *22* (2), 1111–1117. https://doi.org/10.1016/j.bmcl.2011.11.122.

(26) Dufresne, C.; Roy, P.; Wang, Z.; Asante-Appiah, E.; Cromlish, W.; Boie, Y.; Forghani, F.; Desmarais, S.; Wang, Q.; Skorey, K.; Waddleton, D.; Ramachandran, C.; Kennedy, B. P.; Xu, L.; Gordon, R.; Chan, C. C.; Leblanc, Y. The Development of Potent Non-Peptidic PTP-

1B Inhibitors. *Bioorganic & Medicinal Chemistry Letters* **2004**, *14* (4), 1039–1042. https://doi.org/10.1016/j.bmcl.2003.11.048.

(27) Li, X.; Bhandari, A.; Holmes, C. P.; Szardenings, A. K. α,α-Difluoro-β-Ketophosphonates as Potent Inhibitors of Protein Tyrosine Phosphatase 1B. *Bioorganic & Medicinal Chemistry Letters* **2004**, *14* (16), 4301–4306. https://doi.org/10.1016/j.bmcl.2004.05.082.

(28) Mandal, P. K.; Liao, W. S.-L.; McMurray, J. S. Synthesis of Phosphatase-Stable, Cell-Permeable Peptidomimetic Prodrugs That Target the SH2 Domain of Stat3. *Organic Letters* **2009**, *11* (15), 3394–3397. https://doi.org/10.1021/ol9012662.

(29) Mandal, P. K.; Gao, F.; Lu, Z.; Ren, Z.; Ramesh, R.; Birtwistle, J. S.; Kaluarachchi, K. K.; Chen, X.; Bast, R. C.; Liao, W. S.; McMurray, J. S. Potent and Selective Phosphopeptide Mimetic Prodrugs Targeted to the Src Homology 2 (SH2) Domain of Signal Transducer and Activator of Transcription 3. *Journal of Medicinal Chemistry* **2011**, *54* (10), 3549–3563. https://doi.org/10.1021/jm2000882.

(30) McMurray, J. S.; Mandal, P. K.; Liao, W. S.; Klostergaard, J.; Robertson, F. M. The Consequences of Selective Inhibition of Signal Transducer and Activator of Transcription 3 (STAT3) Tyrosine705 Phosphorylation by Phosphopeptide Mimetic Prodrugs Targeting the Src Homology 2 (SH2) Domain. *Jak-Stat* **2012**, *1* (4), 263–347. https://doi.org/10.4161/jkst.22682.

(31) Auzenne, E. J.; Klostergaard, J.; Mandal, P. K.; Liao, W. S.; Lu, Z.; Gao, F.; Bast, R. C. J.; Robertson, F. M.; McMurray, J. S. A Phosphopeptide Mimetic Prodrug Targeting the SH2 Domain of Stat3 Inhibits Tumor Growth and Angiogenesis. *Journal of experimental therapeutics & oncology* **2012**, *10* (2), 155–162.

(32) Mandal, P. K.; Morlacchi, P.; Knight, J. M.; Link, T. M.; Lee, G. R.; Nurieva, R.; Singh, D.; Dhanik, A.; Kavraki, L.; Corry, D. B.; Ladbury, J. E.; McMurray, J. S. Targeting the Src Homology 2 (SH2) Domain of Signal Transducer and Activator of Transcription 6 (STAT6) with Cell-Permeable, Phosphatase-Stable Phosphopeptide Mimics Potently Inhibits Tyr641 Phosphorylation and Transcriptional Activity. *Journal of Medicinal Chemistry* **2015**, *58* (22), 8970–8984. https://doi.org/10.1021/acs.jmedchem.5b01321.

(33) Neklesa, T. K.; Winkler, J. D.; Crews, C. M. Targeted Protein Degradation by PROTACs. *Pharmacol. Ther.* **2017**, *174*, 138–144. https://doi.org/10.1016/j.pharmthera.2017.02.027.

(34) Siddiquee, K.; Zhang, S.; Guida, W. C.; Blaskovich, M. A.; Greedy, B.; Lawrence, H. R.; Yip, M. L. R.; Jove, R.; McLaughlin, M. M.; Lawrence, N. J.; Sebti, S. M.; Turkson, J. Selective Chemical Probe Inhibitor of Stat3, Identified through Structure-Based Virtual Screening, Induces Antitumor Activity. *Proceedings of the National Academy of Sciences* **2007**, *104* (18), 7391–7396. https://doi.org/10.1073/pnas.0609757104.

(35) Fletcher, S.; Singh, J.; Zhang, X.; Yue, P.; Page, B. D. G.; Sharmeen, S.; Shahani, V. M.; Zhao, W.; Schimmer, A. D.; Turkson, J.; Gunning, P. T. Disruption of Transcriptionally Active Stat3 Dimers with Non-Phosphorylated, Salicylic Acid-Based Small Molecules: Potent in Vitro and Tumor Cell Activities. *ChemBioChem* **2009**, *10* (12), 1959–1964. https://doi.org/10.1002/cbic.200900172.

(36) Zhang, X.; Yue, P.; Fletcher, S.; Zhao, W.; Gunning, P. T.; Turkson, J. A Novel Small-Molecule Disrupts Stat3 SH2 Domain–Phosphotyrosine Interactions and Stat3-Dependent Tumor Processes. *Biochemical Pharmacology* **2010**, *79* (10), 1398–1409. https://doi.org/10.1016/j.bcp.2010.01.001.

(37) Zhang, X.; Yue, P.; Page, B. D. G.; Li, T.; Zhao, W.; Namanja, A. T.; Paladino, D.; Zhao, J.; Chen, Y.; Gunning, P. T.; Turkson, J. Orally Bioavailable Small-Molecule Inhibitor of

Transcription Factor Stat3 Regresses Human Breast and Lung Cancer Xenografts. *Proceedings of the National Academy of Sciences* **2012**, *109* (24), 9623–9628. https://doi.org/10.1073/pnas.1121606109.

(38) Haftchenary, S.; Luchman, H. A.; Jouk, A. O.; Veloso, A. J.; Page, B. D. G.; Cheng, X. R.; Dawson, S. S.; Grinshtein, N.; Shahani, V. M.; Kerman, K.; Kaplan, D. R.; Griffin, C.; Aman, A. M.; Al-awar, R.; Weiss, S.; Gunning, P. T. Potent Targeting of the STAT3 Protein in Brain Cancer Stem Cells: A Promising Route for Treating Glioblastoma. *ACS Medicinal Chemistry Letters* **2013**, *4* (11), 1102–1107. https://doi.org/10.1021/ml4003138.

(39) Arpin, C. C.; Mac, S.; Jiang, Y.; Cheng, H.; Grimard, M.; Page, B. D. G.; Kamocka, M. M.; Haftchenary, S.; Su, H.; Ball, D. P.; Rosa, D. A.; Lai, P.-S.; Gomez-Biagi, R. F.; Ali, A. M.; Rana, R.; Hanenberg, H.; Kerman, K.; McElyea, K. C.; Sandusky, G. E.; Gunning, P. T.; Fishel, M. L. Applying Small Molecule Signal Transducer and Activator of Transcription-3 (STAT3) Protein Inhibitors as Pancreatic Cancer Therapeutics. *Molecular Cancer Therapeutics* **2016**, *15* (5), 794–805. https://doi.org/10.1158/1535-7163.MCT-15-0003.

(40) Song, H.; Wang, R.; Wang, S.; Lin, J. A Low-Molecular-Weight Compound Discovered through Virtual Database Screening Inhibits Stat3 Function in Breast Cancer Cells. *PNAS* **2005**, *102* (13), 4700–4705. https://doi.org/10.1073/pnas.0409894102.

(41) Chen, C.-L.; Loy, A.; Cen, L.; Chan, C.; Hsieh, F.-C.; Cheng, G.; Wu, B.; Qualman, S. J.; Kunisada, K.; Yamauchi-Takihara, K.; Lin, J. Signal Transducer and Activator of Transcription 3 Is Involved in Cell Growth and Survival of Human Rhabdomyosarcoma and Osteosarcoma Cells. *BMC Cancer* **2007**, *7* (111).

(42) Chen, C.-L.; Cen, L.; Kohout, J.; Hutzen, B.; Chan, C.; Hsieh, F.-C.; Loy, A.; Huang, V.; Cheng, G.; Lin, J. Signal Transducer and Activator of Transcription 3 Activation Is Associated with Bladder Cancer Cell Growth and Survival. *Molecular Cancer* **2008**, *7* (78). https://doi.org/10.1186/1476-4598-7-78.

(43) Lin, L.; Hutzen, B.; Li, P.-K.; Ball, S.; Zuo, M.; DeAngelis, S.; Foust, E.; Sobo, M.; Friedman, L.; Bhasin, D.; Cen, L.; Li, C.; Lin, J. A Novel Small Molecule, LLL12, Inhibits STAT3 Phosphorylation and Activities and Exhibits Potent Growth-Suppressive Activity in Human Cancer Cells. *Neoplasia* **2010**, *12* (1), 39–50. https://doi.org/10.1593/neo.91196.

(44) Zuo, M.; Li, C.; Lin, J.; Javle, M. LLL12, a Novel Small Inhibitor Targeting STAT3 for Hepatocellular Carcinoma Therapy. *Oncotarget* **2015**, *6* (13), 10940–10949. https://doi.org/10.18632/oncotarget.3458.

(45) Ball, S.; Li, C.; Li, P.-K.; Lin, J. The Small Molecule, LLL12, Inhibits STAT3 Phosphorylation and Induces Apoptosis in Medulloblastoma and Glioblastoma Cells. *PLoS ONE* **2011**, *6* (4), e18820. https://doi.org/10.1371/journal.pone.0018820.

(46) Liu, A.; Liu, Y.; Li, P.-K.; Li, C.; Lin, J. LLL12 Inhibits Endogenous and Exogenous Interleukin-6-Induced STAT3 Phosphorylation in Human Pancreatic Cancer Cells. *Anticancer Research* **2011**, *31*, 2029–2036.

(47) Lin, L.; Benson, D. M.; DeAngelis, S.; Bakan, C. E.; Li, P.-K.; Li, C.; Lin, J. A Small Molecule, LLL12 Inhibits Constitutive STAT3 and IL-6-Induced STAT3 Signaling and Exhibits Potent Growth Suppressive Activity in Human Multiple Myeloma Cells. *International Journal of Cancer* **2012**, *130* (6), 1459–1469. https://doi.org/10.1002/ijc.26152.

(48) Yu, W.; Li, C.; Zhang, W.; Xia, Y.; Li, S.; Lin, J.; Yu, K.; Liu, M.; Yang, L.; Luo, J.; Chen, Y.; Sun, H.; Kong, L. Discovery of an Orally Selective Inhibitor of Signal Transducer and Activator of Transcription 3 Using Advanced Multiple Ligand Simultaneous Docking. *Journal of Medicinal Chemistry* **2017**, *60* (7), 2718–2731. https://doi.org/10.1021/acs.jmedchem.6b01489.

(49) Xu, X.; Kasembeli, M. M.; Jiang, X.; Tweardy, B. J.; Tweardy, D. J. Chemical Probes That Competitively and Selectively Inhibit Stat3 Activation. *PLoS ONE* **2009**, *4* (3), e4783. https://doi.org/10.1371/journal.pone.0004783.

(50) Dave, B.; Landis, M. D.; Dobrolecki, L. E.; Wu, M.-F.; Zhang, X.; Westbrook, T. F.; Hilsenbeck, S. G.; Liu, D.; Lewis, M. T.; Tweardy, D. J.; Chang, J. C. Selective Small Molecule Stat3 Inhibitor Reduces Breast Cancer Tumor-Initiating Cells and Improves Recurrence Free Survival in a Human-Xenograft Model. *PLoS ONE* **2012**, *7* (8), e30207. https://doi.org/10.1371/journal.pone.0030207.

(51) Bharadwaj, U.; Eckols, T. K.; Xu, X.; Kasembeli, M. M.; Chen, Y.; Adachi, M.; Song, Y.; Mo, Q.; Lai, S. Y.; Tweardy, D. J. Small-Molecule Inhibition of STAT3 in Radioresistant Head and Neck Squamous Cell Carcinoma. *Oncotarget* **2016**, *7* (18), 26307–26330. https://doi.org/10.18632/oncotarget.8368.

(52) Miyoshi, K.; Takaishi, M.; Nakajima, K.; Ikeda, M.; Kanda, T.; Tarutani, M.; Iiyama, T.; Asao, N.; DiGiovanni, J.; Sano, S. Stat3 as a Therapeutic Target for the Treatment of Psoriasis: A Clinical Feasibility Study with STA-21, a Stat3 Inhibitor. *J. Invest. Dermatol.* **2011**, *131* (1), 108–117. https://doi.org/10.1038/jid.2010.255.

(53) Wong, A. L.; Soo, R. A.; Tan, D. S.; Lee, S. C.; Lim, J. S.; Marban, P. C.; Kong, L. R.; Lee, Y. J.; Wang, L. Z.; Thuya, W. L.; Soong, R.; Yee, M. Q.; Chin, T. M.; Cordero, M. T.; Asuncion, B. R.; Pang, B.; Pervaiz, S.; Hirpara, J. L.; Sinha, A.; Xu, W. W.; Yuasa, M.; Tsunoda, T.; Motoyama, M.; Yamauchi, T.; Goh, B. C. Phase I and Biomarker Study of OPB-51602, a Novel Signal Transducer and Activator of Transcription (STAT) 3 Inhibitor, in Patients with Refractory Solid Malignancies. *Ann. Oncol.* **2015**, *26* (5), 998–1005. https://doi.org/10.1093/annonc/mdv026.

(54) Ogura, M.; Uchida, T.; Terui, Y.; Hayakawa, F.; Kobayashi, Y.; Taniwaki, M.; Takamatsu, Y.; Naoe, T.; Tobinai, K.; Munakata, W.; Yamauchi, T.; Kageyama, A.; Yuasa, M.; Motoyama, M.; Tsunoda, T.; Hatake, K. Phase I Study of OPB-51602, an Oral Inhibitor of Signal Transducer and Activator of Transcription 3, in Patients with Relapsed/Refractory Hematological Malignancies. *Cancer Sci.* **2015**, *106* (7), 896–901. https://doi.org/10.1111/cas.12683.

(55) Oh, D.-Y.; Lee, S.-H.; Han, S.-W.; Kim, M.-J.; Kim, T.-M.; Kim, T.-Y.; Heo, D. S.; Yuasa, M.; Yanagihara, Y.; Bang, Y.-J. Phase I Study of OPB-31121, an Oral STAT3 Inhibitor, in Patients with Advanced Solid Tumors. *Cancer Res Treat* **2015**, *47* (4), 607–615. https://doi.org/10.4143/crt.2014.249.

(56) Bendell, J. C.; Hong, D. S.; Burris, H. A.; Naing, A.; Jones, S. F.; Falchook, G.; Bricmont, P.; Elekes, A.; Rock, E. P.; Kurzrock, R. Phase 1, Open-Label, Dose-Escalation, and Pharmacokinetic Study of STAT3 Inhibitor OPB-31121 in Subjects with Advanced Solid Tumors. *Cancer Chemother. Pharmacol.* **2014**, *74* (1), 125–130. https://doi.org/10.1007/s00280-014-2480-2.

(57) Okusaka, T.; Ueno, H.; Ikeda, M.; Mitsunaga, S.; Ozaka, M.; Ishii, H.; Yokosuka, O.; Ooka, Y.; Yoshimoto, R.; Yanagihara, Y.; Okita, K. Phase 1 and Pharmacological Trial of OPB-31121, a Signal Transducer and Activator of Transcription-3 Inhibitor, in Patients with Advanced Hepatocellular Carcinoma. *Hepatol. Res.* **2015**, *45* (13), 1283–1291. https://doi.org/10.1111/hepr.12504.

(58) Tolcher, A.; Flaherty, K.; Shapiro, G. I.; Berlin, J.; Witzig, T.; Habermann, T.; Bullock, A.; Rock, E.; Elekes, A.; Lin, C.; Kostic, D.; Ohi, N.; Rasco, D.; Papadopoulos, K. P.; Patnaik, A.; Smith, L.; Cote, G. M. A First-in-Human Phase I Study of OPB-111077, a Small-Molecule STAT3 and Oxidative Phosphorylation Inhibitor, in Patients with Advanced Cancers. *Oncologist* **2018**, *23* (6), 658-e72. https://doi.org/10.1634/theoncologist.2017-0325.

(59) Yoo, C.; Kang, J.; Lim, H. Y.; Kim, J. H.; Lee, M.-A.; Lee, K.-H.; Kim, T.-Y.; Ryoo, B.-Y. Phase I Dose-Finding Study of OPB-111077, a Novel STAT3 Inhibitor, in Patients with Advanced Hepatocellular Carcinoma. *Cancer Res Treat* **2019**, *51* (2), 510–518. https://doi.org/10.4143/crt.2018.226.

(60) Shastri, A.; Choudhary, G.; Teixeira, M.; Gordon-Mitchell, S.; Ramachandra, N.; Bernard, L.; Bhattacharyya, S.; Lopez, R.; Pradhan, K.; Giricz, O.; Ravipati, G.; Wong, L.-F.; Cole, S.; Bhagat, T. D.; Feld, J.; Dhar, Y.; Bartenstein, M.; Thiruthuvanathan, V. J.; Wickrema, A.; Ye, B. H.; Frank, D. A.; Pellagatti, A.; Boultwood, J.; Zhou, T.; Kim, Y.; MacLeod, A. R.; Epling-Burnette, P. K.; Ye, M.; McCoon, P.; Woessner, R.; Steidl, U.; Will, B.; Verma, A. Antisense STAT3 Inhibitor Decreases Viability of Myelodysplastic and Leukemic Stem Cells. *J. Clin. Invest.* **2018**, *128* (12), 5479–5488. https://doi.org/10.1172/JCI120156.

(61) Odate, S.; Veschi, V.; Yan, S.; Lam, N.; Woessner, R.; Thiele, C. J. Inhibition of STAT3 with the Generation 2.5 Antisense Oligonucleotide, AZD9150, Decreases Neuroblastoma Tumorigenicity and Increases Chemosensitivity. *Clin. Cancer Res.* **2017**, *23* (7), 1771–1784. https://doi.org/10.1158/1078-0432.CCR-16-1317.

(62) Hong, D.; Kurzrock, R.; Kim, Y.; Woessner, R.; Younes, A.; Nemunaitis, J.; Fowler, N.; Zhou, T.; Schmidt, J.; Jo, M.; Lee, S. J.; Yamashita, M.; Hughes, S. G.; Fayad, L.; Piha-Paul, S.; Nadella, M. V.; Mohseni, M.; Lawson, D.; Reimer, C.; Blakey, D. C.; Xiao, X.; Hsu, J.; Revenko, A.; Monia, B. P.; MacLeod, A. R. AZD9150, a Next-Generation Antisense Oligonucleotide Inhibitor of STAT3 with Early Evidence of Clinical Activity in Lymphoma and Lung Cancer. *Sci Transl Med* **2015**, *7* (314), 314ra185. https://doi.org/10.1126/scitranslmed.aac5272.

(63) Reilley, M. J.; McCoon, P.; Cook, C.; Lyne, P.; Kurzrock, R.; Kim, Y.; Woessner, R.; Younes, A.; Nemunaitis, J.; Fowler, N.; Curran, M.; Liu, Q.; Zhou, T.; Schmidt, J.; Jo, M.; Lee, S. J.; Yamashita, M.; Hughes, S. G.; Fayad, L.; Piha-Paul, S.; Nadella, M. V. P.; Xiao, X.; Hsu, J.; Revenko, A.; Monia, B. P.; MacLeod, A. R.; Hong, D. S. STAT3 Antisense Oligonucleotide AZD9150 in a Subset of Patients with Heavily Pretreated Lymphoma: Results of a Phase 1b Trial. *J Immunother Cancer* **2018**, *6*. https://doi.org/10.1186/s40425-018-0436-5.

(64) Khan, M. W.; Saadalla, A.; Ewida, A. H.; Al-Katranji, K.; Al-Saoudi, G.; Giaccone, Z. T.; Gounari, F.; Zhang, M.; Frank, D. A.; Khazaie, K. The STAT3 Inhibitor Pyrimethamine Displays Anti-Cancer and Immune Stimulatory Effects in Murine Models of Breast Cancer. *Cancer Immunol Immunother* **2018**, *67* (1), 13–23. https://doi.org/10.1007/s00262-017-2057-0.

(65) Research, A. A. for C. Fedratinib Becomes New Option in Myelofibrosis. *Cancer Discov* **2019**, *9* (10), 1332–1332. https://doi.org/10.1158/2159-8290.CD-NB2019-102.

(66) Peraro, L.; Kritzer, J. A. Emerging Methods and Design Principles for Cell-Penetrant Peptides. *Angew. Chem.-Int. Edit.* **2018**, *57* (37), 11868–11881. https://doi.org/10.1002/anie.201801361.

(67) Heitz, F.; Morris, M. C.; Divita, G. Twenty Years of Cell-Penetrating Peptides: From Molecular Mechanisms to Therapeutics. *Br. J. Pharmacol.* **2009**, *157* (2), 195–206. https://doi.org/10.1111/j.1476-5381.2009.00057.x.

(68) Guidotti, G.; Brambilla, L.; Rossi, D. Cell-Penetrating Peptides: From Basic Research to Clinics. *Trends in Pharmacological Sciences* **2017**, *38* (4), 406–424. https://doi.org/10.1016/j.tips.2017.01.003.

(69) Kertész, Á.; Váradi, G.; Tóth, G. K.; Fajka-Boja, R.; Monostori, É.; Sármay, G. Optimization of the Cellular Import of Functionally Active SH2-Domain-Interacting Phosphopeptides. *Cell. Mol. Life Sci.* **2006**, *63* (22), 2682–2693. https://doi.org/10.1007/s00018-006-6346-6.

(70) Wavreille, A.-S.; Pei, D. A Chemical Approach to the Identification of Tensin-Binding Proteins. *ACS Chem. Biol.* **2007**, *2* (2), 109–118. https://doi.org/10.1021/cb600433g.
(71) Kuil, J.; Fischer, M. J. E.; Mol, N. J. de; Liskamp, R. M. J. Cell Permeable ITAM Constructs for the Modulation of Mediator Release in Mast Cells. *Org. Biomol. Chem.* **2011**, *9* (3), 820–833. https://doi.org/10.1039/C0OB00441C.
(72) Watson, G. M.; Kulkarni, K.; Sang, J.; Ma, X.; Gunzburg, M. J.; Perlmutter, P.; Wilce, M. C. J.; Wilce, J. A. Discovery, Development, and Cellular Delivery of Potent and Selective Bicyclic Peptide Inhibitors of Grb7 Cancer Target. *J. Med. Chem.* **2017**, *60* (22), 9349–9359. https://doi.org/10.1021/acs.jmedchem.7b01320.
(73) Lian, W.; Jiang, B.; Qian, Z.; Pei, D. Cell-Permeable Bicyclic Peptide Inhibitors against Intracellular Proteins. *Journal of the American Chemical Society* **2014**, *136* (28), 9830–9833. https://doi.org/10.1021/ja503710n.
(74) Qian, Z.; Martyna, A.; Hard, R. L.; Wang, J.; Appiah-Kubi, G.; Coss, C.; Phelps, M. A.; Rossman, J. S.; Pei, D. Discovery and Mechanism of Highly Efficient Cyclic Cell-Penetrating Peptides. *Biochemistry* **2016**, *55* (18), 2601–2612. https://doi.org/10.1021/acs.biochem.6b00226.
(75) Wissner, R. F.; Steinauer, A.; Knox, S. L.; Thompson, A. D.; Schepartz, A. Fluorescence Correlation Spectroscopy Reveals Efficient Cytosolic Delivery of Protein Cargo by Cell-Permeant Miniature Proteins. *ACS Central Science* **2018**, *4* (10), 1379–1393. https://doi.org/10.1021/acscentsci.8b00446.
(76) Song, J.; Qian, Z.; Sahni, A.; Chen, K.; Pei, D. Cyclic Cell-Penetrating Peptides with Single Hydrophobic Groups. *ChemBioChem* **2019**, *20* (16), 2085–2088. https://doi.org/10.1002/cbic.201900370.
(77) Levine, B.; Kroemer, G. Autophagy in the Pathogenesis of Disease. *Cell* **2008**, *132* (1), 27–42. https://doi.org/10.1016/j.cell.2007.12.018.
(78) Levine, B.; Kroemer, G. Biological Functions of Autophagy Genes: A Disease Perspective. *Cell* **2019**, *176* (1), 11–42. https://doi.org/10.1016/j.cell.2018.09.048.
(79) Levy, J. M. M.; Towers, C. G.; Thorburn, A. Targeting Autophagy in Cancer. *Nat Rev Cancer* **2017**, *17* (9), 528–542. https://doi.org/10.1038/nrc.2017.53.
(80) Green, D. R.; Levine, B. To Be or Not to Be? How Selective Autophagy and Cell Death Govern Cell Fate. *Cell* **2014**, *157* (1), 65–75. https://doi.org/10.1016/j.cell.2014.02.049.
(81) Vega-Rubín-de-Celis, S.; Zou, Z.; Fernández, Á. F.; Ci, B.; Kim, M.; Xiao, G.; Xie, Y.; Levine, B. Increased Autophagy Blocks HER2-Mediated Breast Tumorigenesis. *PNAS* **2018**, *115* (16), 4176–4181. https://doi.org/10.1073/pnas.1717800115.
(82) Khor, B.; Gardet, A.; Xavier, R. J. Genetics and Pathogenesis of Inflammatory Bowel Disease. *Nature* **2011**, *474* (7351), 307–317. https://doi.org/10.1038/nature10209.
(83) Molineros, J. E.; Yang, W.; Zhou, X.; Sun, C.; Okada, Y.; Zhang, H.; Chua, K. H.; Lau, Y.-L.; Kochi, Y.; Suzuki, A.; Yamamoto, K.; Ma, J.; Bang, S.-Y.; Lee, H.-S.; Kim, K.; Bae, S.-C.; Zhang, H.; Shen, N.; Looger, L. L.; Nath, S. K. Confirmation of Five Novel Susceptibility Loci for Systemic Lupus Erythematosus (SLE) and Integrated Network Analysis of 82 SLE Susceptibility Loci. *Human Molecular Genetics* **2017**, ddx026. https://doi.org/10.1093/hmg/ddx026.
(84) Kim, M.; Sandford, E.; Gatica, D.; Qiu, Y.; Liu, X.; Zheng, Y.; Schulman, B. A.; Xu, J.; Semple, I.; Ro, S.-H.; Kim, B.; Mavioglu, R. N.; Tolun, A.; Jipa, A.; Takats, S.; Karpati, M.; Li, J. Z.; Yapici, Z.; Juhasz, G.; Lee, J. H.; Klionsky, D. J.; Burmeister, M. Mutation in ATG5 Reduces Autophagy and Leads to Ataxia with Developmental Delay. *eLife* **2016**, *5*. https://doi.org/10.7554/eLife.12245.

(85) Fernández, Á. F.; Sebti, S.; Wei, Y.; Zou, Z.; Shi, M.; McMillan, K. L.; He, C.; Ting, T.; Liu, Y.; Chiang, W.-C.; Marciano, D. K.; Schiattarella, G. G.; Bhagat, G.; Moe, O. W.; Hu, M. C.; Levine, B. Disruption of the Beclin 1-BCL2 Autophagy Regulatory Complex Promotes Longevity in Mice. *Nature* **2018**, *558* (7708), 136–140. https://doi.org/10.1038/s41586-018-0162-7.

(86) Qu, X.; Yu, J.; Bhagat, G.; Furuya, N.; Hibshoosh, H.; Troxel, A.; Rosen, J.; Eskelinen, E.-L.; Mizushima, N.; Ohsumi, Y.; Cattoretti, G.; Levine, B. Promotion of Tumorigenesis by Heterozygous Disruption of the Beclin 1 Autophagy Gene. *J. Clin. Invest.* **2003**, *112* (12), 1809–1820. https://doi.org/10.1172/JCI20039.

(87) Guo, J. Y.; Karsli-Uzunbas, G.; Mathew, R.; Aisner, S. C.; Kamphorst, J. J.; Strohecker, A. M.; Chen, G.; Price, S.; Lu, W.; Teng, X.; Snyder, E.; Santanam, U.; Dipaola, R. S.; Jacks, T.; Rabinowitz, J. D.; White, E. Autophagy Suppresses Progression of K-Ras-Induced Lung Tumors to Oncocytomas and Maintains Lipid Homeostasis. *Genes Dev.* **2013**, *27* (13), 1447–1461. https://doi.org/10.1101/gad.219642.113.

(88) Xie, X.; Koh, J. Y.; Price, S.; White, E.; Mehnert, J. M. Atg7 Overcomes Senescence and Promotes Growth of BrafV600E-Driven Melanoma. *Cancer Discov* **2015**, *5* (4), 410–423. https://doi.org/10.1158/2159-8290.CD-14-1473.

(89) Santanam, U.; Banach-Petrosky, W.; Abate-Shen, C.; Shen, M. M.; White, E.; DiPaola, R. S. Atg7 Cooperates with Pten Loss to Drive Prostate Cancer Tumor Growth. *Genes Dev.* **2016**, *30* (4), 399–407. https://doi.org/10.1101/gad.274134.115.

(90) Gammoh, N.; Fraser, J.; Puente, C.; Syred, H. M.; Kang, H.; Ozawa, T.; Lam, D.; Acosta, J. C.; Finch, A. J.; Holland, E.; Jiang, X. Suppression of Autophagy Impedes Glioblastoma Development and Induces Senescence. *Autophagy* **2016**, *12* (9), 1431–1439. https://doi.org/10.1080/15548627.2016.1190053.

(91) Peng, Y.-F.; Shi, Y.-H.; Ding, Z.-B.; Ke, A.-W.; Gu, C.-Y.; Hui, B.; Zhou, J.; Qiu, S.-J.; Dai, Z.; Fan, J. Autophagy Inhibition Suppresses Pulmonary Metastasis of HCC in Mice via Impairing Anoikis Resistance and Colonization of HCC Cells. *Autophagy* **2013**, *9* (12), 2056–2068. https://doi.org/10.4161/auto.26398.

(92) Mowers, E. E.; Sharifi, M. N.; Macleod, K. F. Autophagy in Cancer Metastasis. *Oncogene* **2017**, *36* (12), 1619–1630. https://doi.org/10.1038/onc.2016.333.

(93) Katheder, N. S.; Khezri, R.; O'Farrell, F.; Schultz, S. W.; Jain, A.; Rahman, M. M.; Schink, K. O.; Theodossiou, T. A.; Johansen, T.; Juhász, G.; Bilder, D.; Brech, A.; Stenmark, H.; Rusten, T. E. Microenvironmental Autophagy Promotes Tumour Growth. *Nature* **2017**, *541* (7637), 417–420. https://doi.org/10.1038/nature20815.

(94) Briceño, E.; Reyes, S.; Sotelo, J. Therapy of Glioblastoma Multiforme Improved by the Antimutagenic Chloroquine. *Neurosurg Focus* **2003**, *14* (2), e3. https://doi.org/10.3171/foc.2003.14.2.4.

(95) Sotelo, J.; Briceño, E.; López-González, M. A. Adding Chloroquine to Conventional Treatment for Glioblastoma Multiforme: A Randomized, Double-Blind, Placebo-Controlled Trial. *Ann. Intern. Med.* **2006**, *144* (5), 337–343. https://doi.org/10.7326/0003-4819-144-5-200603070-00008.

(96) Boone, B. A.; Bahary, N.; Zureikat, A. H.; Moser, A. J.; Normolle, D. P.; Wu, W.-C.; Singhi, A. D.; Bao, P.; Bartlett, D. L.; Liotta, L. A.; Espina, V.; Loughran, P.; Lotze, M. T.; Zeh, H. J. Safety and Biologic Response of Pre-Operative Autophagy Inhibition in Combination with Gemcitabine in Patients with Pancreatic Adenocarcinoma. *Ann. Surg. Oncol.* **2015**, *22* (13), 4402–4410. https://doi.org/10.1245/s10434-015-4566-4.

(97) Rubinsztein, D. C.; Gestwicki, J. E.; Murphy, L. O.; Klionsky, D. J. Potential Therapeutic Applications of Autophagy. *Nature Reviews Drug Discovery* **2007**, *6* (4), 304–312. https://doi.org/10.1038/nrd2272.

(98) Sugawara, K.; Suzuki, N. N.; Fujioka, Y.; Mizushima, N.; Ohsumi, Y.; Inagaki, F. The Crystal Structure of Microtubule-Associated Protein Light Chain 3, a Mammalian Homologue of Saccharomyces Cerevisiae Atg8. *Genes Cells* **2004**, *9* (7), 611–618. https://doi.org/10.1111/j.1356-9597.2004.00750.x.

(99) Behrends, C.; Sowa, M. E.; Gygi, S. P.; Harper, J. W. Network Organization of the Human Autophagy System. *Nature* **2010**, *466* (7302), 68–76. https://doi.org/10.1038/nature09204.

(100) Weidberg, H.; Shvets, E.; Shpilka, T.; Shimron, F.; Shinder, V.; Elazar, Z. LC3 and GATE-16/GABARAP Subfamilies Are Both Essential yet Act Differently in Autophagosome Biogenesis. *EMBO J.* **2010**, *29* (11), 1792–1802. https://doi.org/10.1038/emboj.2010.74.

(101) Nguyen, T. N.; Padman, B. S.; Usher, J.; Oorschot, V.; Ramm, G.; Lazarou, M. Atg8 Family LC3/GABARAP Proteins Are Crucial for Autophagosome-Lysosome Fusion but Not Autophagosome Formation during PINK1/Parkin Mitophagy and Starvation. *J. Cell Biol.* **2016**, *215* (6), 857–874. https://doi.org/10.1083/jcb.201607039.

(102) Lazarou, M.; Sliter, D. A.; Kane, L. A.; Sarraf, S. A.; Wang, C.; Burman, J. L.; Sideris, D. P.; Fogel, A. I.; Youle, R. J. The Ubiquitin Kinase PINK1 Recruits Autophagy Receptors to Induce Mitophagy. *Nature* **2015**, *524* (7565), 309–314. https://doi.org/10.1038/nature14893.

(103) Grunwald, D. S.; Otto, N. M.; Park, J.-M.; Song, D.; Kim, D.-H. GABARAPs and LC3s Have Opposite Roles in Regulating ULK1 for Autophagy Induction. *Autophagy* **2019**, *0* (0), 1–15. https://doi.org/10.1080/15548627.2019.1632620.

(104) Alemu, E. A.; Lamark, T.; Torgersen, K. M.; Birgisdottir, A. B.; Larsen, K. B.; Jain, A.; Olsvik, H.; Øvervatn, A.; Kirkin, V.; Johansen, T. ATG8 Family Proteins Act as Scaffolds for Assembly of the ULK Complex: SEQUENCE REQUIREMENTS FOR LC3-INTERACTING REGION (LIR) MOTIFS. *Journal of Biological Chemistry* **2012**, *287* (47), 39275–39290. https://doi.org/10.1074/jbc.M112.378109.

(105) Satoo, K.; Noda, N. N.; Kumeta, H.; Fujioka, Y.; Mizushima, N.; Ohsumi, Y.; Inagaki, F. The Structure of Atg4B-LC3 Complex Reveals the Mechanism of LC3 Processing and Delipidation during Autophagy. *EMBO J.* **2009**, *28* (9), 1341–1350. https://doi.org/10.1038/emboj.2009.80.

(106) Padman, B. S.; Nguyen, T. N.; Uoselis, L.; Skulsuppaisarn, M.; Nguyen, L. K.; Lazarou, M. LC3/GABARAPs Drive Ubiquitin-Independent Recruitment of Optineurin and NDP52 to Amplify Mitophagy. *Nature Communications* **2019**, *10* (1). https://doi.org/10.1038/s41467-019-08335-6.

(107) Pankiv, S.; Clausen, T. H.; Lamark, T.; Brech, A.; Bruun, J.-A.; Outzen, H.; Øvervatn, A.; Bjørkøy, G.; Johansen, T. P62/SQSTM1 Binds Directly to Atg8/LC3 to Facilitate Degradation of Ubiquitinated Protein Aggregates by Autophagy. *J. Biol. Chem.* **2007**, *282* (33), 24131–24145. https://doi.org/10.1074/jbc.M702824200.

(108) Pankiv, S.; Alemu, E. A.; Brech, A.; Bruun, J.-A.; Lamark, T.; Overvatn, A.; Bjørkøy, G.; Johansen, T. FYCO1 Is a Rab7 Effector That Binds to LC3 and PI3P to Mediate Microtubule plus End-Directed Vesicle Transport. *J. Cell Biol.* **2010**, *188* (2), 253–269. https://doi.org/10.1083/jcb.200907015.

(109) McEwan, D. G.; Popovic, D.; Gubas, A.; Terawaki, S.; Suzuki, H.; Stadel, D.; Coxon, F. P.; Miranda de Stegmann, D.; Bhogaraju, S.; Maddi, K.; Kirchof, A.; Gatti, E.; Helfrich, M. H.; Wakatsuki, S.; Behrends, C.; Pierre, P.; Dikic, I. PLEKHM1 Regulates Autophagosome-

Lysosome Fusion through HOPS Complex and LC3/GABARAP Proteins. *Mol. Cell* **2015**, *57* (1), 39–54. https://doi.org/10.1016/j.molcel.2014.11.006.

(110) Mikhaylova, O.; Stratton, Y.; Hall, D.; Kellner, E.; Ehmer, B.; Drew, A. F.; Gallo, C. A.; Plas, D. R.; Biesiada, J.; Meller, J.; Czyzyk-Krzeska, M. F. VHL-Regulated MiR-204 Suppresses Tumor Growth through Inhibition of LC3B-Mediated Autophagy in Renal Clear Cell Carcinoma. *Cancer Cell* **2012**, *21* (4), 532–546. https://doi.org/10.1016/j.ccr.2012.02.019.

(111) Klebig, C.; Seitz, S.; Arnold, W.; Deutschmann, N.; Pacyna-Gengelbach, M.; Scherneck, S.; Petersen, I. Characterization of {gamma}-Aminobutyric Acid Type A Receptor-Associated Protein, a Novel Tumor Suppressor, Showing Reduced Expression in Breast Cancer. *Cancer Res.* **2005**, *65* (2), 394–400.

(112) Genau, H. M.; Huber, J.; Baschieri, F.; Akutsu, M.; Dötsch, V.; Farhan, H.; Rogov, V.; Behrends, C. CUL3-KBTBD6/KBTBD7 Ubiquitin Ligase Cooperates with GABARAP Proteins to Spatially Restrict TIAM1-RAC1 Signaling. *Mol. Cell* **2015**, *57* (6), 995–1010. https://doi.org/10.1016/j.molcel.2014.12.040.

(113) Birgisdottir, Å. B.; Lamark, T.; Johansen, T. The LIR Motif - Crucial for Selective Autophagy. *J. Cell. Sci.* **2013**, *126* (Pt 15), 3237–3247. https://doi.org/10.1242/jcs.126128.

(114) Li, J.; Zhu, R.; Chen, K.; Zheng, H.; Zhao, H.; Yuan, C.; Zhang, H.; Wang, C.; Zhang, M. Potent and Specific Atg8-Targeting Autophagy Inhibitory Peptides from Giant Ankyrins. *Nature Chemical Biology* **2018**, *14* (8), 778–787. https://doi.org/10.1038/s41589-018-0082-8.

(115) Wirth, M.; Zhang, W.; Razi, M.; Nyoni, L.; Joshi, D.; O'Reilly, N.; Johansen, T.; Tooze, S. A.; Mouilleron, S. Molecular Determinants Regulating Selective Binding of Autophagy Adapters and Receptors to ATG8 Proteins. *Nature Communications* **2019**, *10* (1). https://doi.org/10.1038/s41467-019-10059-6.

(116) Atkinson, J. M.; Ye, Y.; Gebru, M. T.; Liu, Q.; Zhou, S.; Young, M. M.; Takahashi, Y.; Lin, Q.; Tian, F.; Wang, H.-G. Time-Resolved FRET and NMR Analyses Reveal Selective Binding of Peptides Containing the LC3-Interacting Region to ATG8 Family Proteins. *Journal of Biological Chemistry* **2019**, *294* (38), 14033–14042. https://doi.org/10.1074/jbc.RA119.008723.

(117) Olsvik, H. L.; Lamark, T.; Takagi, K.; Larsen, K. B.; Evjen, G.; Øvervatn, A.; Mizushima, T.; Johansen, T. FYCO1 Contains a C-Terminally Extended, LC3A/B-Preferring LC3-Interacting Region (LIR) Motif Required for Efficient Maturation of Autophagosomes during Basal Autophagy. *J. Biol. Chem.* **2015**, *290* (49), 29361–29374. https://doi.org/10.1074/jbc.M115.686915.

(118) Cheng, X.; Wang, Y.; Gong, Y.; Li, F.; Guo, Y.; Hu, S.; Liu, J.; Pan, L. Structural Basis of FYCO1 and MAP1LC3A Interaction Reveals a Novel Binding Mode for Atg8-Family Proteins. *Autophagy* **2016**, *12* (8), 1330–1339. https://doi.org/10.1080/15548627.2016.1185590.

(119) Popelka, H.; Klionsky, D. J. Structural Basis for Extremely Strong Binding Affinity of Giant Ankyrins to LC3/GABARAP and Its Application in the Inhibition of Autophagy. *Autophagy* **2018**, *14* (11), 1847–1849. https://doi.org/10.1080/15548627.2018.1522884.

(120) Sakurai, S.; Tomita, T.; Shimizu, T.; Ohto, U. The Crystal Structure of Mouse LC3B in Complex with the FYCO1 LIR Reveals the Importance of the Flanking Region of the LIR Motif. *Acta Crystallographica Section F Structural Biology Communications* **2017**, *73* (3), 130–137. https://doi.org/10.1107/S2053230X17001911.

(121) Darnell, J. E. Transcription Factors as Targets for Cancer Therapy. *Nat Rev Cancer* **2002**, *2* (10), 740–749. https://doi.org/10.1038/nrc906.
(122) Bromberg, J. Stat Proteins and Oncogenesis. *J Clin Invest* **2002**, *109* (9), 1139–1142. https://doi.org/10.1172/JCI15617.
(123) Furtek, S. L.; Backos, D. S.; Matheson, C. J.; Reigan, P. Strategies and Approaches of Targeting STAT3 for Cancer Treatment. *ACS Chemical Biology* **2016**, *11* (2), 308–318. https://doi.org/10.1021/acschembio.5b00945.
(124) Schust, J.; Berg, T. A High-Throughput Fluorescence Polarization Assay for Signal Transducer and Activator of Transcription 3. *Analytical Biochemistry* **2004**, *330* (1), 114–118. https://doi.org/10.1016/j.ab.2004.03.024.
(125) Nelson, E. A.; Walker, S. R.; Kepich, A.; Gashin, L. B.; Hideshima, T.; Ikeda, H.; Chauhan, D.; Anderson, K. C.; Frank, D. A. Nifuroxazide Inhibits Survival of Multiple Myeloma Cells by Directly Inhibiting STAT3. *Blood* **2008**, *112* (13), 5095–5102. https://doi.org/10.1182/blood-2007-12-129718.
(126) Peraro, L.; Deprey, K. L.; Moser, M. K.; Zou, Z.; Ball, H. L.; Levine, B.; Kritzer, J. A. Cell Penetration Profiling Using the Chloroalkane Penetration Assay. *J Am Chem Soc* **2018**, *140* (36), 11360–11369. https://doi.org/10.1021/jacs.8b06144.
(127) Partridge, A. W.; Kaan, H. Y. K.; Juang, Y.-C.; Sadruddin, A.; Lim, S.; Brown, C. J.; Ng, S.; Thean, D.; Ferrer, F.; Johannes, C.; Yuen, T. Y.; Kannan, S.; Aronica, P.; Tan, Y. S.; Pradhan, M. R.; Verma, C. S.; Hochman, J.; Chen, S.; Wan, H.; Ha, S.; Sherborne, B.; Lane, D. P.; Sawyer, T. K. Incorporation of Putative Helix-Breaking Amino Acids in the Design of Novel Stapled Peptides: Exploring Biophysical and Cellular Permeability Properties. *Molecules* **2019**, *24* (12), 2292. https://doi.org/10.3390/molecules24122292.
(128) Walker, S. R.; Chaudhury, M.; Nelson, E. A.; Frank, D. A. Microtubule-Targeted Chemotherapeutic Agents Inhibit Signal Transducer and Activator of Transcription 3 (STAT3) Signaling. *Mol Pharmacol* **2010**, *78* (5), 903–908. https://doi.org/10.1124/mol.110.066316.
(129) Mandal, P. K.; Gao, F.; Lu, Z.; Ren, Z.; Ramesh, R.; Birtwistle, J. S.; Kaluarachchi, K. K.; Chen, X.; Bast, R. C.; Liao, W. S.; McMurray, J. S. Potent and Selective Phosphopeptide Mimetic Prodrugs Targeted to the Src Homology 2 (SH2) Domain of Signal Transducer and Activator of Transcription 3. *Journal of Medicinal Chemistry* **2011**, *54* (10), 3549–3563. https://doi.org/10.1021/jm2000882.
(130) Soudah, T.; Khawaled, S.; Aqeilan, R. I.; Yavin, E. AntimiR-155 Cyclic Peptide–PNA Conjugate: Synthesis, Cellular Uptake, and Biological Activity. *ACS Omega* **2019**, *4* (9), 13954–13961. https://doi.org/10.1021/acsomega.9b01697.
(131) Cai, B.; Kim, D.; Akhand, S.; Sun, Y.; Cassell, R. J.; Alpsoy, A.; Dykhuizen, E. C.; Van Rijn, R. M.; Wendt, M. K.; Krusemark, C. J. Selection of DNA-Encoded Libraries to Protein Targets within and on Living Cells. *J. Am. Chem. Soc.* **2019**, *141* (43), 17057–17061. https://doi.org/10.1021/jacs.9b08085.
(132) Peraro, L.; Zou, Z.; Makwana, K. M.; Cummings, A. E.; Ball, H. L.; Yu, H.; Lin, Y.-S.; Levine, B.; Kritzer, J. A. Diversity-Oriented Stapling Yields Intrinsically Cell-Penetrant Inducers of Autophagy. *J. Am. Chem. Soc.* **2017**, *139* (23), 7792–7802. https://doi.org/10.1021/jacs.7b01698.
(133) Zhang, X.; He, Y.; Liu, S.; Yu, Z.; Jiang, Z.-X.; Yang, Z.; Dong, Y.; Nabinger, S. C.; Wu, L.; Gunawan, A. M.; Wang, L.; Chan, R. J.; Zhang, Z.-Y. Salicylic Acid Based Small Molecule Inhibitor for the Oncogenic Src Homology-2 Domain Containing Protein Tyrosine Phosphatase-2 (SHP2). *Journal of Medicinal Chemistry* **2010**, *53* (6), 2482–2493. https://doi.org/10.1021/jm901645u.

(134) Frankson, R.; Yu, Z.-H.; Bai, Y.; Li, Q.; Zhang, R.-Y.; Zhang, Z.-Y. Therapeutic Targeting of Oncogenic Tyrosine Phosphatases. *Cancer Research* **2017**, *77* (21), 5701–5705. https://doi.org/10.1158/0008-5472.CAN-17-1510.

(135) Namanja, A. T.; Wang, J.; Buettner, R.; Colson, L.; Chen, Y. Allosteric Communication Across STAT3 Domains Associated with STAT3 Function and Disease-Causing Mutation. *J Mol Biol* **2016**, *428* (3), 579–589. https://doi.org/10.1016/j.jmb.2016.01.003.

(136) Siegert, T. R.; Bird, M. J.; Makwana, K. M.; Kritzer, J. A. Analysis of Loops That Mediate Protein-Protein Interactions and Translation into Submicromolar Inhibitors. *J. Am. Chem. Soc.* **2016**, *138* (39), 12876–12884. https://doi.org/10.1021/jacs.6b05656.

(137) Quartararo, J. S.; Wu, P.; Kritzer, J. A. Peptide Bicycles That Inhibit the Grb2 SH2 Domain. *ChemBioChem* **2012**, *13* (10), 1490–1496. https://doi.org/10.1002/cbic.201200175.

(138) Mizushima, N.; Levine, B.; Cuervo, A. M.; Klionsky, D. J. Autophagy Fights Disease through Cellular Self-Digestion. *Nature* **2008**, *451* (7182), 1069–1075. https://doi.org/10.1038/nature06639.

(139) Rubinsztein, D. C.; Codogno, P.; Levine, B. Autophagy Modulation as a Potential Therapeutic Target for Diverse Diseases. *Nat. Rev. Drug Discov.* **2012**, *11* (9), 709-U84. https://doi.org/10.1038/nrd3802.

(140) Mathew, R.; Karantza-Wadsworth, V.; White, E. Role of Autophagy in Cancer. *Nat. Rev. Cancer* **2007**, *7* (12), 961–967. https://doi.org/10.1038/nrc2254.

(141) Piya, S.; Kornblau, S. M.; Ruvolo, V. R.; Mu, H.; Ruvolo, P. P.; McQueen, T.; Davis, R. E.; Hail, N.; Kantarjian, H.; Andreeff, M.; Borthakur, G. Atg7 Suppression Enhances Chemotherapeutic Agent Sensitivity and Overcomes Stroma-Mediated Chemoresistance in Acute Myeloid Leukemia. *Blood* **2016**, *128* (9), 1260–1269. https://doi.org/10.1182/blood-2016-01-692244.

(142) Mauthe, M.; Orhon, I.; Rocchi, C.; Zhou, X.; Luhr, M.; Hijlkema, K.-J.; Coppes, R. P.; Engedal, N.; Mari, M.; Reggiori, F. Chloroquine Inhibits Autophagic Flux by Decreasing Autophagosome-Lysosome Fusion. *Autophagy* **2018**, *14* (8), 1435–1455. https://doi.org/10.1080/15548627.2018.1474314.

(143) Kamens, A. J.; Mientkiewicz, K. M.; Eisert, R. J.; Walz, J. A.; Mace, C. R.; Kritzer, J. A. Thioether-Stapled Macrocyclic Inhibitors of the EH Domain of EHD1. *Bioorg. Med. Chem.* **2018**, *26* (6), 1206–1211. https://doi.org/10.1016/j.bmc.2017.09.007.

(144) Tran, P. T.; Larsen, C. Ø.; Røndbjerg, T.; De Foresta, M.; Kunze, M. B. A.; Marek, A.; Løper, J. H.; Boyhus, L.-E.; Knuhtsen, A.; Lindorff-Larsen, K.; Pedersen, D. S. Diversity-Oriented Peptide Stapling: A Third Generation Copper-Catalysed Azide–Alkyne Cycloaddition Stapling and Functionalisation Strategy. *Chemistry – A European Journal* **2017**, *23* (14), 3490–3495. https://doi.org/10.1002/chem.201700128.

(145) Wu, Y.; Kaur, A.; Fowler, E.; Wiedmann, M. M.; Young, R.; Galloway, W. R. J. D.; Olsen, L.; Sore, H. F.; Chattopadhyay, A.; Kwan, T. T.-L.; Xu, W.; Walsh, S. J.; de Andrade, P.; Janecek, M.; Arumugam, S.; Itzhaki, L. S.; Lau, Y. H.; Spring, D. R. Toolbox of Diverse Linkers for Navigating the Cellular Efficacy Landscape of Stapled Peptides. *ACS Chem. Biol.* **2019**, *14* (3), 526–533. https://doi.org/10.1021/acschembio.9b00063.

(146) Mortensen, K. T.; Osberger, T. J.; King, T. A.; Sore, H. F.; Spring, D. R. Strategies for the Diversity-Oriented Synthesis of Macrocycles. *Chem. Rev.* **2019**, *119* (17), 10288–10317. https://doi.org/10.1021/acs.chemrev.9b00084.

(147) Peraro, L.; Siegert, T. R.; Kritzer, J. A. Conformational Restriction of Peptides Using Dithiol Bis-Alkylation. In *Methods in Enzymology*; Elsevier, 2016; Vol. 580, pp 303–332. https://doi.org/10.1016/bs.mie.2016.05.035.

(148) Timmerman, P.; Beld, J.; Puijk, W. C.; Meloen, R. H. Rapid and Quantitative Cyclization of Multiple Peptide Loops onto Synthetic Scaffolds for Structural Mimicry of Protein Surfaces. *Chembiochem* **2005**, *6* (5), 821–824. https://doi.org/10.1002/cbic.200400374.
(149) Zou, Y.; Spokoyny, A. M.; Zhang, C.; Simon, M. D.; Yu, H.; Lin, Y.-S.; Pentelute, B. L. Convergent Diversity-Oriented Side-Chain Macrocyclization Scan for Unprotected Polypeptides. *Org. Biomol. Chem.* **2013**, *12* (4), 566–573. https://doi.org/10.1039/C3OB42168F.
(150) Weiergräber, O. H.; Stangler, T.; Thielmann, Y.; Mohrlüder, J.; Wiesehan, K.; Willbold, D. Ligand Binding Mode of GABAA Receptor-Associated Protein. *J. Mol. Biol.* **2008**, *381* (5), 1320–1331. https://doi.org/10.1016/j.jmb.2008.06.086.
(151) Walensky, L. D.; Bird, G. H. Hydrocarbon-Stapled Peptides: Principles, Practice, and Progress. *J. Med. Chem.* **2014**, *57* (15), 6275–6288. https://doi.org/10.1021/jm4011675.
(152) Verdine, G. L.; Walensky, L. D. The Challenge of Drugging Undruggable Targets in Cancer: Lessons Learned from Targeting BCL-2 Family Members. *Clin. Cancer Res.* **2007**, *13* (24), 7264–7270. https://doi.org/10.1158/1078-0432.CCR-07-2184.
(153) Heinis, C.; Rutherford, T.; Freund, S.; Winter, G. Phage-Encoded Combinatorial Chemical Libraries Based on Bicyclic Peptides. *Nat. Chem. Biol.* **2009**, *5* (7), 502–507. https://doi.org/10.1038/nchembio.184.
(154) Rogov, V. V.; Stolz, A.; Ravichandran, A. C.; Rios-Szwed, D. O.; Suzuki, H.; Kniss, A.; Löhr, F.; Wakatsuki, S.; Dötsch, V.; Dikic, I.; Dobson, R. C.; McEwan, D. G. Structural and Functional Analysis of the GABARAP Interaction Motif (GIM). *EMBO reports* **2017**, *18* (8), 1382–1396. https://doi.org/10.15252/embr.201643587.
(155) Ma, P.; Schwarten, M.; Schneider, L.; Boeske, A.; Henke, N.; Lisak, D.; Weber, S.; Mohrlüder, J.; Stoldt, M.; Strodel, B.; Methner, A.; Hoffmann, S.; Weiergräber, O. H.; Willbold, D. Interaction of Bcl-2 with the Autophagy-Related GABAA Receptor-Associated Protein (GABARAP) Biophysical characterization and functional implications. *J. Biol. Chem.* **2013**, *288* (52), 37204–37215. https://doi.org/10.1074/jbc.M113.528067.
(156) Stangler, T.; Mayr, L. M.; Dingley, A. J.; Luge, C.; Willbold, D. Sequence-Specific 1H, 13C and 15N Resonance Assignments of Human GABA Receptor Associated Protein. *J. Biomol. NMR* **2001**, *21* (2), 183–184. https://doi.org/10.1023/a:1012416810974.
(157) Dourlat, J.; Valentin, B.; Liu, W.-Q.; Garbay, C. New Syntheses of Tetrazolylmethylphenylalanine and O-Malonyltyrosine as PTyr Mimetics for the Design of STAT3 Dimerization Inhibitors. *Bioorganic & Medicinal Chemistry Letters* **2007**, *17* (14), 3943–3946. https://doi.org/10.1016/j.bmcl.2007.04.107.
(158) Klionsky, D. J. *et al*. Guidelines for the Use and Interpretation of Assays for Monitoring Autophagy (3rd Edition). *Autophagy* **2016**, *12* (1), 1–222. https://doi.org/10.1080/15548627.2015.1100356.